Dynamic Measurement and Characterization of Poisson's Ratio

by

Richard A. Lomenzo, Jr.

Thesis submitted to the Faculty of

Virginia Polytechnic Institute and State University

in partial fulfillment of the requirements for the degree of

MASTER OF SCIENCE

in Mechanical Engineering

APPROVED:

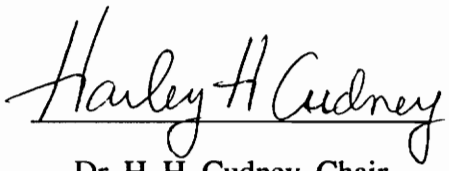

Dr. H. H. Cudney, Chair

Dr. A. L. Wicks

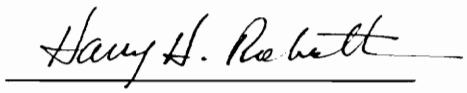

Dr. H. H. Robertshaw

April, 1994

Blacksburg, Virginia

Dynamic Measurement and Characterization of Poisson's Ratio

by

Richard A. Lomenzo, Jr.

Committee Chair: Dr. Harley H. Cudney

Abstract

Poisson's ratio for aluminum is estimated from velocity profile measurements of a free-free beam under dynamic loading conditions A weighted least-squares method is used to select a beam model which is subsequently used to determine the transverse and anticlastic radii of curvature. The model of the beam velocity profile is selected using forward regression with the possible regressor set formed by products of Legendré polynomials in x and y, the two-dimensional coordinates of the beam. The resulting model is manipulated to extract the transverse and anticlastic radii of curvature of the beam which are then used to find local and global estimates of Poisson's ratio. Estimates for Poisson's ratio are found for three different forcing frequencies and three force amplitudes at each frequency. The frequencies selected correspond to the frequencies of the operating shapes dominated by the first, second, and third bending modes. A statistical analysis is performed to assess the quality of the estimates of Poisson's ratio.

Results show that the estimates of Poisson's ratio are dependent on the forcing frequency and forcing amplitude. All estimates are below the accepted value of .33 for aluminum. Contributions of plate modes adversely affect the estimates. Estimates based on the first and third operating shapes exhibit a lower variance than the estimate based on the second operating shapes.

Acknowledgments

I would like to thank all those who guided and encouraged my research as well as those who stood on the sidelines, cheering me on. I thank my major advisor, Dr. Harley Cudney, for his unique insight which contributed to my research and his extreme patience over the rather extended period of my research. I would also like to thank Dr. Al Wicks for his insight and motivation and Dr. Harry Robertshaw for serving on my committee. Thanks to all of my lab colleagues throughout the years, John Richard, John Finefield, Chris Niezrecki, Christina LaPeter, Ning Zhou, Larry Tentor, Joe Colvin, Anton Sumali, Wes Holley, Dave Schmiel, Jon Hill, and Tom McCray for their support, humor, and level-headedness. I would like to thank the Mechanical Engineering classes of 1993 and 1994 for providing me with endless opportunities to teach, laugh, and grieve and the Mechanical Engineering Department for their financial support. Last, I would like to thank my family who believed in me and stood by my side throughout the past several years.

Table of Contents

List of Figures

List of Tables

Nomenclature

Roman Letters

AB	line segment along neutral axis
$A'B'$	arc along neutral axis
a	random variable
a	acceleration
B	parameters of weighted least squares
b	random variable
CD	line segment below neutral axis
$C'D'$	arc below neutral axis
C_a	constant
C_b	constant
C_ℓ	longitudinal wave speed
C_t	transverse wave speed
Cov	covariance
c	random variable
d	displacement
d_0	initial displacement
dx	elongation in x-direction
dy	elongation in y-direction
dL_x	incremental change in length in x-direction
dL_y	incremental change in length in y-direction
d_i	location of i-th measurement location for equal distance measurements
E	Young's modulus

EF	line segment above neutral axis
$E'F'$	arc above neutral axis
e	volume dilatation
e_i	location of i-th measurement location for equal angle measurement
F	applied axial force
$F(t)$	harmonic forcing function
$\|F\|$	amplitude of harmonic forcing function
f	f-value
G	error of weighted least squares
J	square matrix of 1's
K	bulk modulus
K	square root of weighting matrix
k	number of regressors
k	curvature
L_x	length in the x-direction
Ly	length in the y-direction
M	applied bending moment
MSE	mean square error
$N.A.$	neutral axis
n	number of observations
n_{poss}	number of possible regressors
$P(\tilde{x})$	Legendré polynomial
$P(\tilde{y})$	Legendré polynomial
$P(\tilde{x},\tilde{y})$	Legendré surface
p	hydrostatic pressure

r	atomic radius of influence
r^2	sample coefficient of determination
SSR	regression sum of squares
SSE	error sum of squares
SST	total sum of squares
s^2	sample variance
t	time
t_i	i-th time
V	variance
V	variance scaling matrix
v_0	initial velocity
W	weighting matrix
w	beam deflection in the z-direction
X	beam coordinate
X	matrix of regressors
x	beam location, measurement coordinates
x_{ij}	i-th element of j-th regressor
$\tilde{x}$	beam location, Legendré coordinates
Y	beam coordinate
Y	vector of responses
$\hat{Y}$	vector of estimated responses
y	beam location, measurement coordinates
$\tilde{y}$	beam location, Legendré coordinates
Z	response of weighted least squares
z	beam location, measurement coordinates

Greek Letters

α	angle of asymptotes of anticlastic curvature contour lines
α	confidence level
$\hat{\beta}$	vector of estimated parameters
β	vector of parameters
βi	*i*-th parameter of parameter vector
ΔCD	change in line segment *CD*
ε	vector of error terms
εi	individual error term
εx	strain in the *x*-direction
εy	strain in the *y*-direction
εz	strain in the *z*-direction
μ	mean value
μa	mean value of *a*
μb	mean value of *b*
μc	mean value of *c*
θ	included angle
θx	rotation about *x*-axis
θy	rotation about *y*-axis
ρ	density
ρ	transverse radius of curvature
ρ^*	anticlastic radius of curvature
σ	standard deviation
σ_a^2	variance of *a*

σ_b^2	variance of b
σ_c^2	variance of c
σ_{ab}^2	covariance of a and b
σ^2	variance
ν	Poisson's ratio

Chapter 1

Introduction

1.1 Motivation

Material properties of engineering materials are often considered deterministic, fixed quantities. This misconception is rooted in the fact that most published values do not include the inherent uncertainty resulting from the experimental techniques used to arrive at the estimates. The estimate of a material property may be dependent on the conditions under which it was measured and may only be valid under certain loading conditions. A material property determined under static conditions may actually change with dynamic loading conditions. Using the static value in a dynamic model may contribute to a discrepancy between experimental and analytical results. For example, Young's modulus has different values under static conditions than at high strain rates. When experimental results are used as tools for model verification, the dependence of material property estimates on testing and loading conditions not accounted for in the model may result in substantial differences between the predicted and realized results. For cases where Poisson's ratio is used in predicting system responses, such as the vibration of plates and shells, uncertainties in the natural frequencies may be due to a dependence of Poisson's ratio on frequency or amplitude. For this reason, the dependence of material properties on loading conditions must be examined.

1.2 Objective

The goals of this work are to develop and implement a procedure for estimating local and global avulse of Poisson's ratio under dynamic loading conditions, specifically single frequency harmonic point force excitation, and to determine if Poisson's ratio is related to the forcing amplitude and frequency. The procedure must account for the measurement uncertainty and result in an estimate of Poisson's ratio which includes an estimate of the inherent uncertainty.

The scope of this work is limited to estimating Poisson's ratio for aluminum and performing a qualitative comparison of the effect of forcing conditions on the estimates and uncertainties of Poisson's ratio. The example used in this work is a free-free aluminum beam. The method may be applied to other structures and materials, both homogenous and nonhomogenous and may prove especially useful for spatial characterization of composite materials where Poisson's ratio may vary substantially with location.

1.3 Approach

The procedure for estimating Poisson's ratio is based on measuring the anticlastic curvature of the operating shape of a free-free aluminum beam. Nine tests are performed in which the beam is harmonically excited at each of three resonant frequencies with three different force amplitudes at each frequency. A scanning laser Doppler velocimeter measures the velocity profile of the structure. The resulting data consists of the mean value and variance of the voltage at each point on the structure which corresponds to the

component of structure velocity in the direction of the laser beam. A polynomial surface is fit to the spatial voltage data using a weighted least squares method to obtain an analytical expression for the mean value and variance of the velocity profile. The surface is selected using forward regression and an *F*-test. The polynomial expression is converted from measured voltage to out-of-plane displacement amplitude and spatially differentiated twice in the length-wise and width-wise directions. The results are the radii of curvature due to transverse bending and anticlastic bending. The two radii of curvature are then used to calculate local and global estimates and uncertainties of Poisson's ratio for different excitation conditions. Global values from each test are compared to each other and to published values of Poisson's ratio for aluminum to determine if Poisson's ratio is dependent on forcing frequency and amplitude and also to determine if the proposed method yields results consistent with results obtained using different methods.

1.4 Thesis Overview

The proposed method for estimating Poisson's ratio from velocity profiles relies on analytical, statistical, and experimental techniques. Chapter 2 opens with a review of the theoretical development of Poisson's ratio, a review of methods used to measure Poisson's ratio, and a description of the method used in this work to estimate Poisson's ratio. This is followed by a description of the several statistical analysis techniques employed, including linear regression, and the model selection process. Chapter 3 follows with a description of the experimental procedure used to arrive at the measurements needed to implement the proposed method. A description of the scanning laser velocimeter is included to acquaint the general reader with its operation. Results are presented and discussed in Chapter 4. Conclusions and recommendations for future work are presented in Chapter 5.

Chapter 2

Theoretical Development

2.1 Introduction

The proposed method for estimating Poisson's ratio is based on determining a model of the deflection surface of a beam and extracting the lateral and transverse radii of curvature of the beam. The theory behind this method is presented in this chapter. The chapter opens with a brief description of the physical manifestations of Poisson's effect which can be used as a basis for measuring Poisson's ratio. This is followed by a description of analytical and experimental methods for estimating Poisson's ratio and a detailed discussion of the proposed method, including the requirements of the model necessary for estimating Poisson's ratio. This is followed by a description of the statistical method used to transform the experimental measurements into a suitable model meeting these requirements. The manipulations of the model and propagation of uncertainty from the model to the estimate of Poisson's ratio is discussed in the final section.

2.2 Physical Characteristics Modeled by Poisson's Ratio

Poisson's ratio is named for the French scientist and mathematician Simèon Denis Poisson. The variety of Poisson's contributions are illustrated by the many terms which bear his name-Poisson's distribution in statistics, Poisson's integral in potential theory, Poisson brackets in differential equations, and his most noteworthy in the field of mechanical engineering, Poisson's ratio. Poisson's interest in the molecular structure of elastic materials led to his observation that axial elongations of elastic materials were

accompanied by transverse contractions. Poisson's ratio is more generally defined in terms of strains as the negative ratio of transverse strain to axial strain of an element subjected to a uniaxial load

$$\nu = -\frac{\varepsilon_y}{\varepsilon_x} \tag{2.1}$$

where ε_y is the transverse strain, ε_x is the longitudinal strain, and ν is Poisson's ratio.

For most common engineering materials, Poisson's ratio is a positive value. An elongation in the x-direction results in a contraction in the y-direction and a contraction in the x-direction results in an elongation in the y-direction as depicted in Fig. 2.1.

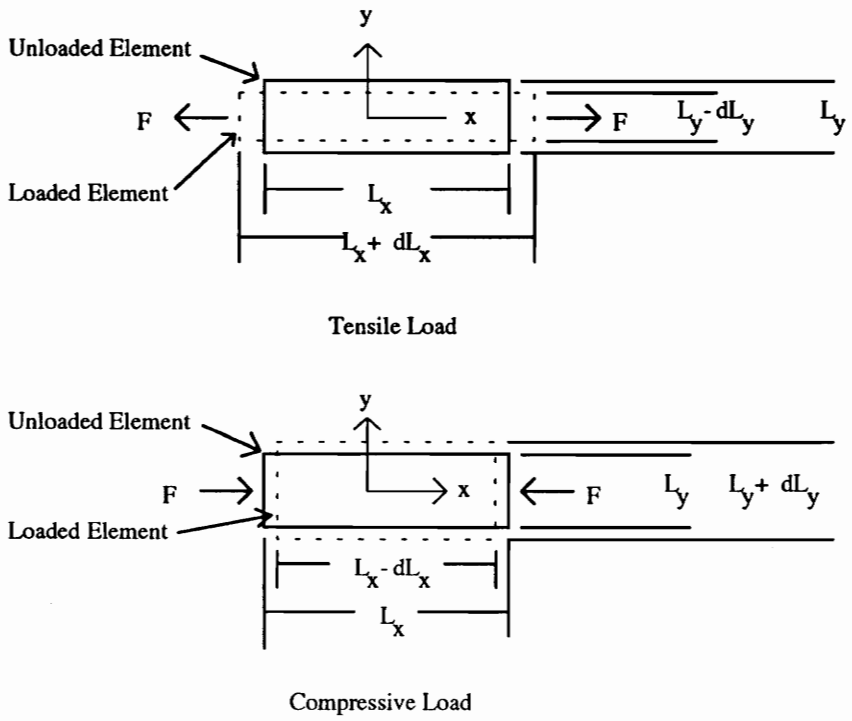

Figure 2.1 Poisson's Effect Under Uniaxial Load

Poisson's effect also manifests itself under different loading conditions as a result of the same mechanism. Consider a beam loaded in pure bending by a pair of equal but opposite moments as in Fig. 2.2.

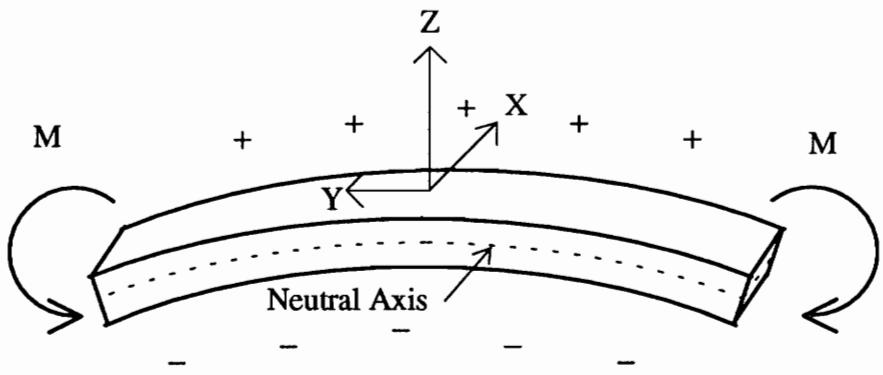

Figure 2.2 Beam in Pure Bending

As a result of the applied couple the top surface is in tension and the lower surface is in compression. The tension in the top surface will cause a compressive strain in the x-direction and the compression in the bottom surface will cause a tensile strain in the x-direction. The resulting strains throughout the thickness of the beam will induce strains parallel to the neutral axis in the x-direction due to Poisson's effect. These induced strains will be compressive in the top surface and tensile in the bottom surface causing contraction of the top surface and expansion of the bottom surface. The cross section resulting from Poisson's has inclined sides with a curved top and bottom. This effect is exaggerated and shown in Fig. 2.3.

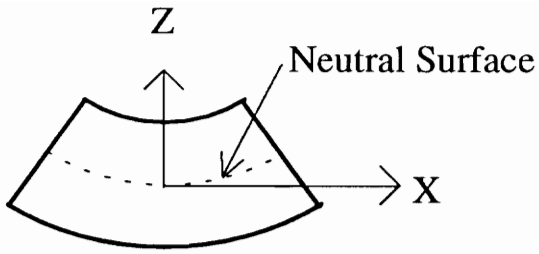

Figure 2.3 Cross Section of Beam in Bending

The curvature in the *xz*-plane is called the anticlastic curvature. Looking at the combined effect of the transverse bending and Poisson's effect, an element of the beam will have curvature in the *yz*-plane due to the applied moment and in the *xz*-plane due to Poisson's effect. The deflection of a beam element with the bending due to Poisson's effect superimposed on the bending due to the applied moments is saddle shaped as shown in Fig. 2.4.

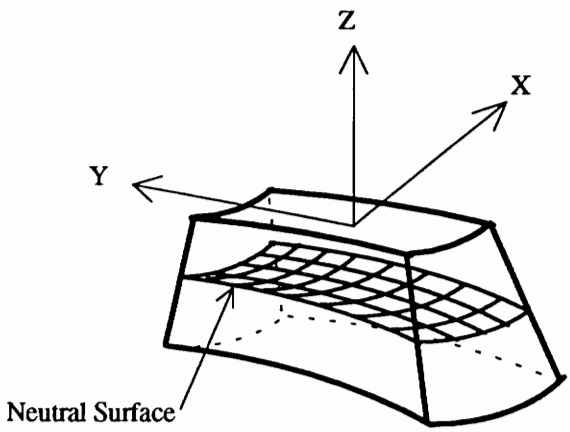

Figure 2.4 Deflection Due to Transverse Bending and Poisson's Effect

Poisson's ratio also plays a role in the propagation of waves through materials. The velocities of longitudinal and transverse waves through isotropic materials are dependent on Young's modulus, (E), density, (ρ), and Poisson's ratio according to

$$C_t = \sqrt{\frac{E}{2(1+\nu)\rho}}$$

$$C_\ell = \sqrt{\frac{E(1-\nu)}{(1+\nu)(1-2\nu)\rho}} \qquad (2.2)$$

where C_t is the transverse wave speed and C_ℓ is the longitudinal wave speed.

In the next section, experimental methods for estimating Poisson's ratio based on these phenomena will be presented.

2.3 Estimates of Poisson's Ratio

Poisson's ratio can be estimated from both analytical models and experimental measurements using a variety of techniques. Values of Poisson's ratio are usually listed as .33 for metals. This value is based on a simple two-dimensional model of the crystalline structure of metals. Although the crystalline structure of metals is three-dimensional and different for different metals, being either body centered cubic, face center cubic, or hexagonal close-packed for a majority of metals, (Smith, 1986) the two-dimensional model is the classic model used for determining theoretical values for Poisson's ratio

(Shanley, 1967 and Juvinal, 1967). The two-dimensional model will be used here to derive Poisson's ratio.

Figure 2.5 shows four atoms of radius r in an undeformed state. Application of a force in the x-direction results in elongation dx and contraction dy.

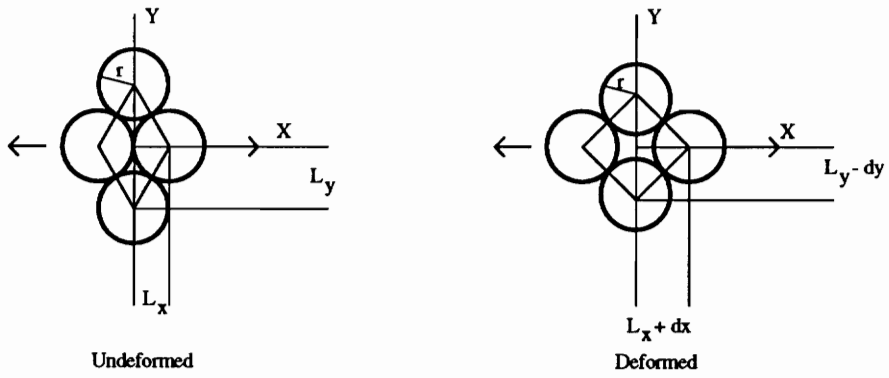

Figure 2.5 Model of Crystal Structure in Undeformed and Deformed States

For uniaxial stress, assuming that the four atoms remain in contact due to interatomic forces, the resulting deformed lengths are related by

$$4r^2 = (L_y - dy)^2 + (L_x + dx)^2 \tag{2.3}$$

Substituting for r based on the undeformed geometry yields

$$L_y^2 + L_x^2 = (L_y - dy)^2 + (L_x + dx)^2 \tag{2.4}$$

The relationship between L_x and L_y can be found by considering the triangle formed by the lines connecting the centers of two adjacent atoms, the line tangent to the upper atom through the center of the lower atom, and the radius of the upper atom in Fig. 2.6.

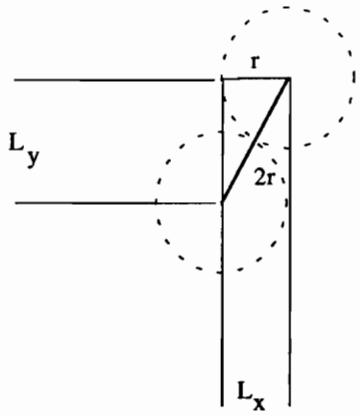

Figure 2.6 Geometry of Atoms

The resulting triangle is a 30°-60°- 90° triangle with sides in the ratio of $1:2:\sqrt{3}$. Applying the geometric relationship between L_x and L_y

$$L_y = \sqrt{3} L_x \tag{2.5}$$

and substituting into Equation 2.4 yields

$$4L_x^2 = 3L_x^2 - 2\sqrt{3}L_x dy + (dy)^2 + L_x^2 + 2L_x dx + (dx)^2 \tag{2.6}$$

Assuming that the deflections are small, the second order terms can be neglected.

Collecting like terms yields

$$4L_x^2 = 4L_x^2 - 2\sqrt{3}L_x dy + 2L_x dx \tag{2.7}$$

Solving for the ratio of the deflections yields

$$\frac{dy}{dx} = \frac{1}{\sqrt{3}} \tag{2.8}$$

Substituting this result and the relationships for strain

$$\begin{aligned} \varepsilon_x &= \frac{dx}{L_x} \\ \varepsilon_y &= \frac{-dy}{L_y} \end{aligned} \tag{2.9}$$

into the definition of Poisson's ratio yields

$$\nu = -\frac{\varepsilon_y}{\varepsilon_x} = -\frac{-dy}{L_y}\frac{L_x}{dx} = -\frac{-dy}{dx}\frac{L_x}{L_y} = \frac{1}{\sqrt{3}}\frac{1}{\sqrt{3}} = \frac{1}{3} \tag{2.10}$$

which is the classical value for Poisson's ratio.

Based on the bulk modulus, (*k*), of a material, limiting values of Poisson's ratio can be derived. The bulk modulus relates the applied hydrostatic pressure, (*p*), to the volume dilatation, (*e*), by

$$K = -\frac{p}{e} \tag{2.11}$$

where the volume dilatation is the decrease in volume.

The bulk modulus is related to Young's modulus and Poisson's ratio by

$$K = \frac{E}{3(1-2\nu)} \tag{2.12}$$

Inspection of the bulk modulus allows for limiting value of Poisson's ratio to be determined. For values of Poisson's ratio between 0 and .5, the bulk modulus will be positive, indicating that the application of a hydrostatic pressure will result in a decrease in volume. For a value of Poisson's ratio greater than .5, the bulk modulus will be negative, indicating that the application of a hydrostatic pressure will cause an increase in volume, a rather unlikely situation. Therefore, the upper limiting value of Poisson's ratio is usually taken to be .5. For a value of Poisson's ratio equal to .5, the bulk modulus is 0, indicating that the material will be incompressible, thus violating the elastic assumption. Therefore, the range of Poisson's ratio for a linear elastic homogenous isotropic material is generally accepted as (Beer and Johnston, 1981)

$$0 < \nu < .5 \tag{2.13}$$

Poisson's ratio can also be estimated using a variety of experimental methods. These methods use measurements of the surface strains, in-plane deflections, out-of-plane deflections, or transverse and longitudinal wave speeds. The majority of these methods are based on surface strain measurements obtained using different techniques. A variety of these methods is discussed in Dally and Reilly (1978).

The concept is that Poisson's ratio defined as the negative of the ratio of the transverse strain to the axial strain when a member is loaded axially. One technique is to use two strain gages, where one gage measures the axial strain and the other measures the transverse strain. This concept can be used with a variety of strain measuring instruments such as electrical, mechanical, and optical strain gages. In order to measure the strains over the entire structure, a large number of gages are needed, a condition which may not be feasible. Grid methods, in which a grid is etched onto the surface and the change in distance between lines also uses the same concept. A grid is painted or etched on the structure and photographed. The structure is then loaded and a photograph is made of the deformed grid pattern. The photographs are compared and the change in the gridlines is used to determine the strain. This method allows for the determination of the strains over the entire surface of a structure, but is limited by the difficulty in measuring the small changes in distance and cannot be used under dynamic loading conditions.

Another method is based on measuring the out-of-plane deflection under pure bending (Durelli, *et al.* 1958 and Timoshenko, 1951). The surface of the structure is polished and a piece of glass is placed on the structure. The saddle shaped deflection of the beam results in an air gap between the structure and glass. Light reflected from the structure results in a diffraction pattern due to the differences in air gap thickness. The contour

lines of the diffraction pattern correspond to contour lines of the structure. The contour lines of the deflection can be shown to be parabolas as illustrated in Fig. 2.7 where the moments are applied at the beam ends in the *y*-direction.

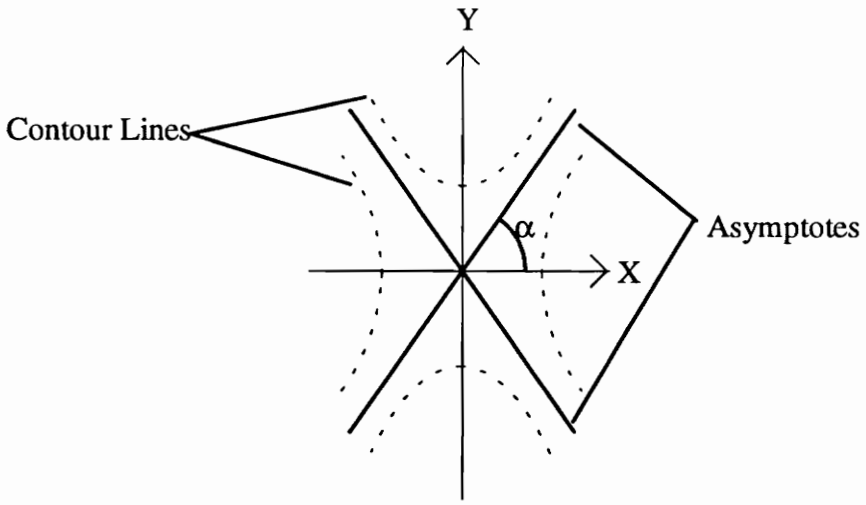

Figure 2.7 Contour Lines for Anticlastic Deflection

where α is the angle between the *x*-axis and the asymptote. It can be shown that the equation for the contour lines is

$$x^2 - \nu y^2 = 0 \tag{2.14}$$

By measuring the angle of the asymptotes of the contour lines it is possible to estimate Poisson's ratio based on the relationship

$$\tan^2 \alpha = \frac{1}{\nu} \tag{2.15}$$

This method has the disadvantage of only allowing for the estimate of a global value of Poisson's ratio and cannot be implemented under dynamic loading conditions.

Another approach for experimentally measuring Poisson's ratio is to measure the velocities of longitudinal, transverse, and Rayleigh waves excited in a structure. This approach is taken by Jarosz and Obata (1992) and Mihara (1991). Jarosz and Obata showed that ultrasonic surface elastic waves excited by laser pulses and measured by piezoelectric transducer attached to the structure can be used to estimate Poisson's ratio. By measuring the wave speeds of Rayleigh waves and transverse waves, a relationship between the wave speeds and Poisson's ratio was used to estimate Poisson's ratio. Jarosz showed that the estimated value of Poisson's ratio for aluminum is .3359. One shortcoming of this method is that it can only be applied to metallic materials and requires the bonding of ultrasonic piezoelectric transducers to the structure. Obata and Mihara also measured the surface elastic waves using an acoustic microscope. Using the acoustic microscope allows for the measurement of local velocities whereas in the method used by Jarosz the average velocities over the entire structure are measured. Obata and Mihara estimate Poisson's ratio to be approximately .30.

The method used in this work is based on measuring the out-of plane displacements and extracting the transverse and anticlastic radii of curvature. A complete description of this method is presented next. This method was applied in a rudimentary form in a previous work (Richard and Lomenzo, 1990). The present work is an extension of the previous work, with a more exhaustive statistical analysis including the forward regression model selection and the use of weighted least squares.

2.4 Analytical Determination of Anticlastic Curvature

Determining the anticlastic curvature at a multitude of points on the structure has been selected as the method for estimating Poisson's ratio. We will now determine the anticlastic curvature from deflection measurements.

Consider the deflection of a two-dimensional, uniform, rectangular beam under the influence of a pair of equal but opposite moments as in Fig. 2.8

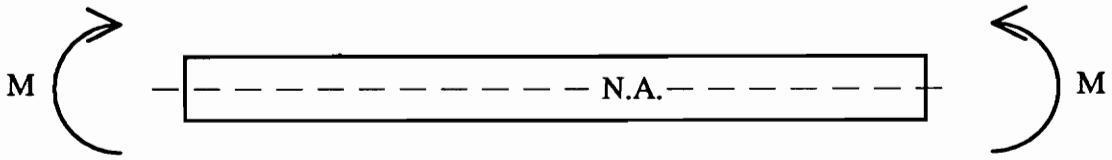

Figure. 2.8 Beam in Bending

where *M* is an ideal applied moment and *N.A.* is the neutral axis of the beam. Since the beam is loaded by a moment pair at the ends, the moment distribution along the length of the beam is constant. Therefore, each element of the beam experiences the same loading. Since the loading of each element is the same, the deformation of all elements will be the same, resulting in the deformation shown in Fig. 2.9.

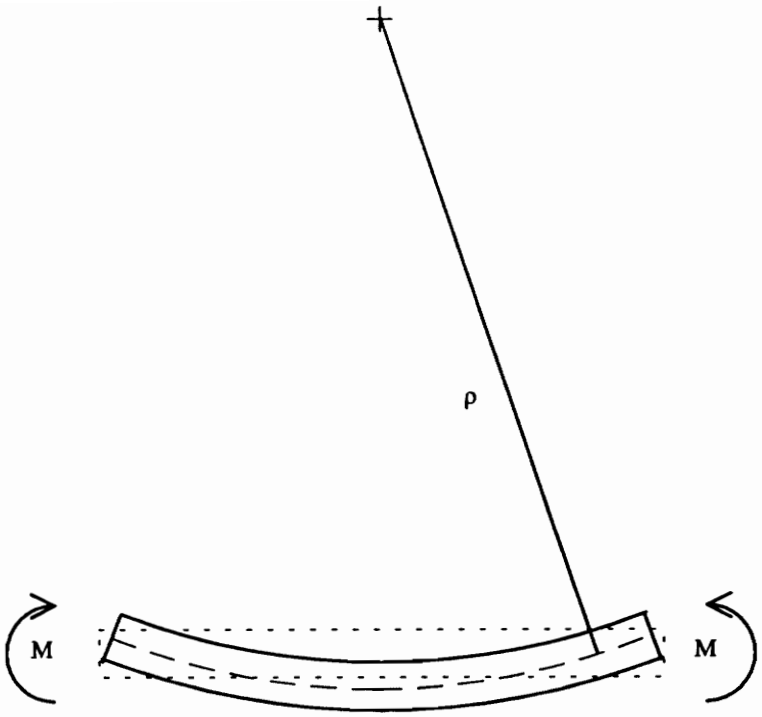

Figure 2.9 Transverse Radius of Curvature

The resulting deflection of the neutral axis will be a circular arc with constant radius of curvature ρ. Also, all planes initially perpendicular to the neutral axis before deformation will remain plane and perpendicular to the neutral axis after deformation. Since there is no axial loading, the length of the neutral axis will not change as a result of the moment loading.

Having defined the radius of curvature, ρ, it is now possible to determine the strains in the beam. Consider a single beam element, before and after deformation, as illustrated in Fig. 2.10.

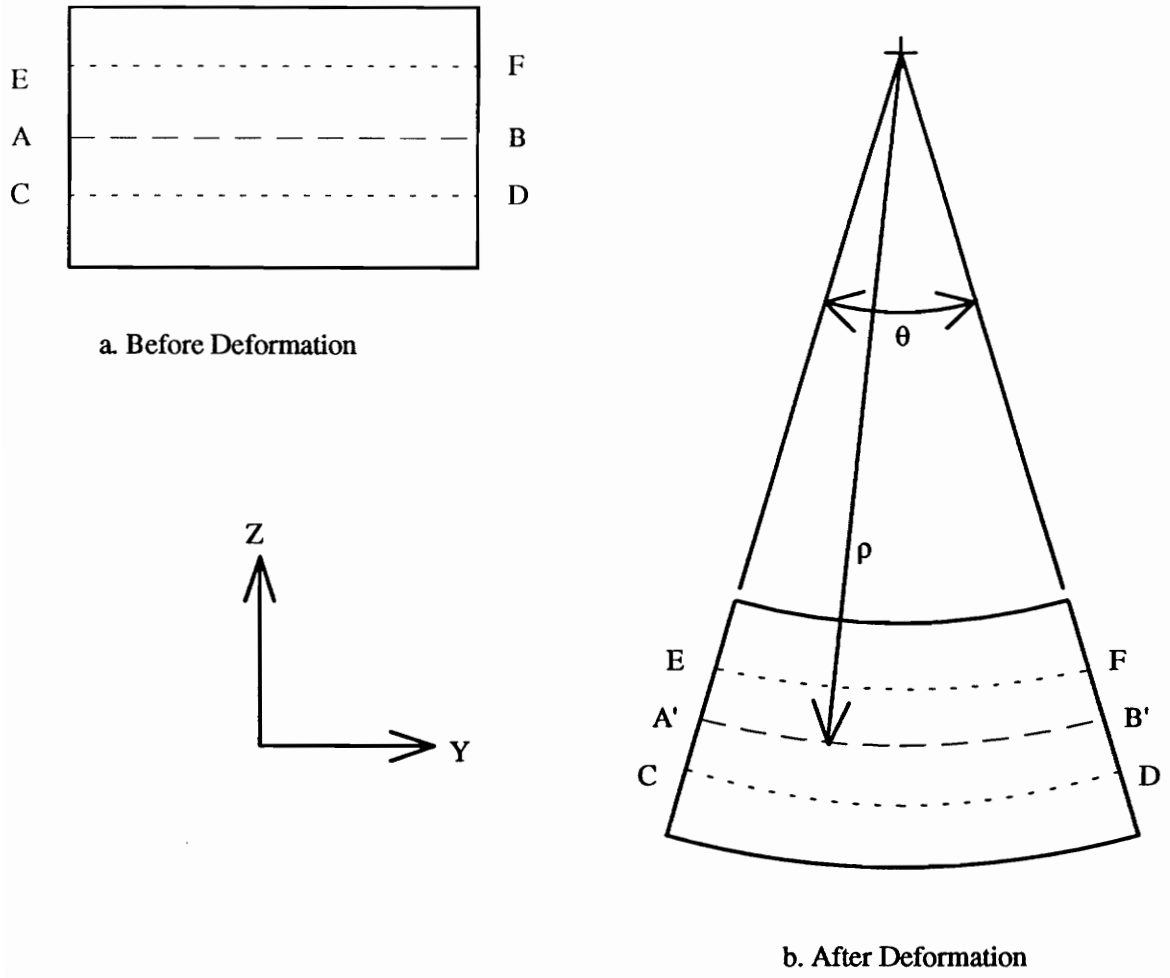

Figure 2.10 Segment of Beam in Bending

The length of the line segment AB lying on the neutral axis is equal to the arc $A'B'$ since the length of the neutral axis remains constant under bending. The length of $A'B'$ is

$$A'B' = \rho\theta \tag{2.16}$$

The length of the line segment CD, a distance z below the neutral axis will deform into an arc of radius $\rho + z$ and have a deformed length of

$$C'D' = (\rho + z)\theta \tag{2.17}$$

Before deformation, the line segment *CD* had a length equal to *AB*. The change in length of line segment *CD* is

$$\Delta CD = (\rho + z)\theta - \rho\theta = z\theta \tag{2.18}$$

The strain at a distance z below the neutral axis can be written as

$$\varepsilon_y = -\frac{z\theta}{\rho} \tag{2.19}$$

The negative sign accounts for the fact that the strain below the neutral axis, in the negative z-direction, will be tensile. Similarly, the strain above the neutral axis will be compressive. It is evident from this relationship that the strain distribution will vary linearly through the depth of the beam.

Similar results exists for a plate loaded by a pair of distributed moments along the edge (Timoshenko, 1951). By switching to a plate, the neutral axis becomes a neutral surface and the radius of curvature is constant across the width of the beam. The strain distribution through the depth of the plate will be the same as for the beam. However due to Poisson's effect, strains will be induced in the y and z directions. Recalling Eqn. 2.1, the induced strains are

$$\varepsilon_x = -\nu\varepsilon_y$$
$$\varepsilon_z = -\nu\varepsilon_y \tag{2.20}$$

Considering only the strain in the x-direction, the strain can be written in terms of the curvature in the xz-plane. This curvature, known as the anticlastic curvature, (ρ^*), can be used in conjunction with Eqn. 2.19 to yield

$$\varepsilon_x = \frac{z}{\rho^*} \tag{2.21}$$

Substituting Eqns. 2.19 and 2.21 into Eqn. 2.1 yields

$$\frac{\rho}{\rho^*} = -\nu \tag{2.22}$$

Thus, if measurements can be made of these two radii of curvature, Poisson's ratio can be estimated.

The results of the previous analysis can also be applied to beams under arbitrary loading by application of Navier's hypothesis. Navier's hypothesis (Ugural, 1991) states that the results obtained for symmetric beams in pure bending can be applied to slender beams of asymmetric cross section, arbitrary loading, and inelastic or nonhomegenous material. This hypothesis is based on three basic assumptions. First, it is assumed that the transverse beam deflections are small compared to the length of the beam, therefore the length of the neutral axis is constant and the slope of the beam is small. Second, sections

of the beam that are normal to the neutral axis before loading remain normal to the neutral axis after loading. Last, the shearing stresses do not affect the distribution of the bending stress. The implications of these assumptions have a slight effect on the previous results. Whereas for the case of pure bending the radius of curvature was constant along the length of the beam, for arbitrary loading, the radius of curvature will vary along the length of the beam.

Having discussed the mechanism which causes anticlastic curvature, we must now determine a method for finding the radius of curvature, ρ, and the anticlastic radius of curvature, ρ^*, for a beam. Consider some arbitrary curve, $y=f(x)$, whose first and second derivatives exist. From analytic geometry (Swokowski, 1988) it can be shown that the curvature, (k), which is defined as the reciprocal of the radius of curvature, is

$$k = \frac{1}{\rho} = \frac{\dfrac{d^2y}{dx^2}}{\left[1+\left(\dfrac{dy}{dx}\right)^2\right]^{3/2}} \tag{2.23}$$

This result can now be used to solve for the radius of curvature and radius of anticlastic curvature of the beam. From the first assumption of Navier's hypothesis, the square of the derivative term in the denominator is much less than one, resulting in

$$\frac{1}{\rho} = \frac{d^2y}{dx^2} \tag{2.24}$$

The deflection of the beam in the z-direction is expressed as

$$w = w(x, y) \tag{2.25}$$

The radius of curvature can be written as

$$\frac{1}{\rho} = \frac{\partial^2 w}{\partial y^2} \tag{2.26}$$

and the radius of anticlastic curvature can be written as

$$\frac{1}{\rho^*} = \frac{\partial^2 w}{\partial x^2} \tag{2.27}$$

The relationship for Poisson's ratio becomes

$$\frac{\rho}{\rho^*} = \frac{\partial^2 w}{\partial x^2} \cdot \frac{1}{\frac{\partial^2 w}{\partial y^2}} = -\nu \tag{2.28}$$

which says that the negative of Poisson's ratio is equal to the second derivative of the deflection with respect to the width divided by the second derivative of the deflection with respect to the length. Therefore in order to arrive at estimates of Poisson's ratio through the use of the radius of curvature and radius of anticlastic curvature, an expression for the

deflection of the beam is required. The expression must be twice differentiable in the x and y directions. These are the only requirements of the expression.

Recalling the beam boundary conditions and coordinate system, shown in Fig. 2.11, there is an observations which can be made about the expected form of the expression for the beam deflection.

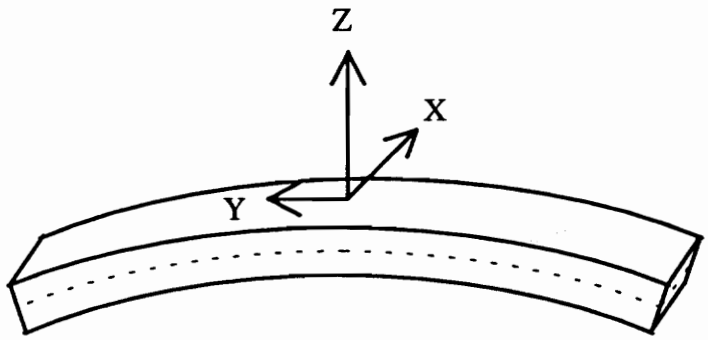

Figure 2.11 Beam in Bending

It was assumed that the curvature in the y-direction is constant across the width of the beam at a given y location. Since the curvature in the x-direction is related to the curvature in the y-direction by

$$\frac{\rho}{\rho^*} = -\nu \tag{2.29}$$

the curvature in the x-direction is expected to be constant at a given y-location.

The method for determining the expression for the beam deflection that meets these requirements is presented in the next section.

2.5 Statistical Techniques

In the previous sections it was shown that given a model of the deflection surface of a structure it is possible to arrive at estimates of Poisson's ratio, provided that the model of the surface is twice differentiable in the x and y directions. In the following sections the procedure for transforming experimental measurements of velocity and the variance of the velocity into a model which can be used to estimate Poisson's ratio is presented. The approach is to fit a model based on the method of least squares and then operate on the least squares model. An outline of the steps used to arrive at estimates of Poisson's ratio from velocity profiles is shown in Figure 2.12.

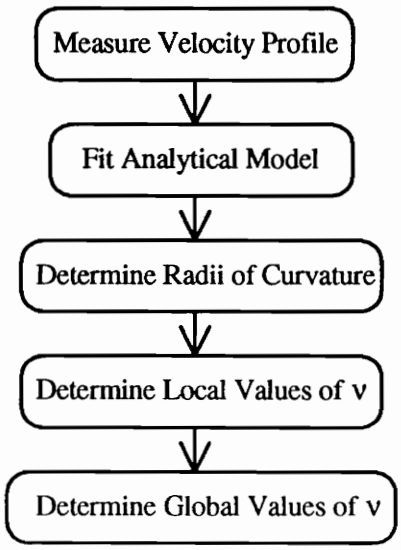

Figure 2.12 Outline of Estimation Procedure

The process for estimating Poisson's ratio is based on several basic statistical concepts which will be briefly discussed in order to acquaint the general reader with these concepts. A more complete discussion of these concepts is available in Neter, *et al.* (1990), and Walpole and Myers (1993).

2.5.1 Random Variables

Random variables are variables whose specific values cannot be determined but whose values can be characterized generally. A random variable can be described by its distribution and the parameters that define its distribution. The random variables considered in this work are assumed to have a normal distribution which is characterized by the mean value, μ, and variance, σ^2, or standard deviation, σ. Figure 2.13 shows the normal distribution and parameters μ and σ.

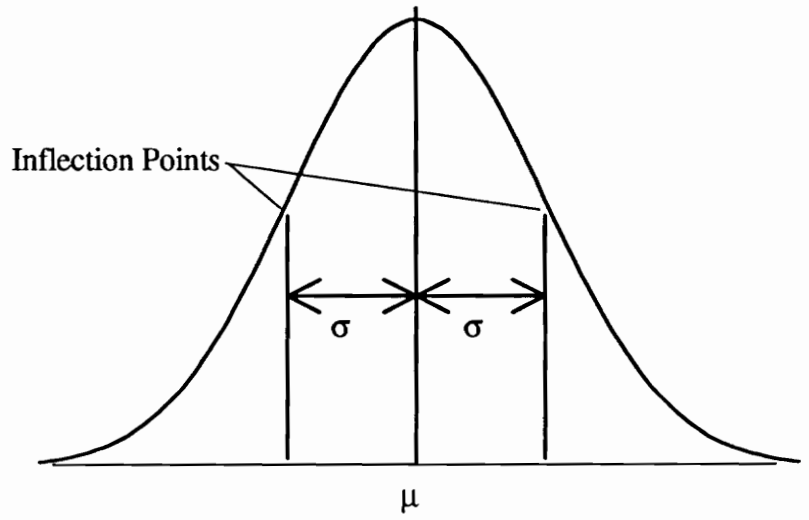

Figure 2.13 Normal Distribution

An important relationship for random variables is the behavior of linear combinations of random variables. Consider normally distributed random variables a and b with mean values μ_a and μ_b and variances $\sigma_a{}^2$ and $\sigma_b{}^2$. If we define a new random variable, c, which is related to a and b according to

$$c = C_a a + C_b b \tag{2.30}$$

it can be shown that the mean and variance of c are

$$\mu_c = C_a \mu_a + C_b \mu_b \tag{2.31}$$

and

$$\sigma_c^2 = C_a^2 \sigma_a^2 + C_b^2 \sigma_b^2 \tag{2.32}$$

provided that the variables a, and b are independent. If the variables a and b are not independent, Eqn. 2.32 becomes

$$\sigma_c^2 = C_a^2 \sigma_a^2 + C_b^2 \sigma_b^2 + 2C_a C_b \sigma_{ab} \tag{2.33}$$

These results can be applied to a linear combination of any number of random variables.

Thus, if

$$\mu = \sum_{i=1}^{n} a_i \mu_i \tag{2.34}$$

then

$$\sigma^2 = \sum_{i=1}^{n} \sum_{j=1}^{n} a_i a_j \sigma_i \sigma_j \tag{2.35}$$

These concepts will be applied later in the conversion of parameters, measurements, and velocities.

2.5.2 Least Squares

The basic concept of least squares is to estimate unknown parameters of a relationship based on a set of assumptions by minimizing the sum of the squared error between the model and the observations. Consider a set of data consisting of n observations, y_i, corresponding to n independent measurements, x_i related by the equation

$$y_i = \beta_0 + \beta_1 x_{i1} + \beta_2 x_{i2} + \ldots + \beta_j x_{ij} + \ldots + \beta_k x_{ik} + \varepsilon_i \tag{2.36}$$

where each x_{ij} is one of the k regressors which is a function of the independent measurements x_i. The error terms, ε_i are the difference between the actual measurements and the model. It is desired to find estimates of the coefficients β_j such that the square of the error between the observations and the fitted values is minimized. It is assumed that the error terms, ε_i, are random variables with zero means and unknown variances. It is

further assumed that each individual error term, ε_i, has the same variance as every other error term. These assumptions are written as

$$E(\varepsilon) = 0, \qquad V(\varepsilon) = \sigma^2 \tag{2.37}$$

The equations can be rewritten in matrix form. Let

$$X = \begin{bmatrix} 1 & x_{11} & x_{12} & \cdots & x_{1k} \\ 1 & x_{21} & x_{22} & \cdots & x_{2k} \\ 1 & x_{31} & x_{32} & \cdots & x_{3k} \\ \vdots & \vdots & \vdots & \ddots & \vdots \\ 1 & x_{n1} & x_{n2} & \cdots & x_{nk} \end{bmatrix}, \quad Y = \begin{bmatrix} y_1 \\ y_2 \\ y_3 \\ \vdots \\ y_n \end{bmatrix}, \quad \varepsilon = \begin{bmatrix} \varepsilon_1 \\ \varepsilon_2 \\ \varepsilon_3 \\ \vdots \\ \varepsilon_n \end{bmatrix}, \quad \beta = \begin{bmatrix} \beta_0 \\ \beta_1 \\ \beta_2 \\ \vdots \\ \beta_k \end{bmatrix} \tag{2.38}$$

where X is the regressor matrix, Y is the vector of measurements, β is the vector of parameters to be estimated, and ε is a vector of error terms.

The physical meaning of the terms in the least squares formulation can be illustrated by considering the displacement of a body with some unknown initial position, d_0, unknown initial velocity, v_0, and constant acceleration, a. The total displacement, as a function of time can be written as

$$d(t) = d_0 + v_o t + \tfrac{1}{2} a t^2 \tag{2.39}$$

Consider n measurements taken at times t_i of the corresponding displacements, $d(t_i)$. If the parameters d_0, v_0, and, a are to be estimated using the method of least squares, the form of the matrices would be

$$X = \begin{bmatrix} 1 & t_1 & \frac{1}{2}t_1^2 \\ 1 & t_2 & \frac{1}{2}t_2^2 \\ 1 & t_3 & \frac{1}{2}t_3^2 \\ \vdots & \vdots & \vdots \\ 1 & t_n & \frac{1}{2}t_n^2 \end{bmatrix}, \quad Y = \begin{bmatrix} d(t_1) \\ d(t_2) \\ d(t_3) \\ \vdots \\ d(t_n) \end{bmatrix}, \quad \varepsilon = \begin{bmatrix} \varepsilon_1 \\ \varepsilon_2 \\ \varepsilon_3 \\ \vdots \\ \varepsilon_n \end{bmatrix}, \quad \beta = \begin{bmatrix} d_0 \\ v_0 \\ a \end{bmatrix} \tag{2.40}$$

The vector of responses, Y, consists of the measurements of displacement, the matrix of regressors, X, consists of functions of the measurement times, and the parameter vector, β, consists of the values of d_0, v_0, and, a to be estimated.

The least squares method is also called linear regression since it estimates the coefficients of the regressors which when linearly combined produce estimates of the response. The first subscript of the x's correspond to the measurement index, and the second subscript of the x's correspond to the parameter index. Similarly, the subscript of the ε's and y's correspond to the measurement index. Equation 2.36 can now be rewritten as

$$Y = X\beta + \varepsilon \tag{2.41}$$

and rearranged to isolate the error term.

$$\varepsilon = Y - X\beta \tag{2.42}$$

The sum of the squared error is found by pre-multiplying Eqn. 2.42 by its transpose, yielding

$$\varepsilon'\varepsilon = (Y - X\beta)'(Y - X\beta) \tag{2.43}$$

The parameters that minimize the sum of the squared error can be found by taking the derivative of Eqn. 2.43 with respect to β, setting the result equal to zero, and solving for β. Expanding Eqn. 2.43 yields

$$\varepsilon'\varepsilon = YY' - Y'X\beta - \beta'X'Y + \beta'X'X\beta \tag{2.44}$$

Recognizing that the two middle terms are scalars of equal value, Eqn. 2.44 can be rewritten as

$$\varepsilon'\varepsilon = YY' - 2\beta'X'Y + \beta'X'X\beta \tag{2.45}$$

Taking the derivative with respect to β and setting it equal to zero, yields

$$\left.\frac{\partial \varepsilon'\varepsilon}{\partial \beta}\right|_{\hat{\beta}} = -2X'Y + 2X'X\hat{\beta} = 0 \tag{2.46}$$

where $\hat{\beta}$ is the estimate of the parameters β which solve this equation. Solving for $\hat{\beta}$ yields

$$\hat{\beta} = (X'X)^{-1}X'Y \tag{2.47}$$

It can be shown that the estimated value of the parameters β, have variances described by the covariance matrix

$$Cov(\hat{\beta}) = \sigma^2 (X'X)^{-1} \tag{2.48}$$

where

$$\sigma^2 = \frac{YY' - \hat{\beta}'X'Y}{n-k} \tag{2.49}$$

The individual terms of the covariance matrix can be written as $\sigma^2_{\beta_{ij}}$ which helps to identify the relationship between these terms and the estimates of the parameters.

The covariance matrix can be normalized so that the diagonal terms are equal to one. This normalized matrix is called the correlation matrix and can be used to assess the level of orthogonality between the regressors.

The result of the least squares operation is the extraction of deterministic content, as described by X and $\hat{\beta}$ and quantification of the error by σ^2. Thus the uncertainty in the measurements and the error in the fit have been reduced to a matrix of terms which can be used in subsequent calculations based on the model.

2.5.3 Weighted Least Squares

The application of least squares assumes that the individual error terms share the same variance. When the variance of the error is different for each measurement and the difference can be quantified, we can use the weighted least squares method. The difference can best be described by performing a change of variables such that the new system adheres to the assumptions of the least squares approach. Consider Eqn. 2.36 where the errors, ε_i, are random variables with a mean of zero and unknown variance, but with the relative size of the variances for each ε_i known. This can be described as

$$E(\varepsilon) = 0, \qquad V(\varepsilon) = \sigma^2 V \tag{2.50}$$

where V is an n-by-n matrix. If the errors are uncorrelated, the matrix V will be diagonal. For uncorrelated errors, it can then be shown that V must be non-singular and positive definite, and can therefore be represented as the product of a diagonal matrix K, and its transpose K', which is equal to the original matrix K, as

$$K'K = KK = V \tag{2.51}$$

New variables can now be defined such that the problem can be posed as a least squares problem. Let

$$Z = K^{-1}Y, B = K^{-1}X, G = K^{-1}\varepsilon \tag{2.52}$$

The regression model can now be written in terms of the new variables as

$$Z = B\beta + G \tag{2.53}$$

It can be shown (Montgomery and Peck 1991) that the error in the new system can be described by

$$E(G) = 0, \qquad V(G) = \sigma^2 \tag{2.54}$$

Following the same procedure as used in the least squares approach, estimates of the parameters β and the covariance matrix for β can be shown to be

$$\hat{\beta} = (X'WX)^{-1} X'WY \tag{2.55}$$

and

$$Cov(\hat{\beta}) = \sigma^2 (X'WX)^{-1} \tag{2.56}$$

where

$$W = V^{-1} \tag{2.57}$$

The effect of the unequal variances is that each observation and independent variable is weighted by the inverse of the variance of its error. Measurements with a high variance will have a smaller effect on the model than measurements with a low variance. This is intuitively satisfying since a measurement with a high variance is less reliable than a measurement with a low variance and should therefore have a lower influence on the

estimates of the parameters β. By using the weighted least squares method, it is possible to account for the unequal variances and therefore obtain a model which is more representative of the observations.

2.5.4 Regression Characterization

The results of regression analysis is an estimate of the parameters, β, and the covariance of β. The values of the regression model are equal to the product of the regressors and the parameters

$$\hat{Y} = X\hat{\beta} \tag{2.58}$$

However there are several other quantities that can be used to analyze the regression model. Three of these quantities are the regression sum of squares (*SSR*), error sum of squares (*SSE*), and total corrected sum of squares (*SST*). The quantity *SST* is the sum of the squared difference between each observation and the mean of the observation values. It is a measure of the scatter of the observations. The quantity *SSR* is the sum of squared difference between each fitted value and the mean of the observation values. It is a measure of the information in the observation explained by the regression model. The quantity *SST* is the sum of the squared difference between each observation and the corresponding fitted value. It is a measure of the information in the observations not explained by the regression model. It should be noted that *SSR* and *SSE* are model dependent whereas *SST* is independent of the model selected. These quantities are defined as

$$SSR = \sum_{i=1}^{n} (\hat{y}_i - \bar{y})^2$$

$$SSE = \sum_{i=1}^{n} (y_i - \hat{y}_i)^2 \tag{2.59}$$

$$SST = SSR + SSE = \sum_{i=1}^{n} (y_i - \bar{y})^2$$

These can be written alternatively in matrix form as

$$SSR = \hat{\beta}'X'Y - \left(\frac{1}{n}\right)Y'JY$$

$$SSE = Y'Y - \hat{\beta}'X'Y \tag{2.60}$$

$$SST = SSR + SSE = Y'Y - \left(\frac{1}{n}\right)Y'JY$$

for the general linear regression where n is the number of elements in Y and J is an n-by-n matrix of ones. For the weighted linear regression, we can represent these quantities as

$$SSR = \hat{\beta}'X'WY - \left(\frac{1}{n}\right)Y'K^{-1}JK^{-1}Y$$

$$SSE = Y'WY - \hat{\beta}'X'WY \tag{2.61}$$

$$SST = SSR + SSE = Y'WY - \left(\frac{1}{n}\right)Y'K^{-1}JK^{-1}Y$$

It should be noted that the last term in SSR and SST is independent of the model. The percentage of the observations described by the regression model can be found by dividing SSR by SST. This value is called the sample coefficient of determination and is expressed as

$$r^2 = \frac{SSR}{SST} \tag{2.62}$$

A value of r^2 equal to 1 indicates that the model accounts for all of the response content and that there is no error between the model values and the observations. Thus examination of the sample coefficient of determination reveals the percentage of the response explained by the model. Another value that is calculated is s^2, an estimate of the variance of the error term, σ^2. This value is also known as the means squared error, *MSE*, and is written as

$$MSE = \frac{SSE}{n-k} \tag{2.63}$$

Having outlined the basic concept of weighted least squares, it is now possible to explain how this process is combined with the model selection process.

2.5.5 Model Selection

The weighted least squares method can be used to find estimates of parameters which define a model describing the system under consideration. However the method does not select the model. It only estimates the parameters of the regression model described by the matrix of regressors, *X*. A method is now needed to select the regressors for which the parameters will be estimated. The selection of the appropriate regressors and estimation of the parameters will be called model building in this work.

2.5.5.1 Forward Regression and *F*-test

The general philosophy behind model building is to pick regressors that best describe the phenomena being modeled and then to combine these regressors and find the parameters that relate the regressors to the observations. The procedure used in this study to build the model is forward regression. Forward regression is the process by which regressors are selected from a set of possible regressors and added to the model based on two criteria. First, the regressor which reduces the sum of the squared error between the model and the observations the most is selected. Next, the amount that the sum of the square error is reduced by introducing the new regressor to the model is compared to some minimum value determined by the number of regressors in the model, the number of observations, the sum of the square error with the selected regressor included in the model, and the sum of the square error without the selected regressor included in the model. This is done to ensure that the decrease in the sum of the squared error is significant beyond what is expected as a result of adding a new regressor.

The forward regression procedure begins by defining a pool of possible regressors from which will be chosen candidate regressors to be evaluated for inclusion in the model. Let the number of possible regressors be n_{poss}. The definition of the pool of possible regressors is driven by knowledge of the system being modeled. Once the pool of possible regressors has been defined, each regressor is considered as a candidate regressor and is fit to the observations one at a time resulting in n_{poss} estimates of β, one for each regressor. Next, each of the candidate regressors is evaluated based on the sample coefficient of determination defined in section 2.5.4. The candidate regressor with the largest sample coefficient of determination becomes the current regression model. The current regression

model, X_1, now consists of a single regressor, x_1. Next, the remaining possible regressors are included one at a time with X_1 to form a new possible regression model. Each of the n_{poss}-1 possible regression models are again evaluated based on the coefficient of multiple determination and the model with the largest coefficient of multiple determination is selected as the candidate regression model. A second test is now applied to the candidate regression model before accepting it as the new regression model.

The addition of any regressor to the model will result in an incremental change in the sample coefficient of determination. A test needs to be performed to determine if the increase in r^2 is larger than expected due to the addition of a regressor. The quantity which is used to test the significance of the candidate regression model is the difference between the residual sum of squares of the current model and the candidate model divided by the total sum of squares which is defined as the *f*-value and can be written as

$$f = \frac{SSR_{CANDIDATE} - SSR_{CURRENT}}{MSE_{CURRENT}} \tag{2.64}$$

Substituting the matrix expressions for *SSR* results in

$$f = \frac{\left(\hat{\beta}'X'WY\right)_{CANDIDATE} - \left(\hat{\beta}'X'WY\right)_{CURRENT}}{MSE_{CURRENT}} \tag{2.65}$$

The *f*-value, which is the ratio of two squared variables can be shown to have an *F*-distribution. The *F*-distribution is the distribution of the ratio of two random variables, each having a χ^2-distribution. The calculated *f*-value is now compared to the critical

f-value that determines if the candidate model is indeed better than the current model. The critical f-value is

$$f_{CRITICAL} = f_{\alpha}(1, n-k) \tag{2.66}$$

where α is the confidence level, n is the number of observations, and k is the number of regressors in the candidate model. The current model is replaced by the candidate model if

$$f > f_{CRITICAL} \tag{2.67}$$

The current model now consists of k regressors and parameters. The procedure is repeated until the above condition can not be met. At this point the model has been selected from the pool of possible regressors, and the parameters of the selected model have been computed. A schematic of the forward regression procedure is shown in Fig. 2.14.

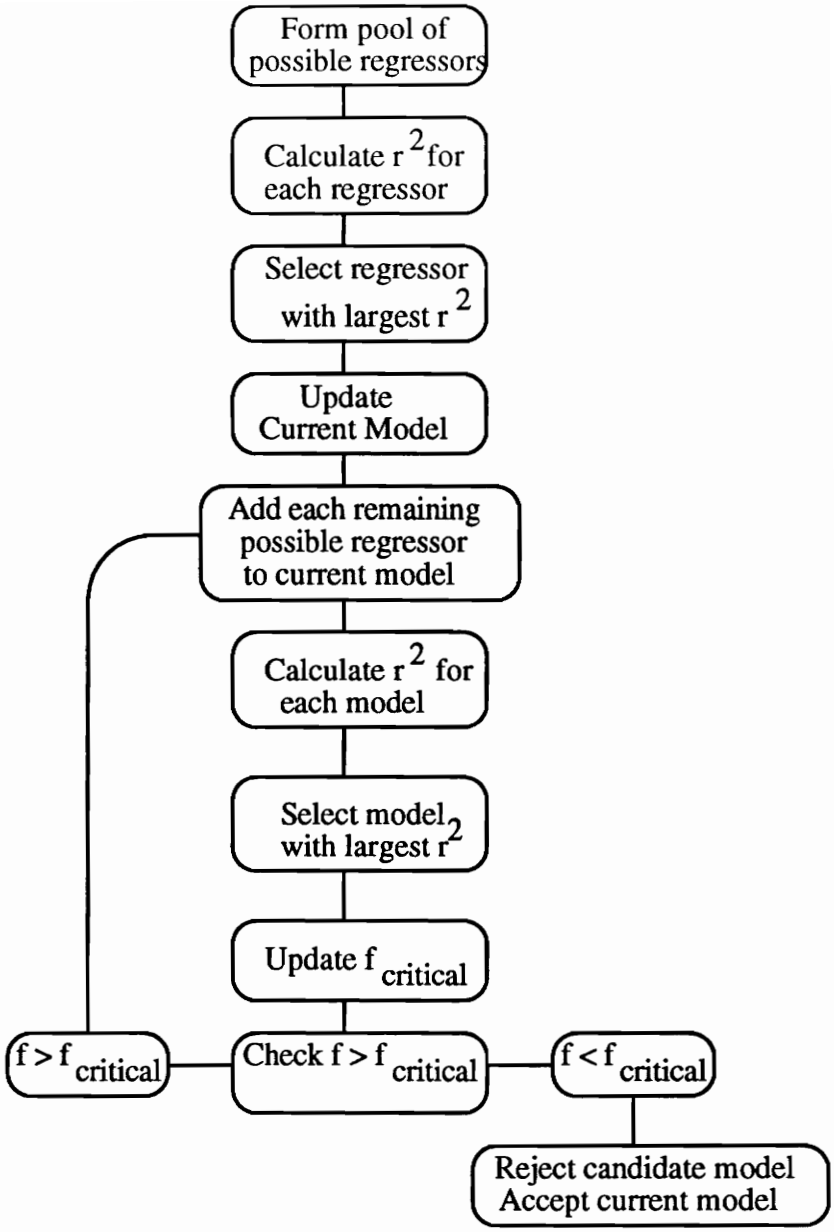

Figure 2.14 Flow Chart for Forward Regression

One of the most important steps in forward regression is the selection of the pool of possible regressors. If too few regressors or regressors of the wrong form are included in the model, the forward regression procedure may not be able to meet the *F*-test requirement. Therefore a systematic approach must be used to determine the pool of possible regressors. The next section discusses the form of the possible regressors followed by a discussion of the procedure used to determine the number of regressors to be included in the pool of possible regressors.

2.5.5.2 Legendré Polynomials

A pool of possible regressors must be defined as the first step of the model selection process. These regressors must be compatible with the observations being modeled. In general, a compatible set of regressors for any one dimensional model is the set of powers of x. Legendré polynomials are a special class of polynomials which are defined on the closed interval [-1,1] and are orthogonal to each other. The first nine Legendré polynomials, written as functions of $\tilde{x}$, are

$$
\begin{aligned}
P_0(\tilde{x}) &= 1 \\
P_1(\tilde{x}) &= \tilde{x} \\
P_2(\tilde{x}) &= \tfrac{1}{2}\left(3\tilde{x}^2 - 1\right) \\
P_3(\tilde{x}) &= \tfrac{1}{2}\left(5\tilde{x}^3 - 3\tilde{x}\right) \\
P_4(\tilde{x}) &= \tfrac{1}{8}\left(35\tilde{x}^4 - 30\tilde{x}^2 + 3\right) \\
P_5(\tilde{x}) &= \tfrac{1}{8}\left(63\tilde{x}^5 - 70\tilde{x}^3 + 15\tilde{x}\right) \\
P_6(\tilde{x}) &= \tfrac{1}{16}\left(231\tilde{x}^6 - 315\tilde{x}^4 + 105\tilde{x}^2 - 5\right) \\
P_7(\tilde{x}) &= \tfrac{1}{16}\left(429\tilde{x}^7 - 693\tilde{x}^5 + 315\tilde{x}^3 - 35\tilde{x}\right) \\
P_8(\tilde{x}) &= \tfrac{1}{128}\left(6435\tilde{x}^8 - 12012\tilde{x}^6 + 6930\tilde{x}^4 - 1260\tilde{x}^2 + 35\right)
\end{aligned}
\tag{2.68}
$$

These functions, evaluated on the closed interval [-1,1] are separated into odd and even orders and plotted in Figures 2.15 and 2.16.

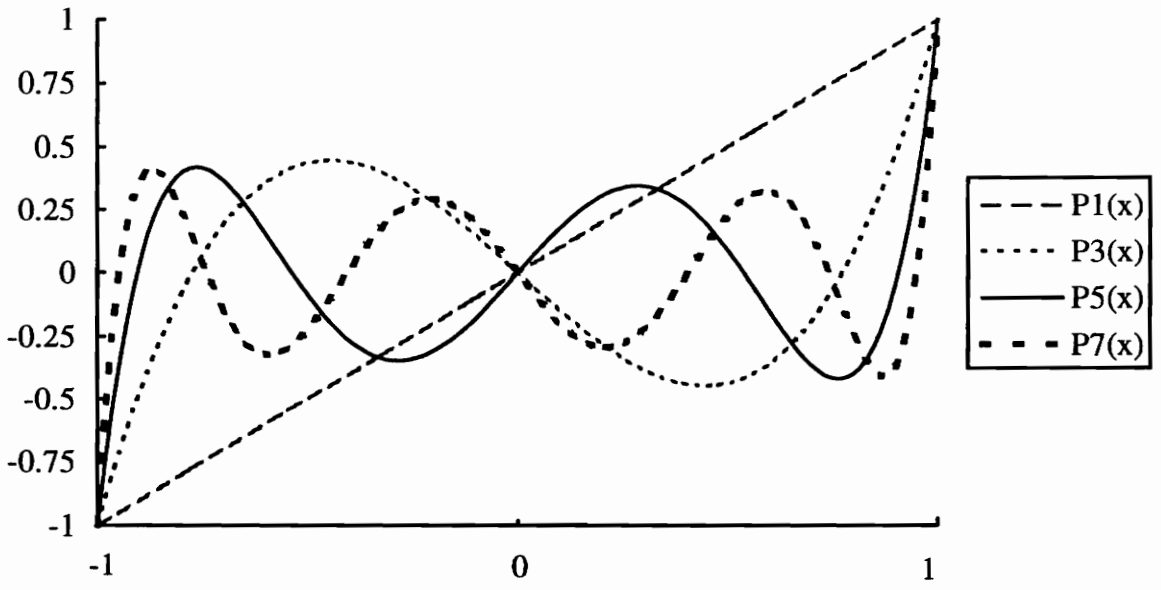

Figure 2.15 Odd Order Legendré Polynomials

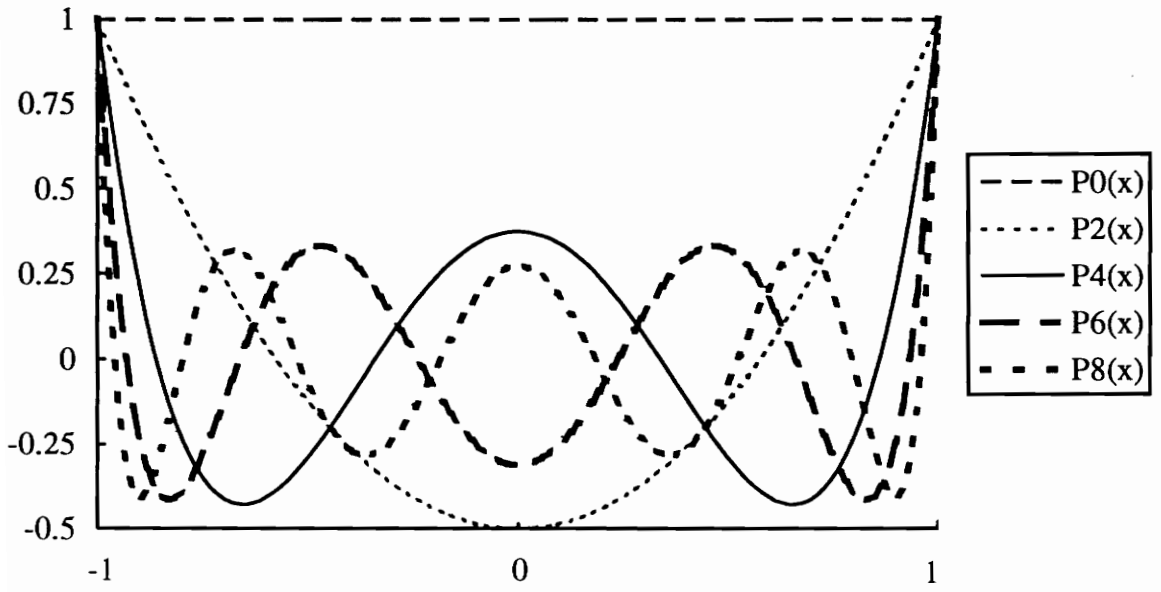

Figures 2.16 Even Order Legendré Polynomials

For the free-free beam used in this study, the deflections, w, are a function of x and y. The possible regressors chosen are the set of surfaces formed by the product of Legendré polynomials in $\tilde{x}$, $P(\tilde{x})$, and Legendré polynomials in y, $P(\tilde{y})$. These surfaces are referred to as Legendré surfaces in this work. Thus the possible regressors are of the form

$$P_{ij}(\tilde{x},\tilde{y}) = P_i(\tilde{x})P_j(\tilde{y}) \tag{2.69}$$

Three dimensional plots of selected surfaces are shown in Figs. 2.17 through 2.23.

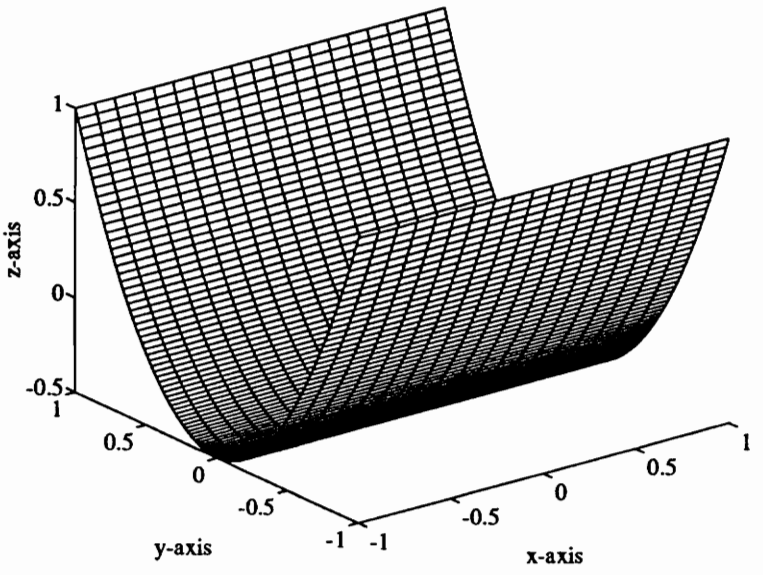

Figure 2.17 Legendré Surface $P_{02}(\tilde{x},\tilde{y})$

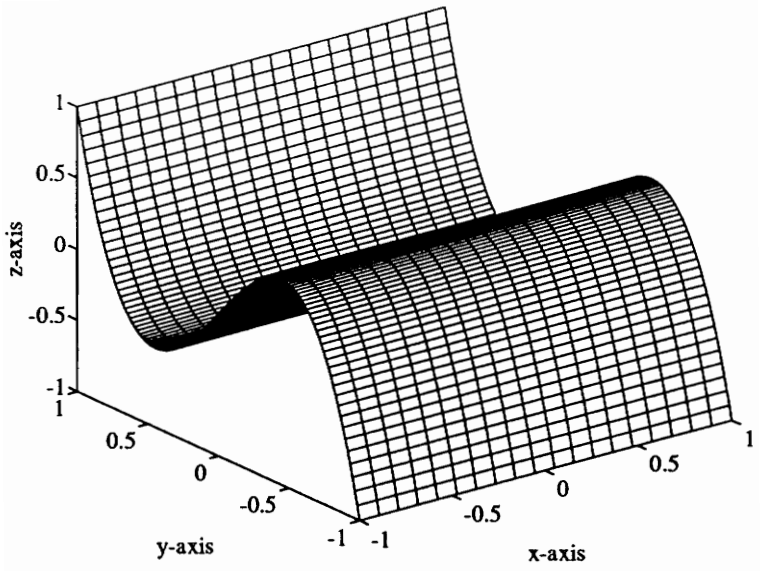

Figure 2.18 Legendré Surface $P_{03}(\tilde{x}, \tilde{y})$

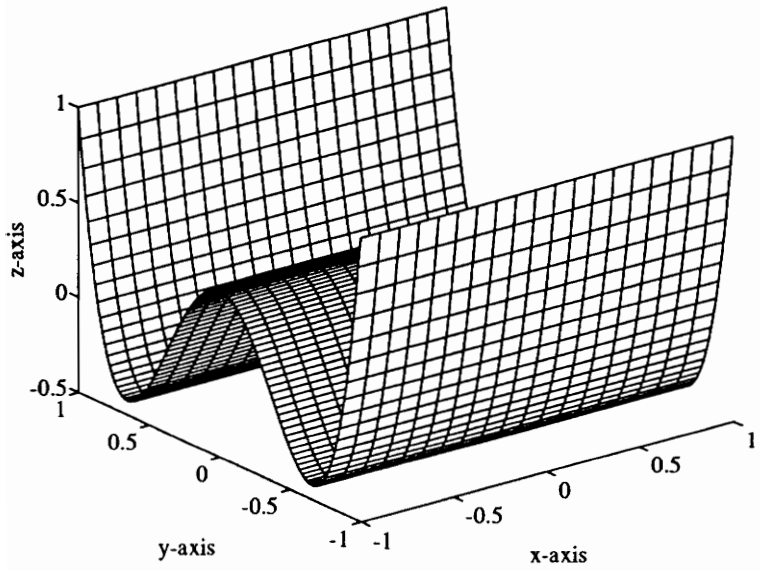

Figure 2.19 Legendré Surface $P_{04}(\tilde{x}, \tilde{y})$

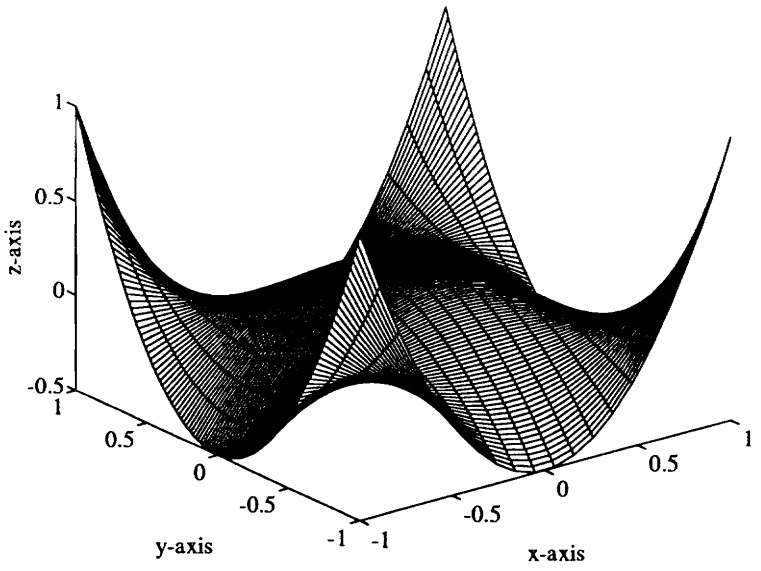

Figure 2.20 Legendré Surface $P_{22}(\tilde{x}, \tilde{y})$

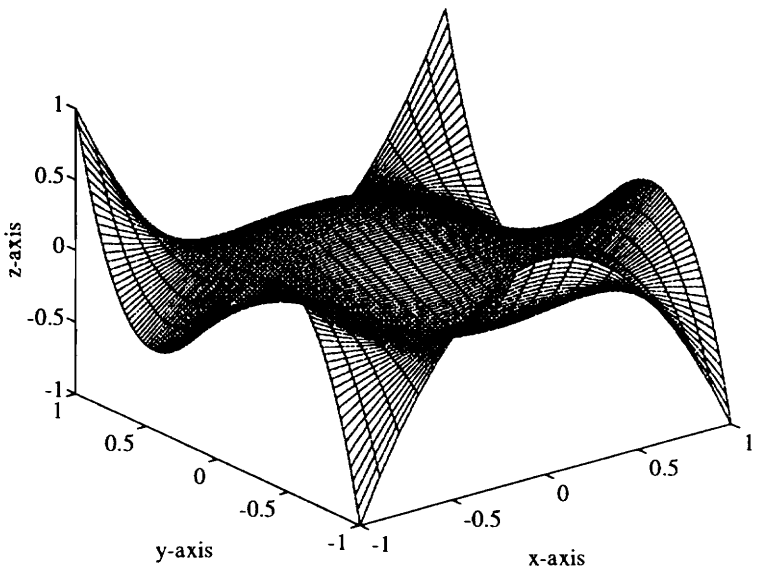

Figure 2.21 Legendré Surface $P_{23}(\tilde{x}, \tilde{y})$

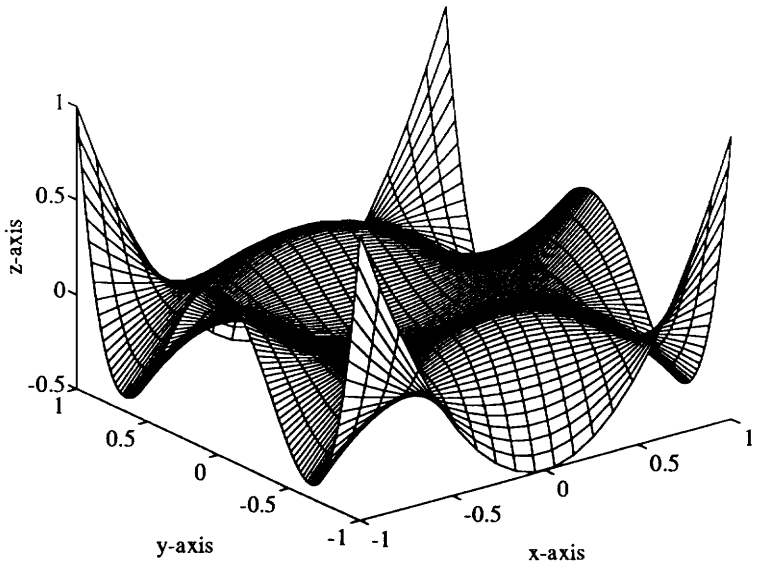

Figure 2.22 Legendré Surface $P_{24}(\tilde{x},\tilde{y})$

Legendré surfaces were selected as the possible regressors for several reasons. First, since the Legendré surfaces are nearly orthogonal, the off-diagonal terms of the correlation matrix will be close to zero with the diagonal terms being close to one. This reduces the effects of errors in the variance estimates due to multi-collinearity. Secondly, the Legendré polynomials are easily generated using the recurrence relation

$$P_{n+1}(\tilde{x}) = 2\tilde{x}P_n(\tilde{x}) - P_{n-1}(\tilde{x}) - \left[\frac{\tilde{x}P_n(\tilde{x}) - P_{n-1}(\tilde{x})}{n+1}\right] \tag{2.70}$$

once $P_0(\tilde{x})$ and $P_1(\tilde{x})$ are defined. Third, the polynomial shapes are similar to the bending modes of free-free beams. The maximum values of the polynomials occur at the endpoints The odd order polynomials are symmetric about the origin, corresponding to

the even beam modes, and the even order polynomials are symmetric about the y-axis, corresponding to the odd beam modes.

In order to use the Legendré surfaces, the measurement locations must be mapped into the closed intervals $\tilde{x}$=[-1,1] and $\tilde{y}$=[-1,1], referred to here as the Legendré space. The mapping is linear, with the four corners of the beam mapped to the four corners of the Legendré space and the number of points between the corners divided into the same number of equal increments as on the beam as shown in Fig. 2.23.

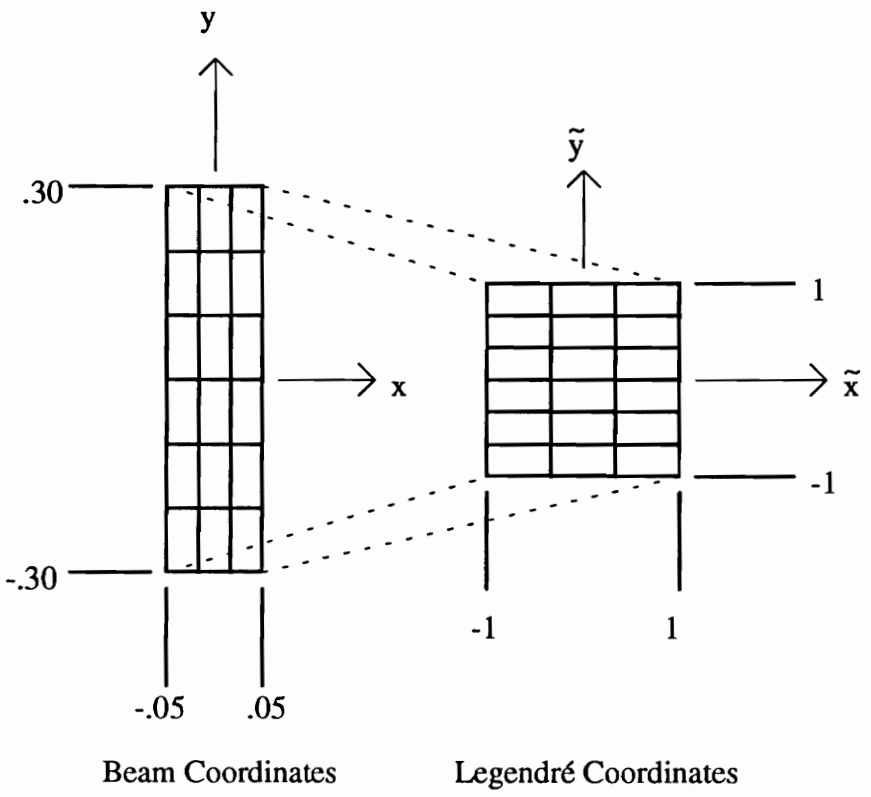

Figure 2.23 Mapping from Beam Coordinates to Legendré Coordinates

The measured voltage at each beam location is transferred to the corresponding point in the Legendré space, and the model selection is performed in the Legendré space. This mapping preserves the value of the measured voltages, however the model must be modified to account for the mapping. This modification is described in a following section.

2.5.5.3 Selection of Possible Regressors

Having determined the desired form of the possible regressors, it is necessary to determine how many regressors should be included in the pool of possible regressors. The approach we take here is to examine the structure of the residual which are defined as the difference between the estimated responses and the measured responses.

For each case, an initial pool of possible regressors compatible with the operating shape was chosen and the forward regression was performed. After the model had been found, a plot of the residuals was generated to determine if there was any structure in the residuals. if structure was found, more regressors were added to the pool of possible regressors and the forward regression was implemented again. This procedure continued until the structure in the residuals was removed.

Figure 2.24 show the residuals for the 265.6 Hz excitation frequency when the pool of possible regressors consisted of all the Legendré surfaces up to $P_{24}(\tilde{x},\tilde{y})$. A slight structure resembling $P_6(\tilde{y})$ is evident. Increasing the order of the pool of possible regressors to $P_{26}(\tilde{x},\tilde{y})$ shows that this structure has been removed as shown in Fig. 2.25. This procedure was implemented for each case.

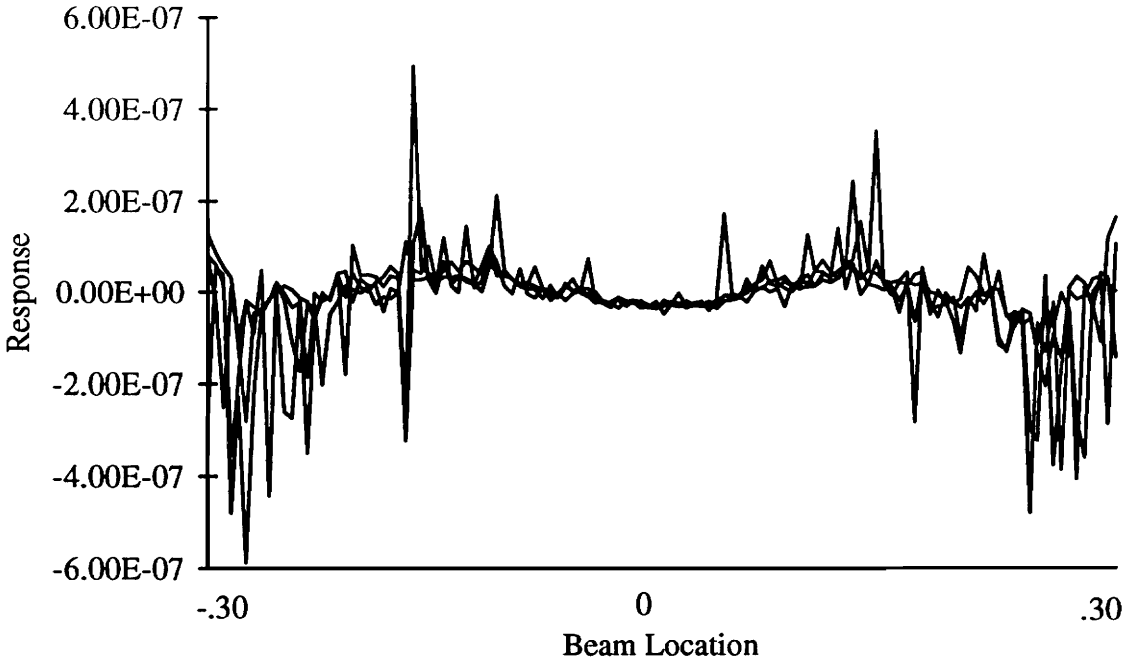

Figure 2.24 Residuals for $P_{24}(\tilde{x}, \tilde{y})$

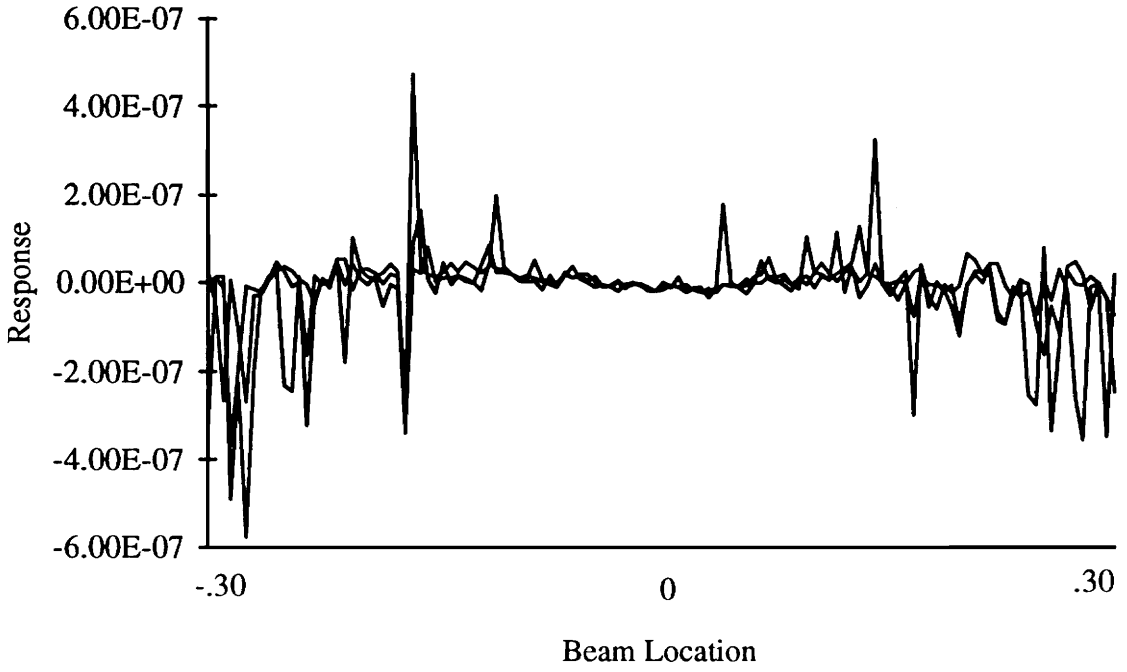

Figure 2.25 Residuals for $P_{26}(\tilde{x}, \tilde{y})$

Applying this procedure to the measured response of the operating shapes, the proper pool of possible regressors was selected for each operating shape.

2.5.5.4 Conversion of Coefficients from Legendré Domain to Measurement Domain

Once the coefficients of the Legendré polynomials corresponding to the best fit have been found, the values must be transformed back into the domain of the true measurement locations in order to correctly calculate the radii of curvature. Recall that the original velocities were mapped from a rectangular space which was .10 m (4 in) wide and .61 m (24 in) long into the Legendré space which spans [-1,1] in both the $\tilde{x}$ and y directions. Therefore, the locations in the Legendré space are related to the locations on the beam according to,

$$\begin{aligned} \tilde{x} &= \frac{1}{.05} x \\ \tilde{y} &= \frac{1}{.3} y \end{aligned} \tag{2.71}$$

It is desired to have the model as a function of the true locations in terms of powers of x and y. The easiest way to accomplish this is to first collect the coefficients for each $\tilde{x}^i \tilde{y}^j$ term, and then convert the coefficients and variances from the Legendré domain to coefficients and variances of the coefficients of $x^i y^j$ according to the rules governing linear combinations of random variables. At this point, we have available a continuous model which relates the beam response to the beam location at any point on the structure.

2.5.6 Propagation of Uncertainty for Poisson's Ratio

Having found the model for the deflection of the beam and converted the results to the domain of the true positions, it is now possible to determine estimates for Poisson's ratio and the corresponding uncertainty. The resulting coefficients for the structure deflection consist of mean values of β_i and the corresponding variance and covariance terms from the covariance matrix, $\sigma^2_{\beta_{ij}}$, of the deflection shape. The resulting coefficients, variances, and covariances can be used to calculate the transverse and anticlastic radii of curvature and Poisson's ratio at any location, again applying the rules for linear combinations of random variables and the relationship for the propagation of uncertainty presented in Beckwith, *et al.* (1993). At this point, values are available for the local value of Poisson's ratio and the associated variance of the local value. Once the local values of Poisson's ratio and the associated variances are calculated, a weighted least squares procedure is applied to obtain a global value and variance for Poisson's ratio, under the assumption that Poisson's ratio is constant over the structure.

2.6 Summary

The methods for estimating local and global values of Poisson's ratio have been presented. We also reviewed the necessary background information. It is now possible to describe the experimental techniques used to implement this procedure.

Chapter 3

Experiment Description

3.1 Introduction

The theoretical development of the method used to estimate Poisson's ratio was presented in the previous chapter. It was shown that, beginning with a velocity profile consisting of measurements of velocity and the variance of the measurements at discrete points on the structure, it is possible to arrive at estimates, as well as confidence intervals, of Poisson's ratio. The scanning laser velocimeter is capable of efficiently measuring the velocity and variance of the velocity of structures at discrete points which provides the needed information. In this chapter, we describe the operating principles of the scanning laser velocimeter, the experiment setup, the data acquisition system, and the subsequent processing involved in obtaining the velocity profile of a structure, including the uncertainty.

3.2 Scanning Laser Doppler Velocimeter

The scanning laser Doppler velocimeter measures the velocity of a structure based on the Doppler shift of the light reflected from the structure. The velocimeter consists of a laser head which generates a coherent, single frequency light beam, mirrors for pointing the light beam, optics for splitting the light beam, photo-detectors for measuring the reflected light beam, and electronics for extracting the structure velocity from the reflected light beam. After exiting the laser head, the light beam is split into three separate beams. Two are used as reference beams for extracting the velocity from the reflected light beam. The

third is reflected by several mirrors to the opening in the front of the velocimeter enclosure. Two of the mirrors, allowed to pivot, are driven by galvanometers. The application of a voltage to the galvanometers results in deflection of the mirrors and subsequently the deflection of the laser beam. By varying the voltages applied to the galvanometers, the light beam can be scanned over the structure. The laser deflection is specified by two rotation angles, θ_x, rotation about the laser's x-axis, and θ_y, rotation about the laser's y-axis. The mirrors' allow a deflection range of ±25° in both the x and y directions.

Once the laser beam has been directed to the selected point on the structure, the velocimeter is able to measure the point velocity. The projected light strikes the structure and is reflected back to the velocimeter after being frequency-modulated by the motion of the structure. The projected light serves as the carrier signal and the structure velocity in the direction of the laser beam is the modulating signal. Thus, the reflected light beam contains the necessary information for determining the velocity of the structure. In the next two sections, the background material for determining the true structure velocity and extracting the true structure velocity from the modulated signal are presented.

3.2.1 Geometric Considerations

The projected light is modulated by the velocity of the structure in the direction of the laser beam, but we are interested in determining the velocity normal to the structure. If the projected light beam is not collinear with the structure velocity, the reflected light beam is modulated by a component of the structure velocity. The measured velocity of the velocimeter will therefore not be the structure velocity normal to the structure. In

general, three velocity measurements of each point on the structure are necessary to resolve the true structure velocity. These three measurements must be taken from different location such that the lines from the structure to the laser origin are not parallel. This can be demonstrated using a two-dimensional model.

Consider the velocity of point A, V_A, in Fig. 3.1.

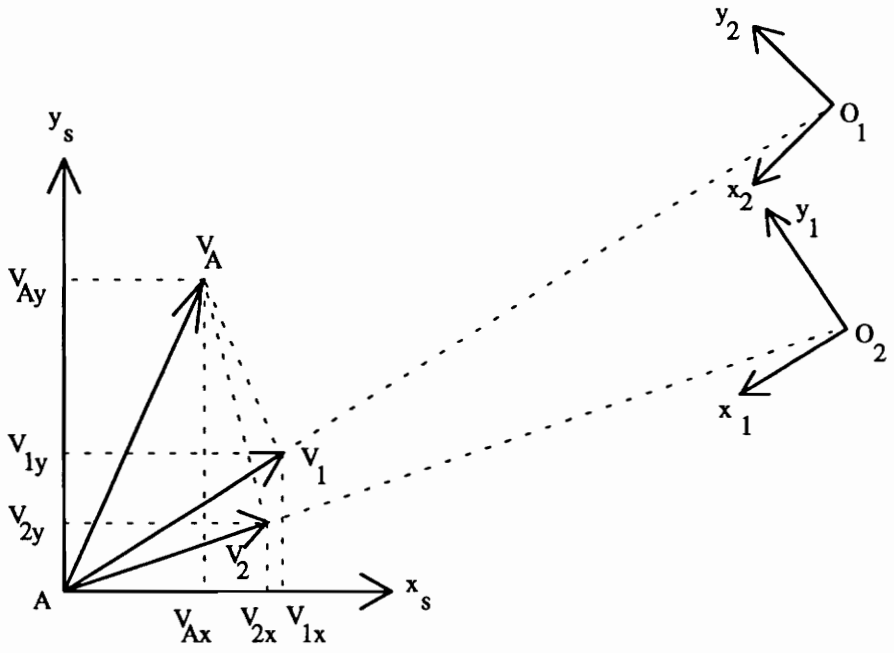

Figure 3.1 Geometry of Multiple Velocity Measurements

In order to determine the true velocity, V_A, the x and y components in the structure coordinate system must be found. If a single measurement is taken along the line AO_1, this measured velocity, V_1, is equal to the dot product of V_A with a unit vector along AO_1, defined as N_1. The dot product can be represented as

$$V_1 = V_{Ax} \cdot N_{1x} + V_{Ay} \cdot N_{1y} \tag{3.1}$$

where N_{1x} and N_{1y} are the x and y components of the unit vector N_1. It is easily seen that it is impossible to determine the two unknowns, V_{Ax} and V_{Ay}, from a single equation. However by taking a second measurement, V_2, and performing the same operations, two equations are available for solving the two unknowns. The resulting set of equations, written in matrix form, is

$$\begin{bmatrix} V_1 \\ V_2 \end{bmatrix} = \begin{bmatrix} N_{1x} & N_{1y} \\ N_{2x} & N_{2y} \end{bmatrix} \begin{bmatrix} V_{Ax} \\ V_{Ay} \end{bmatrix} \tag{3.2}$$

where N_{2x} and N_{2y} are the x and y components of the unit vector N_2 along the line AO_2.

The result is similar for resolving the three dimensional velocity, requiring three measurements of the velocity at each point and the solution of three equations with three unknowns.

One complication is determining the directions of V_1 and V_2 in the structure coordinate system. The directions are a function of the location and orientation of the velocimeter coordinate system relative to the structure coordinate system and the deflection angle of the laser beam. This, along with determining the location and orientation of the velocimeter coordinate system relative to the structure coordinate system, is the registration and reconstruction problem. In general the solution of the registration and reconstruction problem requires the solution of a set of non-linear equations. This subject is discussed extensively in Zeng, *et al.* (1993).

For this study it was assumed that the velocity of all points on the structure were normal to the x-y plane and the laser's z-axis was collinear with the structure's z-axis as shown in Fig. 3.2. The structure coordinate system, subscripted with an S, is fixed to the center of the structure with the xy-plane parallel to the structure and the z-axis directed out of the structure on the side facing the velocimeter. The laser coordinate system, subscripted with an S, is fixed to the velocimeter with the z-axis pointing out of the front of the velocimeter enclosure.

The first assumption is justified by the fact that the structures out-of-plane motion is much larger than the in-plane motion. The second assumption can be justified through careful alignment of the structure and velocimeter.

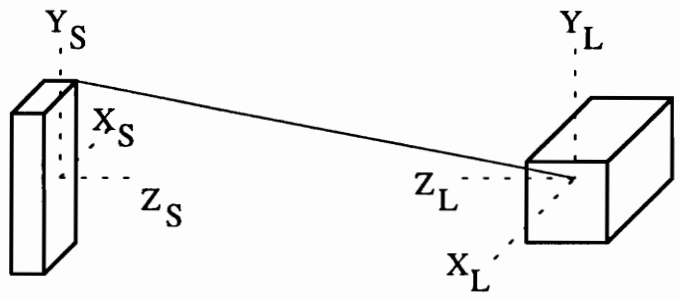

Figure 3.2 Orientation of Velocimeter to Structure

Under these assumptions the translation of the measured velocity in the laser beam direction to the true structure velocity is simplified. The true velocity of the structure, V_S, is related to the measured velocity, V_M, by

$$V_S = \frac{V_M}{\cos(\theta_x)\cos(\theta_y)} \tag{3.3}$$

as shown in Fig. 3.3.

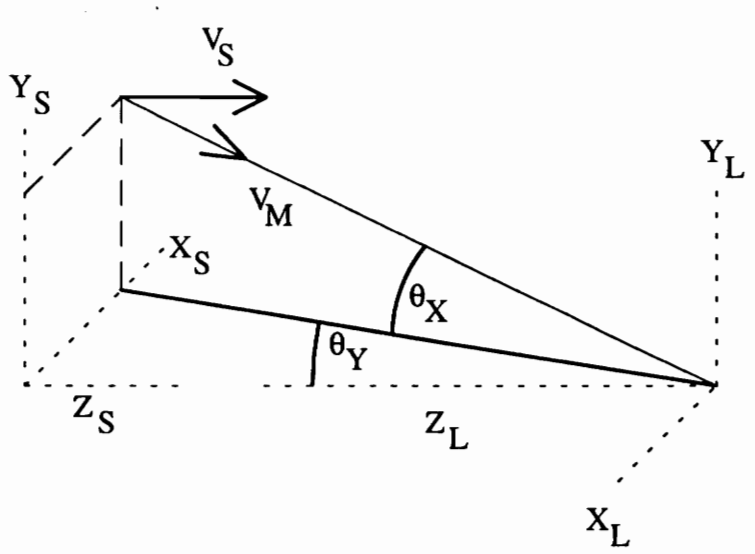

Figure 3.3 Geometry of Structure Velocity and Measured Velocity

Since the output of the velocimeter is a voltage proportional to the measured velocity, the true structure velocity in terms of the output voltage, v_m, and laser deflection angles is

$$V_S = K\frac{v_m}{\cos(\theta_x)\cos(\theta_y)} \tag{3.4}$$

where K is the conversion factor for voltage to velocity. Therefore, it is possible to determine the structure velocity, under the stated assumptions, from the voltage output of the laser velocimeter.

Not only is it necessary to know the velocity of the structure, but also the location of the point being measured. Knowing the deflection angle of the mirrors, the distance from the laser to the structure and orientation of the laser with respect to the structure, it is possible to determine the location of the measurement in the laser coordinate system. The software used for controlling the laser deflection requires the user to locate the four corners of the beam. Each corner is described by a set of two laser deflection angles, θ_x and θ_y. The intermediate points are found by dividing the included angle into a number of user specified equal angles. Thus the measurement locations are not equal distances apart, but equal angular deflections apart as shown in Fig. 3.4.

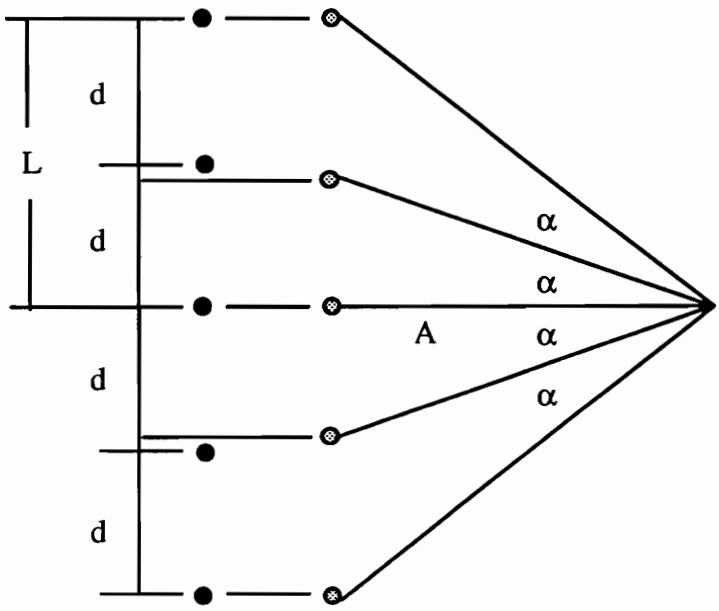

Figure 3.4 Equal Distance Versus Equal Angle Measurement Locations

For an arrangement similar to Fig. 3.4 where $2n$ is the number of measurements locations, and $2L$ is the total distance over which the measurements will be taken, and the

measurements will be taken at positions resulting from equal angular deflections, the distance of the i-th measurement point from the zero deflection position is given by

$$e_i = \tan\left(i \cdot \frac{\tan^{-1}\left(\frac{L}{A}\right)}{n} \right) \cdot A \tag{3.5}$$

Had the measurement been taken at equally spaced distances, the location of the i-th measurement above the zero deflection line would be

$$d_i = \frac{L}{n} \cdot i \tag{3.6}$$

In this study, A is approximately 3m (118 in), the distance over which the measurements were taken are .61m (24 in) in the y-direction and .15m (6 in) in the x-direction. Using these values, the percent error, defined as

$$\%error = \frac{d_i - e_i}{d_i} \tag{3.7}$$

in the location of the vertical and horizontal directions, can be evaluated. These errors are shown in Figs. 3.5 and 3.6.

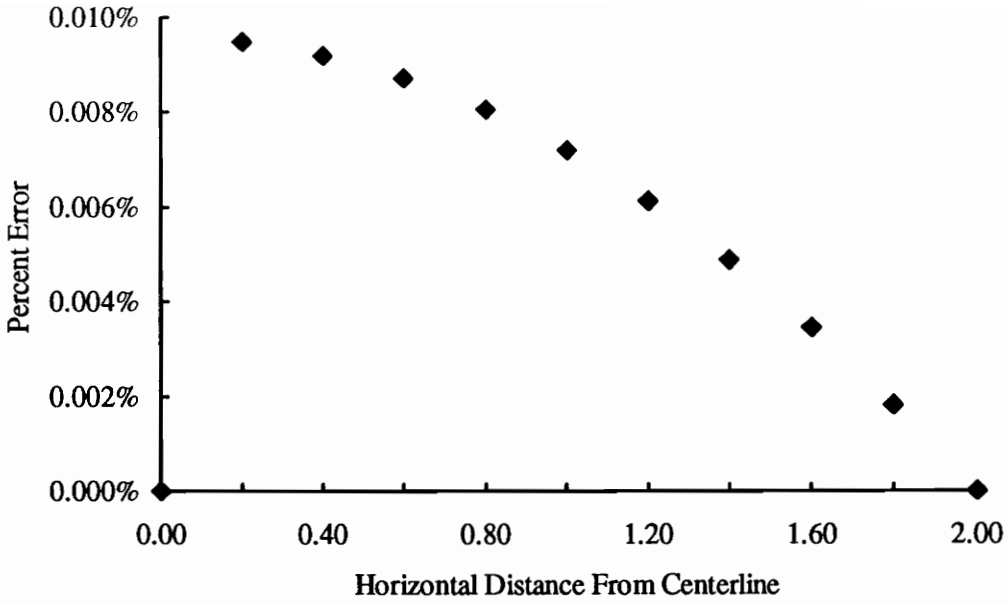

Figure 3.5 Percent Error for Horizontal Measurement Locations

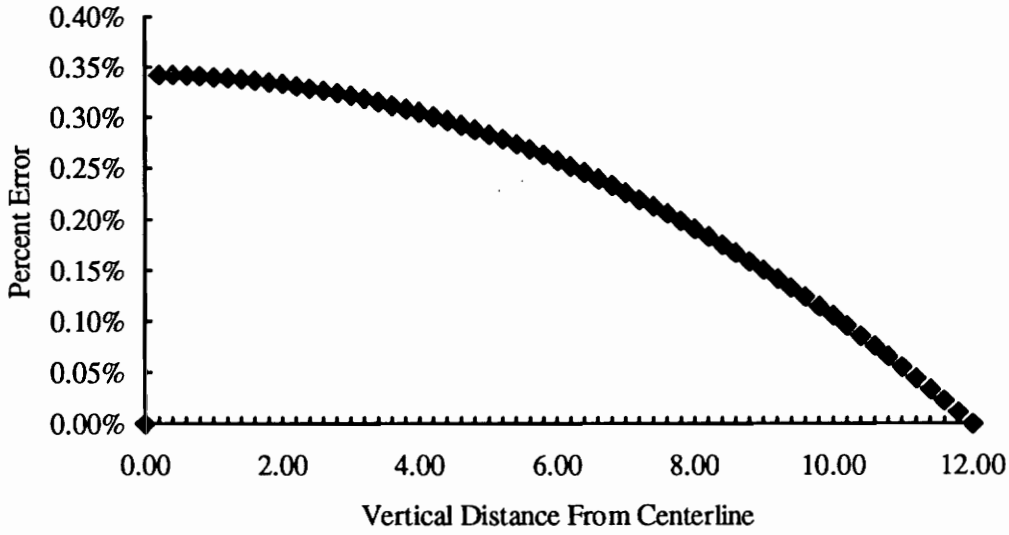

Figure 3.6 Percent Error in Vertical Measurement Locations

From Figs. 3.5 and 3.6, we can see that the error in assuming that the measurements were taken at equally spaced locations on the structure is insignificant. Therefore, in this study,

it was assumed that the measurements were taken at equally spaced locations on the structure.

3.2.2 Operating Principle

The operating principle of the laser Doppler velocimeter draws on the fields of optics and electronics, and although the principle has been described in various levels of detail and completeness, (Drain, 1980, Ometron, 1987) an intermediate description of the operating principle is presented here to introduce those unfamiliar with the technique. The measurement of the velocities using the laser velocimeter centers around the modulation of a laser beam by the structure under investigation, detection of the frequency modulated light beam, and extraction of the velocity signal's magnitude and direction from the modulated signal.

The laser velocimeter used in this study is a Velocity Profile Imaging (VPI) Sensor manufactured by Ometron Limited. The laser is a Class II helium-neon type with a power output of less than 1mW, posing a minimum risk of eye damage due to accidental direct exposure to the laser beam. The velocimeter includes mirrors for aiming the laser beam, and optics and electronics for detection and extraction of the velocity.

The measurement procedure begins with the projection of coherent laser light onto a moving structure. The electromagnetic field of projected light is represented by

$$E_p(t) = E_p \cos(2\pi f_0 t) \tag{3.8}$$

where E_p is the amplitude and f_o the frequency of the projected light. For the helium-neon laser in the VPI Sensor, f_o is equal to 473.8 THz. Prior to emerging from the velocimeter enclosure, the projected light beam is split to for two additional beams which are used as reference beams during the velocity extraction process. The projected light beam is frequency modulated by the motion of the structure before being reflected back to the velocimeter. If the structure is moving away from the velocimeter, the reflected light will be of a frequency less than the frequency of the projected light. If the structure is moving towards the velocimeter, the reflected light will be of a frequency greater than the frequency of the projected light. Figure 3.7 depicts the modulation of the carrier signal by a structure moving towards and away from the velocimeter.

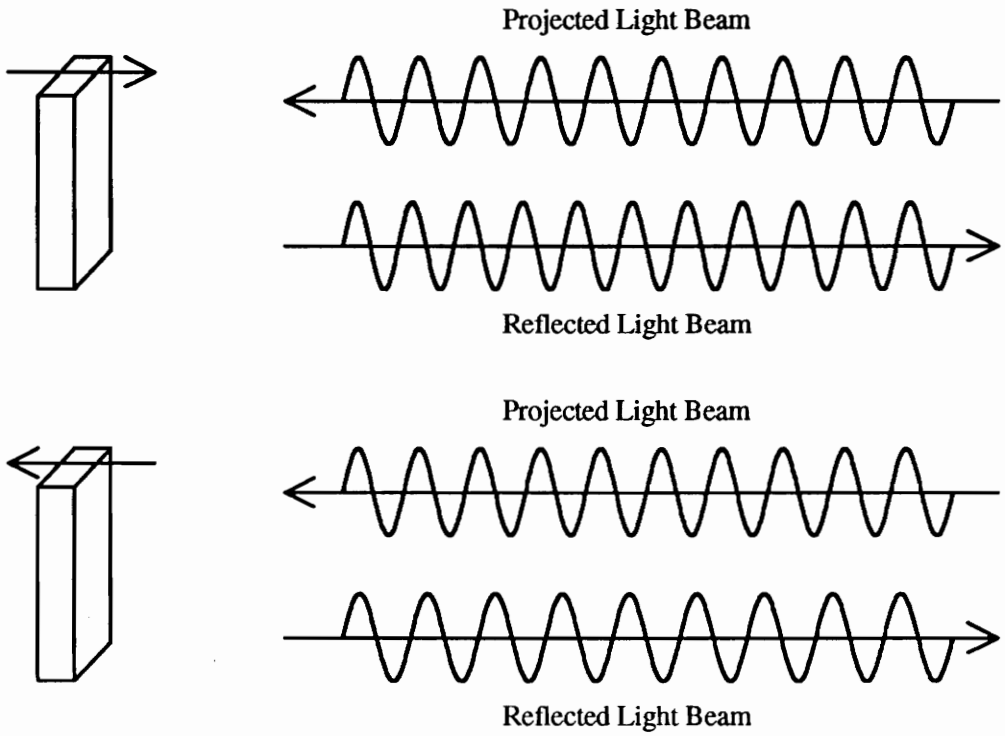

Figure 3.7 Modulation of Laser Beam by Structure Velocity

The reflected light beam, expressed as an electromagnetic field, will be of the form

$$E_r(t) = E_r \cos(2\pi(f_0 + \Delta f)t + \phi) \tag{3.9}$$

where E_r is the amplitude of the reflected light, Δf is the change in frequency due to the motion of the structure, and ϕ is the phase angle between the projected and reflected light beams. The change in frequency, Δf_O, occurs about the frequency of the projected light, f_O. In order to extract the measured velocity of the structure, this signal must be manipulated in order to extract the magnitude of the measured velocity and the phase angle relative to the force. This extraction is a multi-step process which is outlined below. Figure 3.8 illustrates the extraction of the measured velocity signal from the frequency modulated signal.

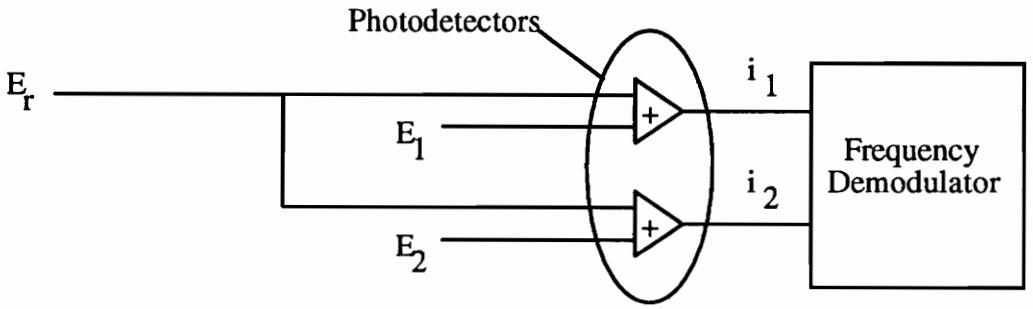

Figure 3.8 Velocity Extraction

After entering the velocimeter enclosure, the reflected beam is split into two beams. Next the reflected frequency modulated light is homodyned, or added to, the two reference beams split from the projected light beam. The first reference beam, which is represented by

$$E_1(t) = E_1 \cos(2\pi f_0 t) \tag{3.10}$$

has the same frequency as the projected light with a 0° phase difference. The second reference beam is first shifted by 90°, resulting in

$$E_2(t) = E_2 \sin(2\pi f_0 t) \tag{3.11}$$

before being mixed with the reflected light. The results of the mixing of the two reference beams with the reflected light are

$$\begin{aligned} E_{1M}(t) &= E_1 \cos(2\pi f_o t) + E_r \cos(2\pi(f_0 + \Delta f)t + \phi) \\ E_{2M}(t) &= E_2 \sin(2\pi f_o t) + E_r \cos(2\pi(f_0 + \Delta f)t + \phi) \end{aligned} \tag{3.12}$$

These two light beams are then measured by two photodetectors, one for each beam. The photodetectors produce a current proportional to the square of the amplitude of the electromagnetic field. Due to the limitations of the photodetectors, the high frequency component of the homodyned signal is not detected. Therefore the current output of the photodetectors are

$$\begin{aligned} i_1(t) &= \frac{1}{2}E_r^2 + \frac{1}{2}E_1^2 + E_r E_1 \cos((2\pi\Delta f)t + \phi) \\ i_2(t) &= \frac{1}{2}E_r^2 + \frac{1}{2}E_2^2 - E_r E_2 \sin((2\pi\Delta f)t + \phi) \end{aligned} \tag{3.13}$$

The first two terms in each signal are DC. components, which can be filtered out. The last term of each signal is a sinusoid with frequency which vary about zero frequency.

$$\begin{aligned} i_1(t) &= E_r E_1 \cos((2\pi\Delta f)t + \phi) \\ i_2(t) &= -E_r E_2 \sin((2\pi\Delta f)t + \phi) \end{aligned} \tag{3.14}$$

The need for obtaining two signals can now be presented. Consider the case where the only signal available is $i_1(t)$. If the structure is moving towards the velocimeter, the change in frequency will be positive. If the structure is moving away from the structure the change in frequency will have the same magnitude but will be negative. As a result of the trigonometric identities

$$\begin{aligned} \cos(-\alpha) &= \cos(\alpha) \\ \sin(-\alpha) &= -\sin(\alpha) \end{aligned} \tag{3.15}$$

it is not possible to discern if the structure velocity is positive or negative since the frequency change is the same whether the velocity is positive or negative. However by using the technique of mixing with two reference signals it is possible to determine the magnitude as well as the direction. The direction can be found by based on the phase relationship between $i_1(t)$ and $i_2(t)$, The final step is to send the two current signals to frequency shifter and frequency demodulator which produces an output signal proportional to and in phase with the modulating signal, which is the structure velocity.

3.2.3 Laser Control and Data Acquisition

Besides measuring the velocity at each point on the structure, a method is needed to capture and store the signal at each of the many measurement locations. This data acquisition task is accomplished using an A/D converter controlled by a MacIntosh IIFx. The structure is assumed to behave linearly in frequency, meaning that the response will have the same frequency as the excitation. The data acquisition system is used to determine the magnitude of the velocity and the phase relationship between the velocity and the force.

The required information is found by sampling the force and velocity signals and finding the magnitude and phase relationship between the two by applying linear regression. The response will be of the same frequency as the excitation with some magnitude ratio and phase shift. For a given location on the structure, the velocity can be represented as

$$V_m(t) = A\cos(\omega_o t) + B\sin(\omega_o t) \tag{3.16}$$

and the force can be represented by

$$F(t) = C\cos(\omega_o t) + D\sin(\omega_o t) \tag{3.17}$$

The data acquisition program is configured to sample a specific number of points per waveform, n_p, over a specific number of wave forms, n_w resulting in a total sample record of n points where

$$n = n_p \cdot n_w \tag{3.18}$$

The n data points for force and velocity are then regressed using the linear least squares method discussed in Chapter 2. The general linear regression equations are

$$\begin{bmatrix} V(t_1) \\ V(t_2) \\ \vdots \\ V(t_n) \end{bmatrix} = \begin{bmatrix} \cos(\omega_o t_1) & \sin(\omega_o t_1) \\ \cos(\omega_o t_2) & \sin(\omega_o t_2) \\ \vdots & \vdots \\ \cos(\omega_o t_n) & \sin(\omega_o t_n) \end{bmatrix} \begin{bmatrix} A \\ B \end{bmatrix} + \begin{bmatrix} \varepsilon_{V1} \\ \varepsilon_{V2} \\ \vdots \\ \varepsilon_{Vn} \end{bmatrix} \tag{3.19}$$

$$\begin{bmatrix} F(t_1) \\ F(t_2) \\ \vdots \\ F(t_n) \end{bmatrix} = \begin{bmatrix} \cos(\omega_o t_1) & \sin(\omega_o t_1) \\ \cos(\omega_o t_2) & \sin(\omega_o t_2) \\ \vdots & \vdots \\ \cos(\omega_o t_n) & \sin(\omega_o t_n) \end{bmatrix} \begin{bmatrix} C \\ D \end{bmatrix} + \begin{bmatrix} \varepsilon_{F1} \\ \varepsilon_{F2} \\ \vdots \\ \varepsilon_{Fn} \end{bmatrix} \tag{3.20}$$

Once the force and velocity signals have been fitted, estimates of the coefficients as well as estimates of the variance of the coefficients can be found as discussed in Section 2.5.2. The magnitude of the force and velocity can now be found from

$$\begin{aligned} |V| &= \sqrt{A^2 + B^2} \\ |F| &= \sqrt{C^2 + D^2} \end{aligned} \tag{3.21}$$

and the phase angles can be found from

$$\phi_V = \tan^{-1}\frac{|A|}{|B|},\ \phi_F = \tan^{-1}\frac{|C|}{|D|} \tag{3.22}$$

where the phase angles are referenced to the first sample of the sample record.

The force and velocity can now be represented as

$$\begin{aligned} V(t) &= \sqrt{A^2 + B^2}\cdot\sin(\omega_o t + \phi_V) \\ F(t) &= \sqrt{C^2 + D^2}\cdot\sin(\omega_o t + \phi_F) \end{aligned} \tag{3.23}$$

For each sample block corresponding to a different point on the structure, the phase angles of the force and velocity and the velocity magnitude will be different, whereas the force amplitude is independent of velocity measurement location. The velocity referenced to the force signal can than be represented as

$$V(t) = \sqrt{A^2 + B^2}\cdot\sin(\omega_o t + (\phi_F - \phi_V)) \tag{3.24}$$

Therefore at each location the measurement is equivalent to the velocity magnitude and the phase angle between the force and velocity. For lightly damped structures with widely spaced modes the phase angle will be ±90° off-resonance and 180° or 0° on resonance. The magnitude and phase are transformed into real and imaginary parts according to the relations

$$V_R = \sqrt{A^2 + B^2} \cdot \cos(\phi_F - \phi_V)$$
$$V_I = \sqrt{A^2 + B^2} \cdot \sin(\phi_F - \phi_V) \tag{3.25}$$

Positive and negative real velocities correspond to force-velocity phase relationships of 0° and 180° respectively, and positive and negative imaginary velocities correspond to a force velocity phase relationship of +90° and -90° respectively.

Following calculation of the above parameters, the data acquisition program writes to a file the following quantities: θ_x, θ_y, the voltages corresponding to V_R, V_I, $|F|$, and $\sigma^2_{|V|}$. These quantities serve as the starting point for the subsequent model regression and Poisson's ratio estimation.

3.3 Equipment Setup

The use of the scanning laser velocimeter requires several other pieces of equipment. This section describes the setup and the function of each component. The first component of the experimental setup is the structure to be tested. For this study the structure was a free-free aluminum beam .61 m (24 in) long, .10 m (4 in) wide, and .02 m (.75 in) thick. The beam was suspended from an overhead support using bungee cord and fishing line. The beam was excited by an electromechanical shaker which was also suspended form the overhead support using bungee cord. A force transducer was attached to the structure at the point of excitation and coupled to the shaker with a stinger. The excitation point was mid way along the width of the beam along the top edge. The scanning laser velocimeter

was placed approximately 3 m away aligned with the structure as described in section 3.2. A diagram of the setup is shown in Fig. 3.9.

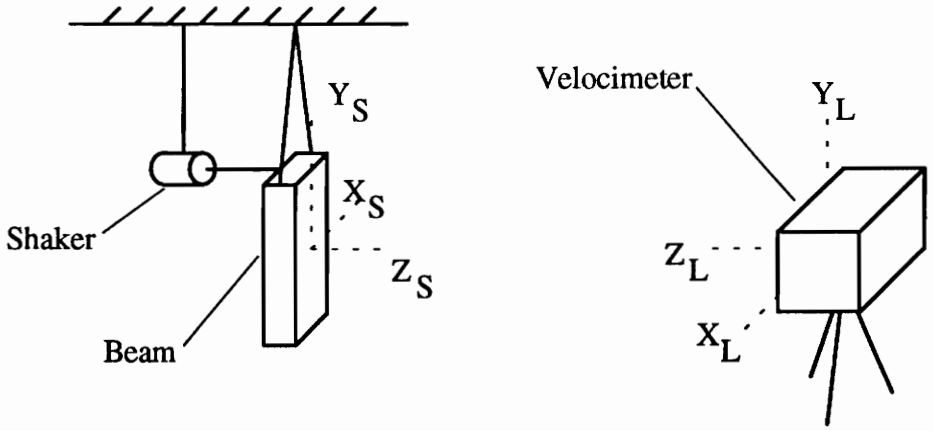

Figure 3.9 Velocimeter and Structure Setup

Equipment is also needed to drive the shaker, measure the force input to the structure, condition the velocimeter signals, and monitor the signals. A schematic of this equipment is shown in Fig. 3.10.

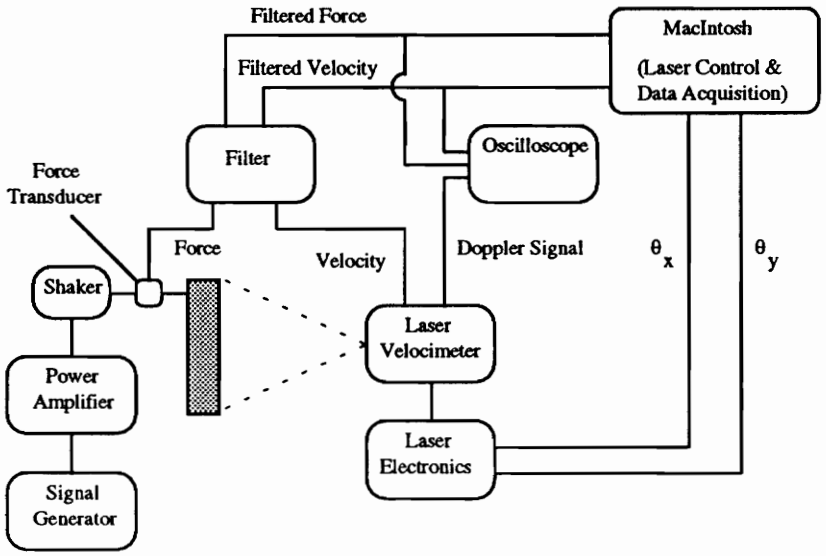

Figure 3.10 Equipment Schematic

The excitation signal was generated using a Hewlett Packard 3324A Synthesized Function/Sweep Generator. The output of the signal generator was sent to a Harmon Kardon HK770 Power Amplifier to supply the necessary current for driving a Ling Dynamics shaker. The shaker acted through a short stinger, and a Kistler Piezotron Force Transducer (Model 9712A50), whose output was sent through a PCB force transducer power unit (Model 480DO9). The scanning laser velocimeter is a Velocity Profile Imager (VPI) Sensor manufactured by Ometron, Limited. The velocity and the force signals were sent through a pair of matched bandpass filters (Frequency Devices Model 9016 Multi-Channel filter). The multi-channel filter contains two matched high-pass and two matched low-pass Butterworth filters which were connected in series, resulting in two matched bandpass filters. Matched filters ensure that the phase relationship between the force and velocity signals will be preserved. The Frequency Devices Filter also provides gain for matching the force and velocity signal levels to the input range of the A/D boards.

The filtered force and velocity signals, along with the Doppler signal, were displayed on a Tektronix Model 2214 Digital Oscilloscope. The filtered force and velocity signals were connected to a National Instruments NB-A2000 located in the MacIntosh. The NB-A2000 is a 12-bit A/D board with a fixed input range of ±5V. The gain on the bandpass filters was selected to utilize the full input range of the A/D board to minimize the effect of quantization error. A National Instruments NB-AO-6 D/A board, also located in the MacIntosh, was connected to the Ometron unit for supplying the control signals for laser beam deflection. The mirror control and data acquisition operation control was performed by MDI10, a LabVIEW Virtual Instrument developed by the Modal Analysis Lab at Virginia Tech.

The laser control and data acquisition program was configured to measure the velocity profile at locations on the structure corresponding to the points on a rectangular grid 20 points wide by 120 point long, resulting in 2400 measurement locations. This grid, referred to as the scan area, extended to the four edges of the beam and was aligned with the structure so that the structure and scan area edges where parallel. At each measurement location, 64 measurements were made of the velocity and force at a sample rate equal to 8 times the forcing frequency. These discrete measurements were then used to calculate the magnitude of the force and velocity and the phase relationship of the velocity relative to the force as previously discussed. The procedure was repeated at nine different operating conditions consisting of three amplitudes at each of three different frequencies. Table 3.1 list the equipment settings for each of the nine sets of data.

Table 3.1 Equipment Settings

Test Number	Forcing Frequency Hz	Force Voltage (p-p) mV	Low-Pass Cut-off Hz	Pre/Post Gains (dB) Channel 0 (Force)	Channel 1 (Velocity)	High-Pass Cut-off Hz	Pre/Post Gains (dB) Channel 6 (Force)	Channel 7 (Velocity)
1	265.68	100	300	0/0	0/0	200	6/20	0/6
2	265.68	200	300	0/0	0/0	200	6/6	0/0
3	265.68	300	300	0/0	0/0	200	0/6	0/0
4	728.27	100	800	0/6	0/0	650	20/20	0/20
5	728.27	200	800	0/6	0/0	650	6/20	6/6
6	728.27	300	800	0/0	0/0	650	6/20	6/6
7	1418.4	50	1450	6/6	6/6	1350	6/20	6/20
8	1418.4	100	1450	6/6	6/6	1350	0/20	0/20
9	1418.4	150	1450	0/6	0/6	1350	0/20	0/20

3.4 Operating Conditions

The estimation of Poisson's ratio from anticlastic bending is based on the assumption that the beam responds purely in bending. The more closely this condition is met, the better the estimate of Poisson's ratio. In order to achieve this, careful selection of the forcing frequency is required.

The response of all dynamic systems can be represented by an infinite sum of modes. In the case of the free-free beam, there are non-bending modes excited which result in out-of-plane velocities, such as plate modes and torsion modes. In order to better meet the assumption, the excitation frequency should be selected such that the modal contribution of non-bending modes is reduced.

The first step in selecting the excitation frequency is to identify the bending modes. A driving point FRF using burst random excitation is an efficient method for doing this. This FRF was performed using a Tektronix 2630 Fourier Analyzer, electromechanical shaker, force transducer, and accelerometer. The resulting driving point force-to-acceleration FRF taken at the center of the top edge of the beam is shown in Fig. 3.11.

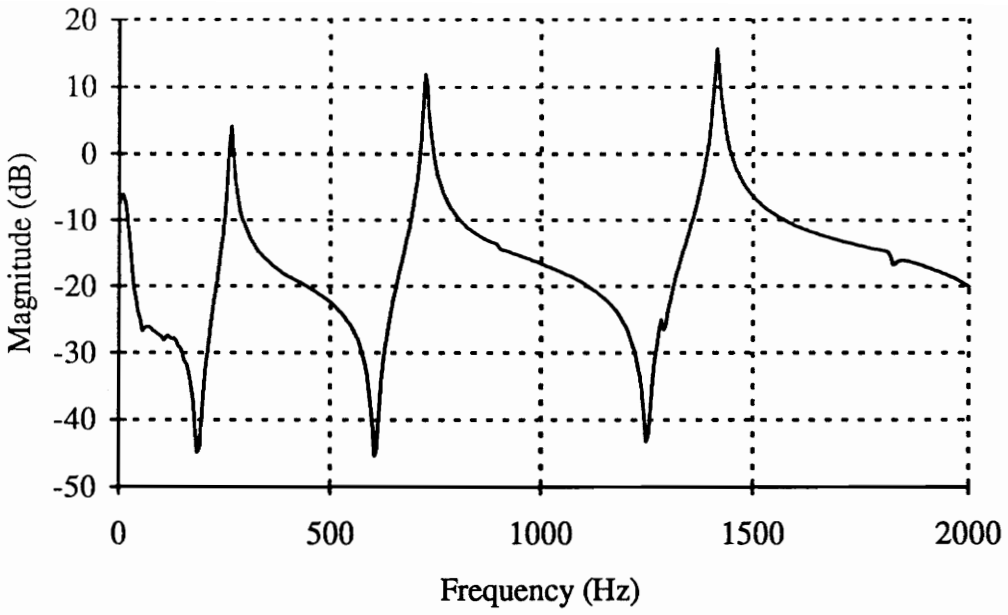

Figure 3.11 FRF Magnitude for Driving Point Test

From the FRF the approximate resonant frequencies for the first three bending modes were identified as 250 Hz, 725 Hz, and 1400 Hz. More exact resonant frequencies were found through the use of a Lissajou plot using the experimental setup for the velocity profile measurement. The laser velocimeter was aimed at a corner of the beam and the velocity signal was plotted on the horizontal axis of the oscilloscope. The output of the force transducer was plotted on the vertical axis of the oscilloscope. At resonance, the force and voltage exhibit a phase relationship of either 0° or 180°. This condition produces a Lissajou plot consisting of a single line with a slope of either ±1. The frequency of the signal generator was adjusted until this condition was met. The resonant frequencies based on this method were found to be 265.68 Hz, 728.27 Hz, and 1418.4 Hz.

3.5 Data Post-Processing

Following collection of data, the files created by MDI10, were converted into Matlab format. The Matlab files were then converted from MacIntosh format to IBM PC format. All subsequent data processing was performed using Matlab for Windows.

As stated in Chapter 2, the relationship between the measured voltage, v_m, and the true structure velocity, V_S, is

$$V_S(x,y) = K\frac{v_m}{\cos(\theta_x)\cos(\theta_y)} \tag{3.26}$$

The first step in the data processing was to convert the measured voltages and variances to displacements according to

$$D_s(x,y) = \frac{1}{\omega_o}\cdot K\cdot\frac{v_m}{\cos(\theta_x)\cos(\theta_y)} \tag{3.27}$$

where K is the sensitivity of the velocimeter which is equal to .0333 (m/s)/Volt.

Although it was possible to apply this conversion prior to applying the least squares method, only the last term of the conversion was applied. This was done to keep the relative size of the regressors and observation close to one. This reduces the chances of numerical inaccuracies due to round-off error. Therefore the model was fit to the voltages corresponding to the true structure velocities.

Once the proper model was found, the remainder of the conversion factor was applied to convert to displacement. This model was then differentiated twice in the x and y directions as previously stated and local estimates and variances of Poisson's ratio were found at the x and y locations of the original measurements. Weighted least squares was then applied to the local estimates and variances to arrive at a single global value and variance of Poisson's ratio.

3.6 Summary

This chapter described the experimental procedure used to obtain the information necessary to perform the processing described in Chapter 2. From the measured velocity profile, it was possible to arrive at the displacement data which could be used to find a continuous model. This continuous model can now be evaluated and used to find local and global estimates of Poisson's ratio. The results of the processing is discussed in the next chapter.

Chapter 4

Results

4.1 Introduction

Up to this point, the method for estimating Poisson's ratio has been presented. The results of the estimation procedure are presented in this chapter. Recalling the goals of this work, it is now necessary to evaluate the estimates and uncertainties of Poisson's ratio to determine if Poisson's ratio is dependent on the frequency and amplitude of excitation. Furthermore, it is important to determine if the difference in the estimates of Poisson's ratio for the different excitations can be attributed to changes in Poisson's ratio, to violations of the assumptions, or to experimental error.

The first section consists of the estimates of Poisson's ratio for each of the excitation conditions. A discussion of the results follows as does possible reasons for the differences in the estimates.

4.2 Results

Having processed the data according to the procedures outlined in Chapters 2 and 3, the resulting sample means and sample standard deviations for the local estimates of Poisson's ratio shown in Figs. 4.1 through 4.27. Included in these figures are plots of the local estimates with the values outside the range of $0<\upsilon<.5$ removed in order to increase the resolution.

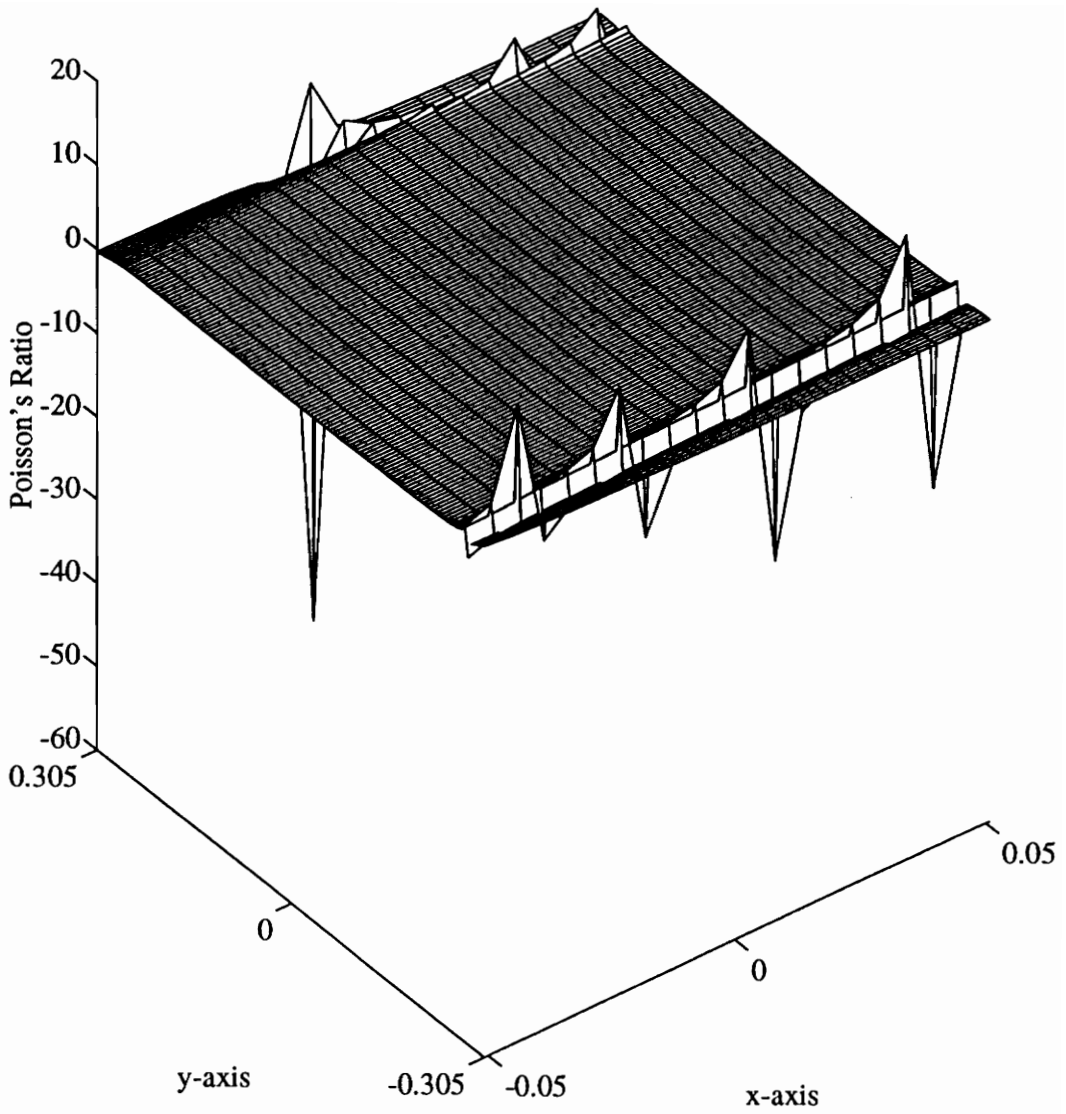

Figure 4.1 Poisson's Ratio 265.7 Hz, Reference Force

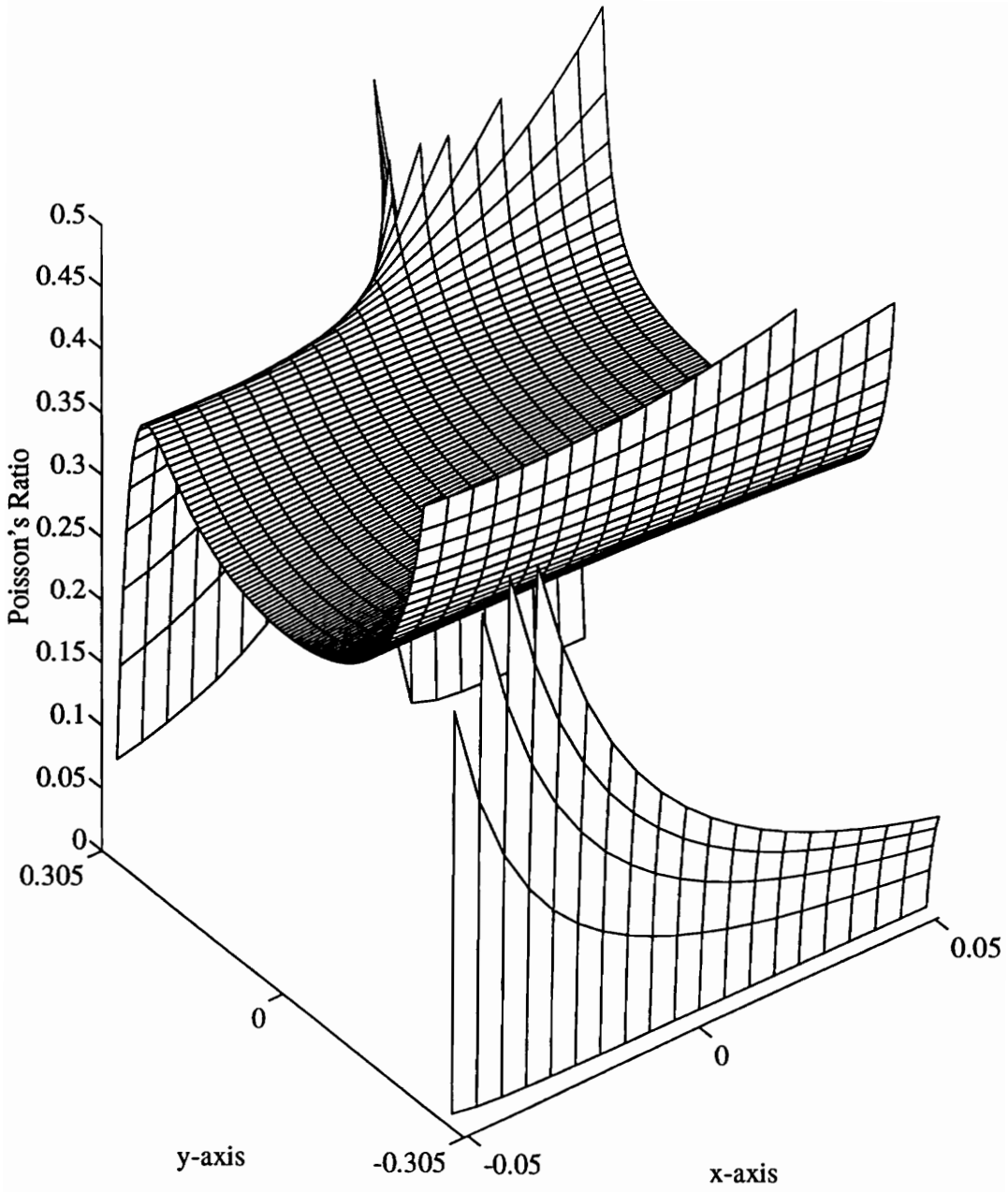

Figure 4.2 Poisson's Ratio 265.7 Hz, Reference Force, Peaks Removed

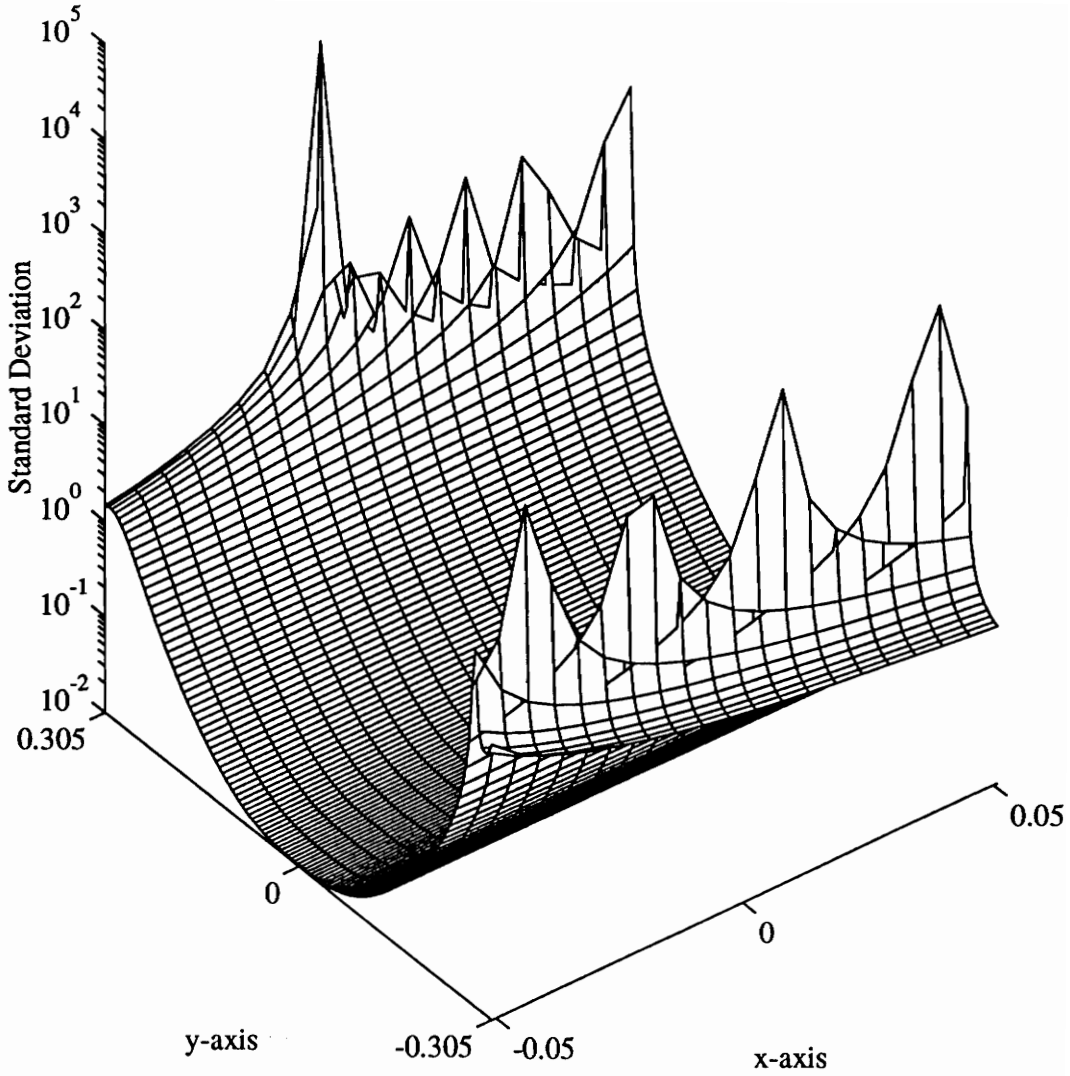

Figure 4.3 Standard Deviation of Poisson's Ratio 265.7 Hz, Reference Force

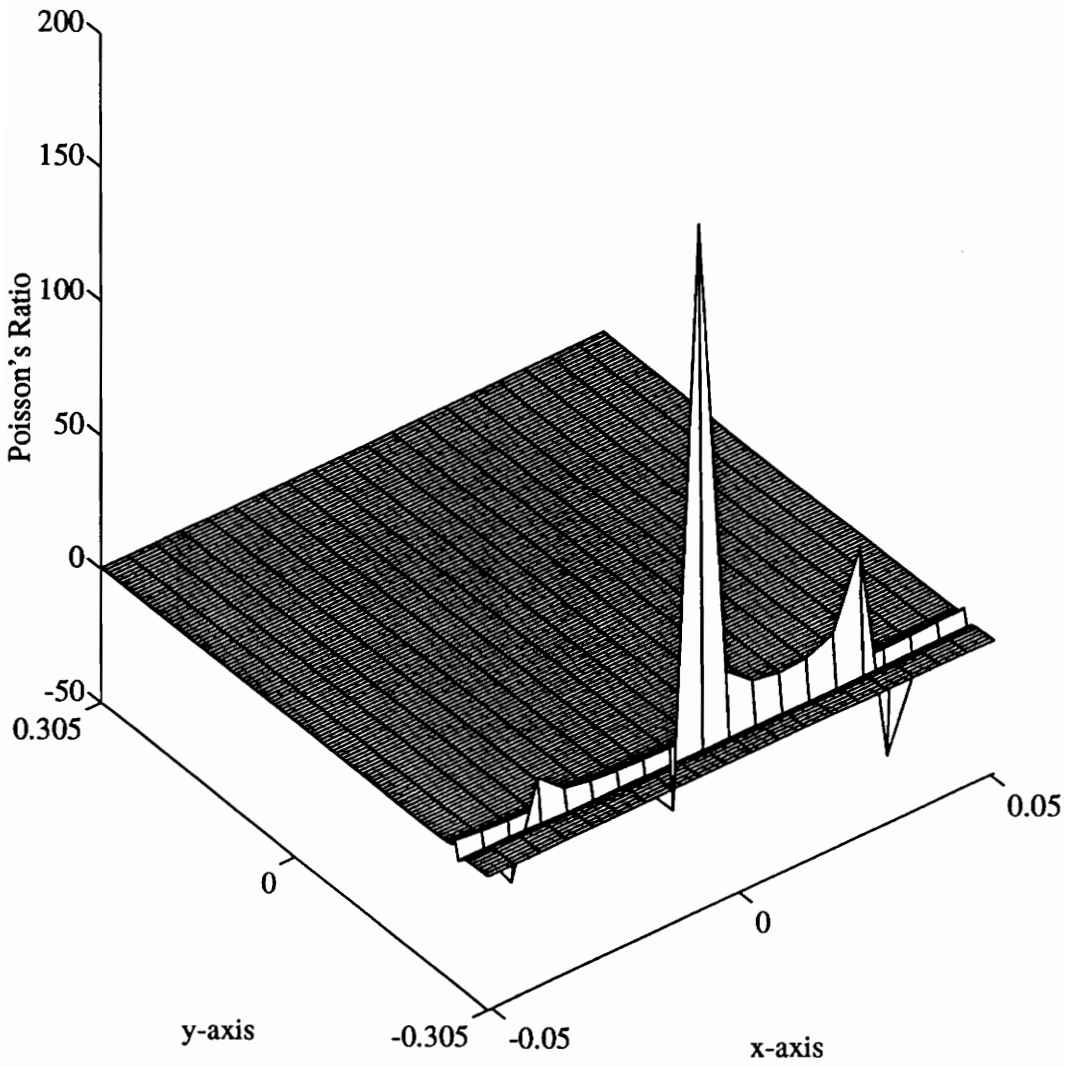

Figure 4.4 Poisson's Ratio 265.7 Hz, 2*Reference Force

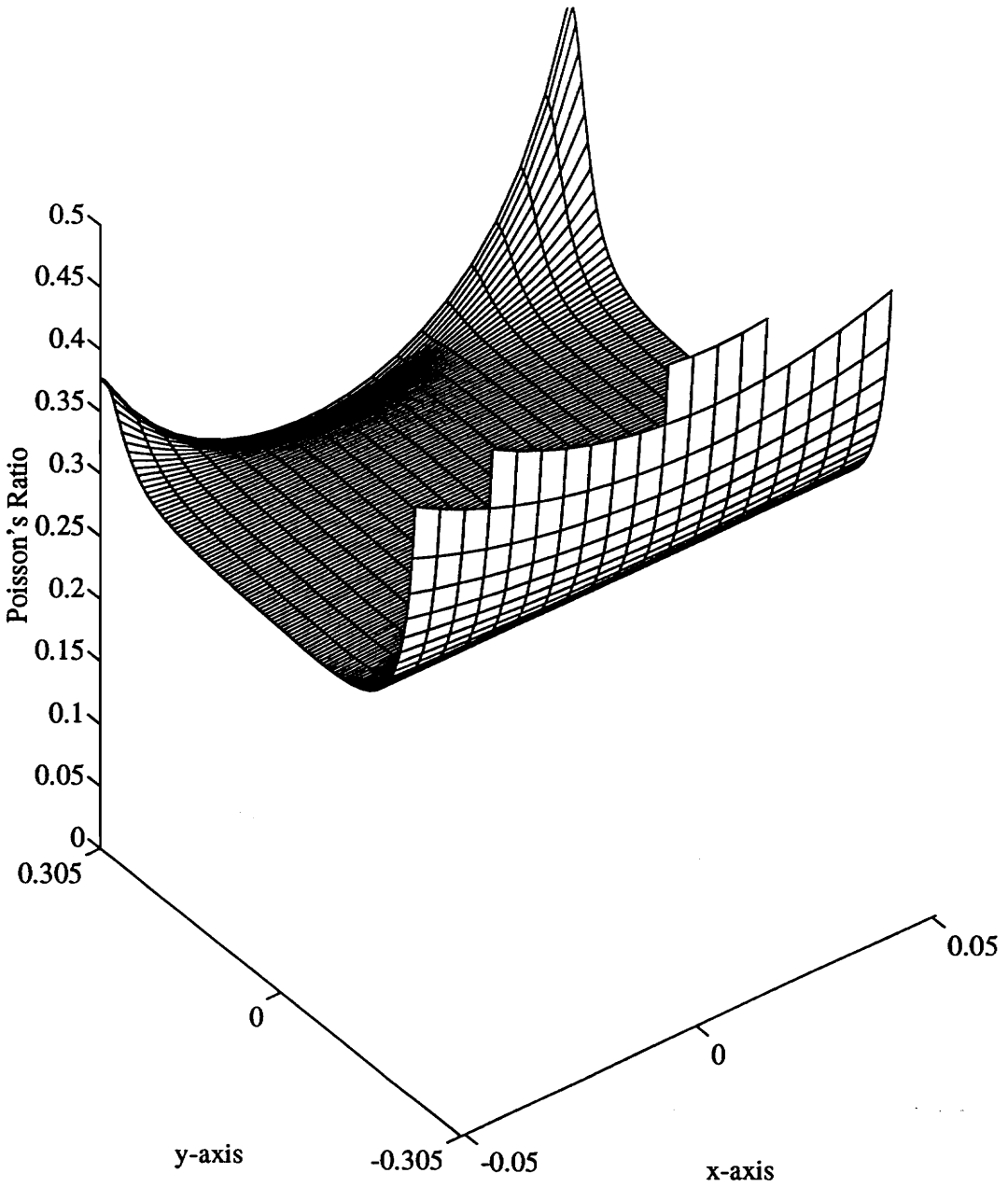

Figure 4.5 Poisson's Ratio 265.7 Hz, 2*Reference Force, Peaks Removed

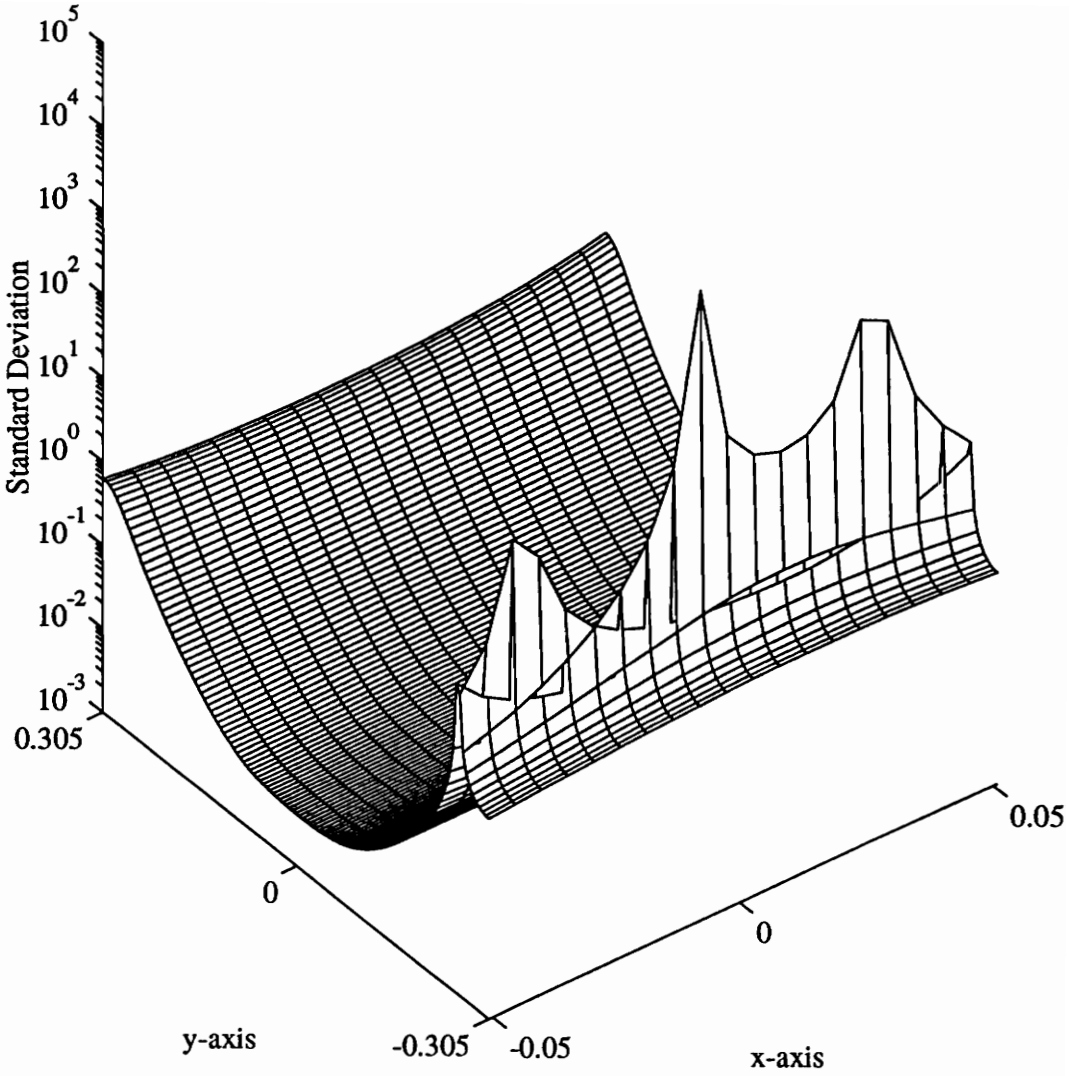

Figure 4.6 Standard Deviation of Poisson's Ratio 265.7 Hz, 2*Reference Force

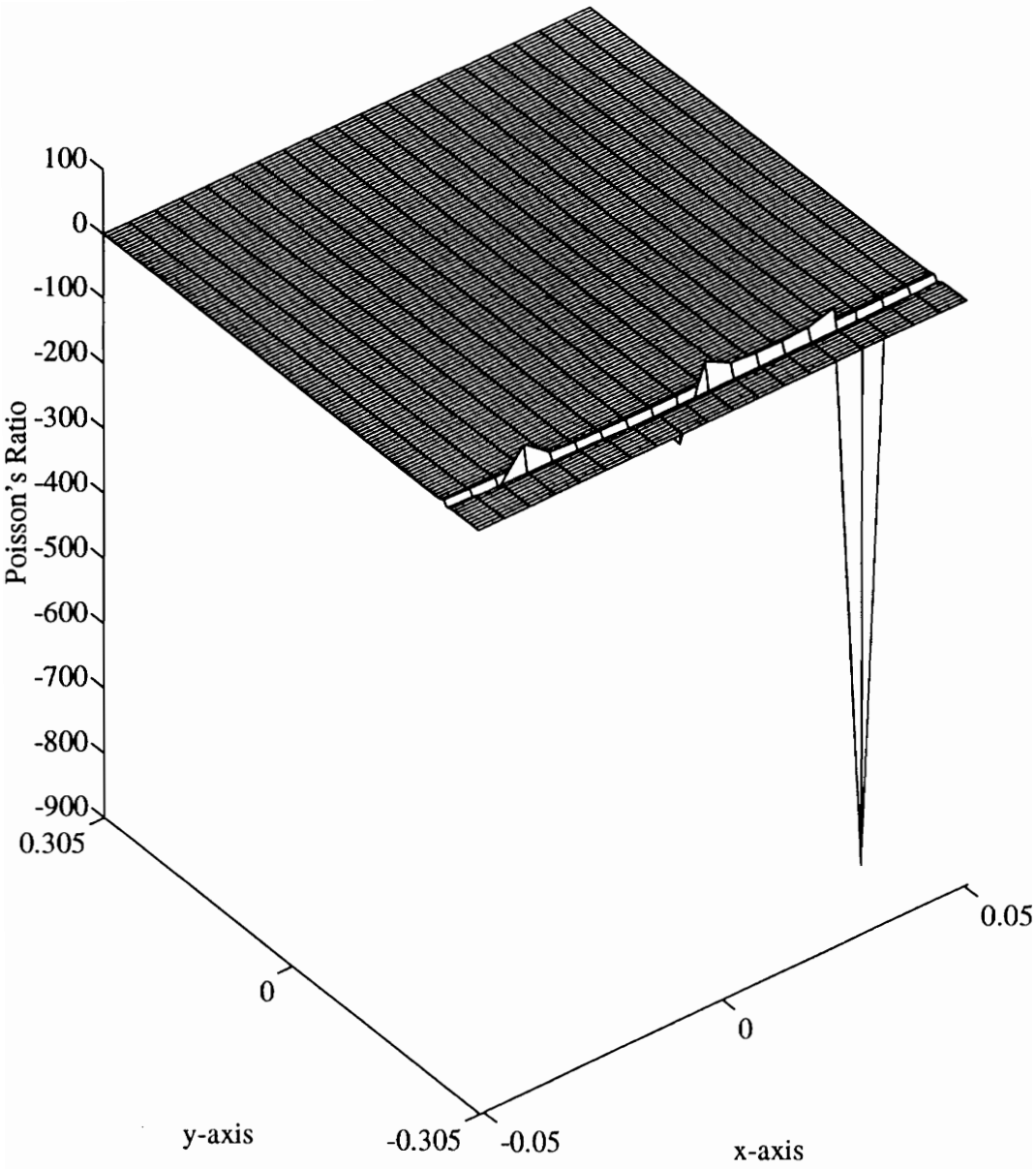

Figure 4.7 Poisson's Ratio 265.7 Hz, 3*Reference Force

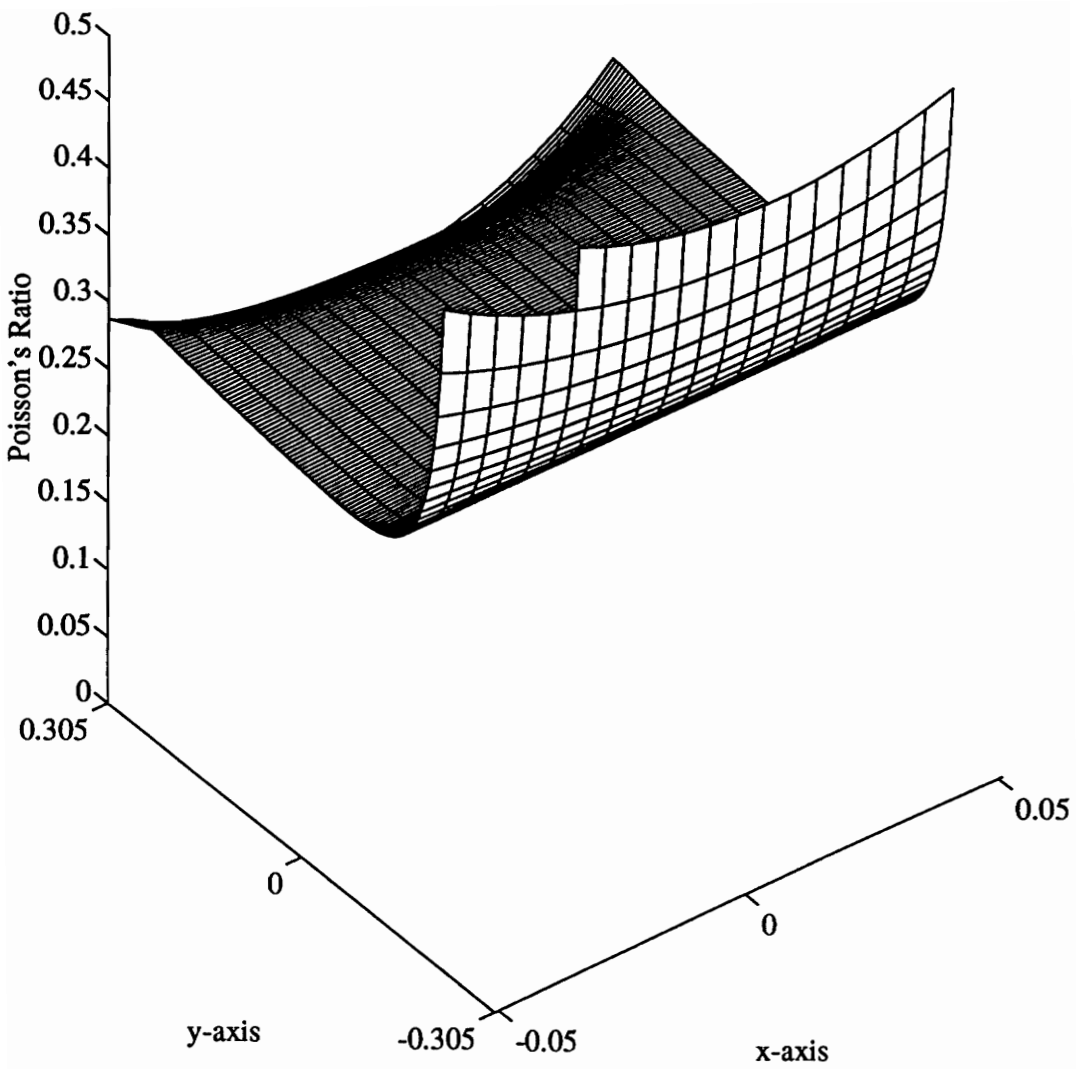

Figure 4.8 Poisson's Ratio 265.7 Hz, 3*Reference Force, Peaks Removed

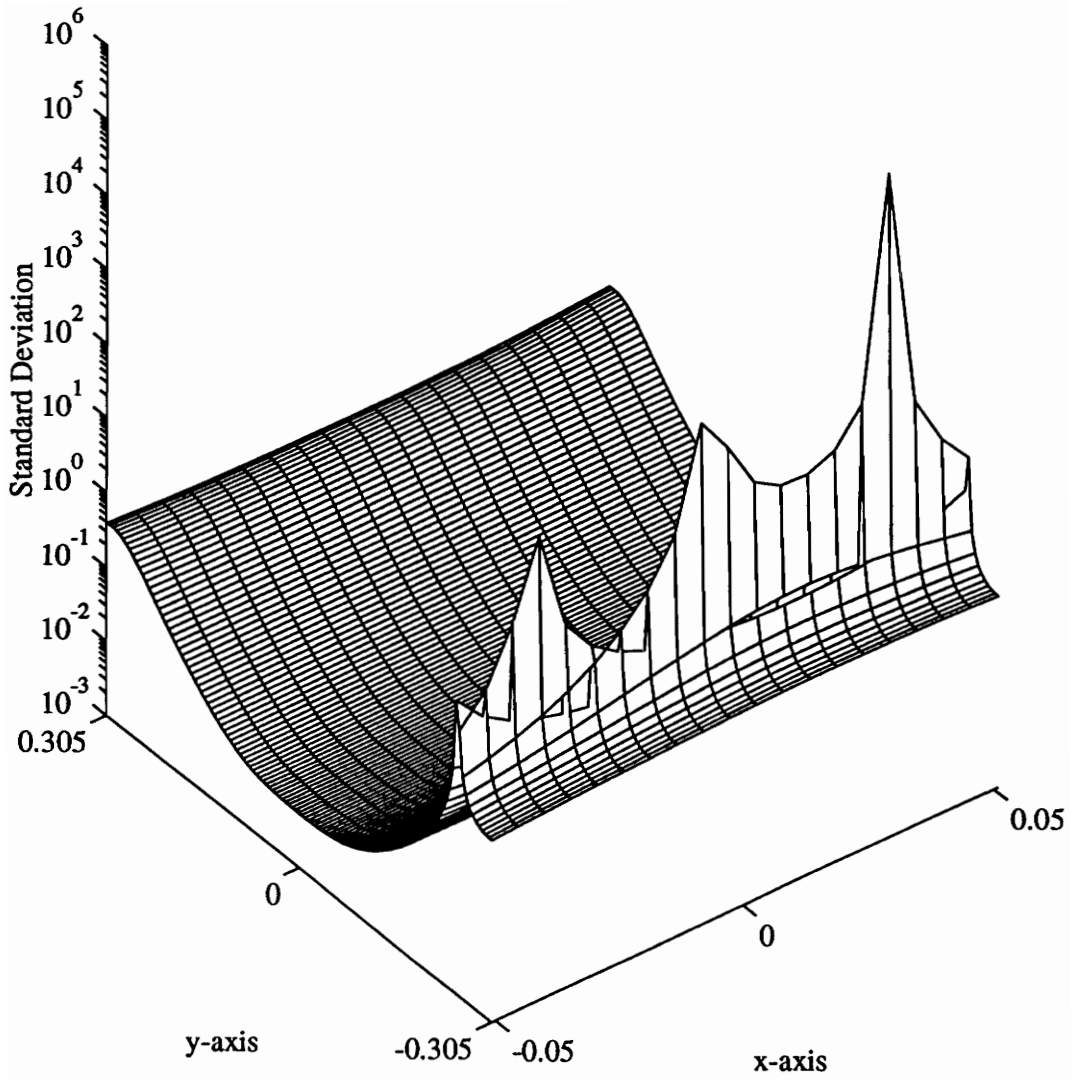

Figure 4.9 Standard Deviation of Poisson's Ratio 265.7 Hz, 3*Reference Force

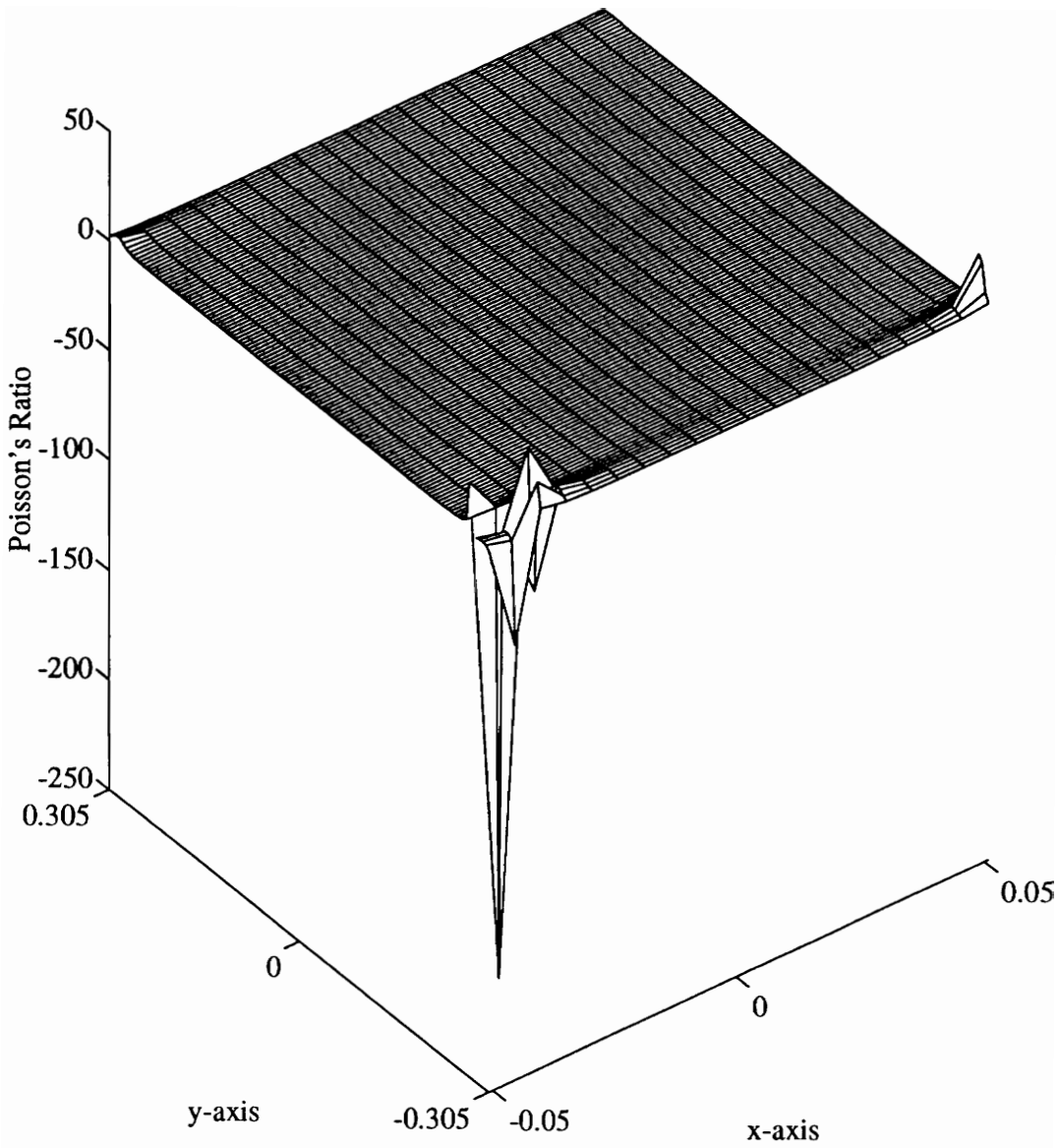

Figure 4.10 Poisson's Ratio 728.3 Hz, Reference Force

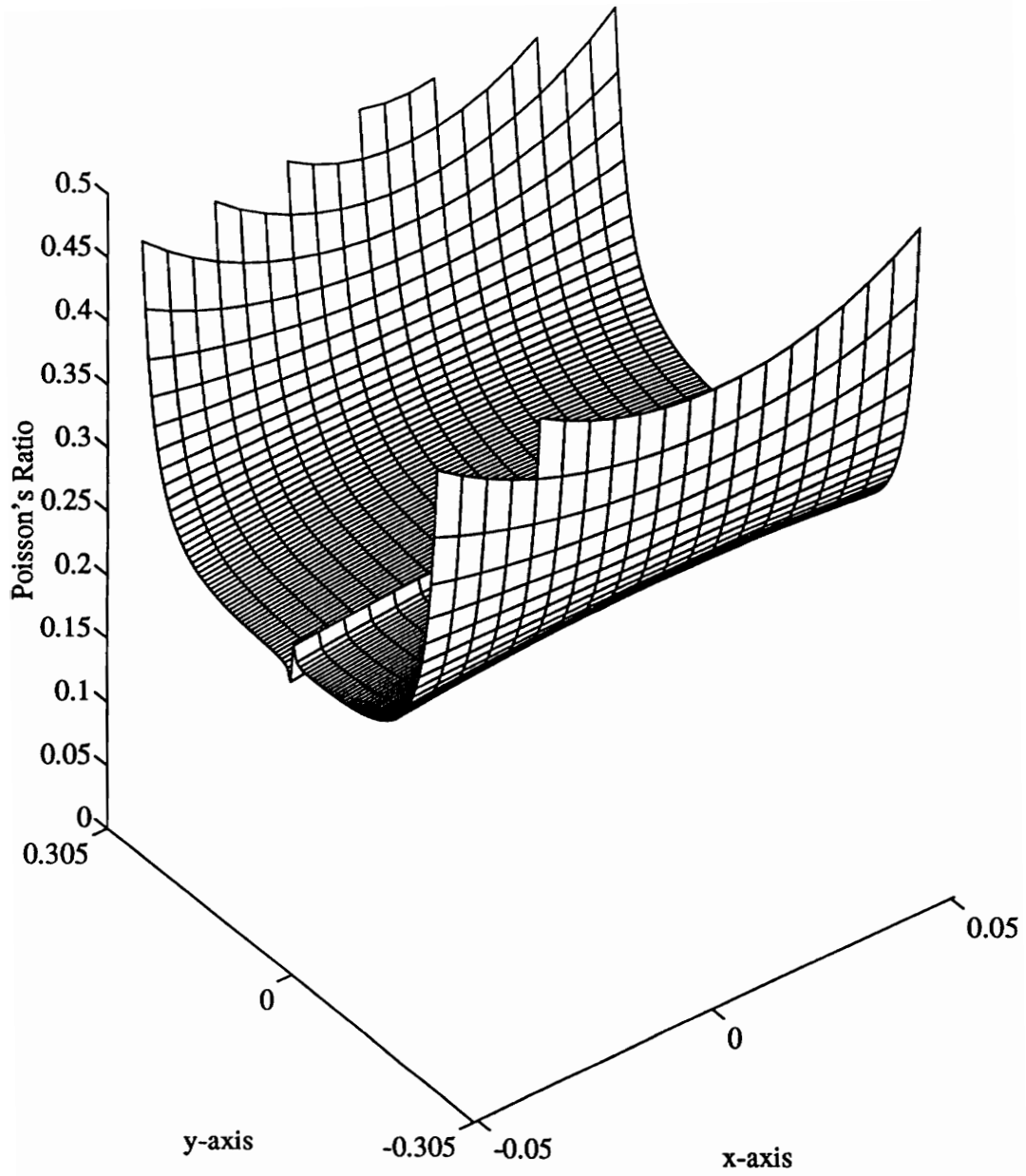

Figure 4.11 Poisson's Ratio 728.3 Hz, Reference Force, Peaks Removed

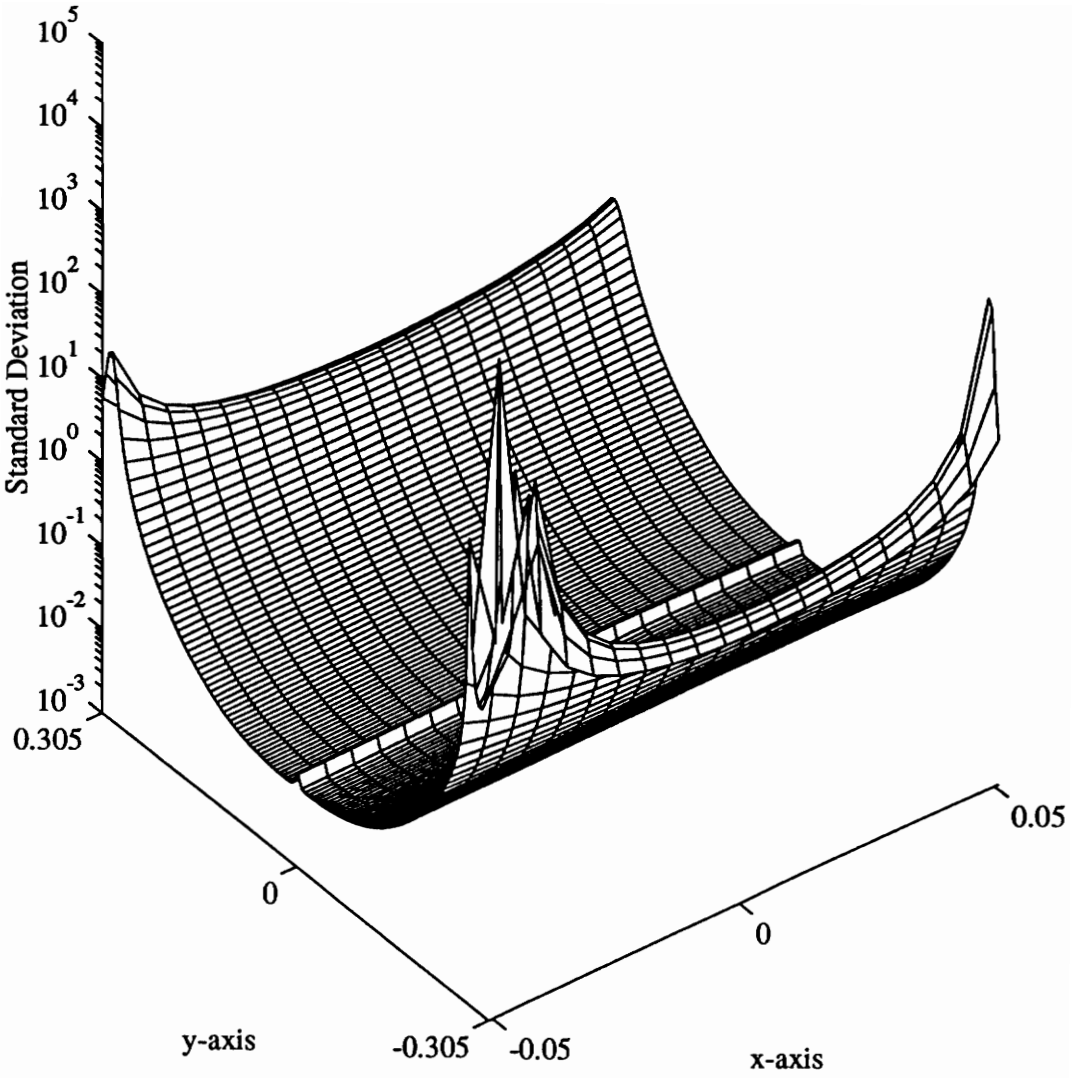

Figure 4.12 Standard Deviation of Poisson's Ratio 728.3 Hz, Reference Force

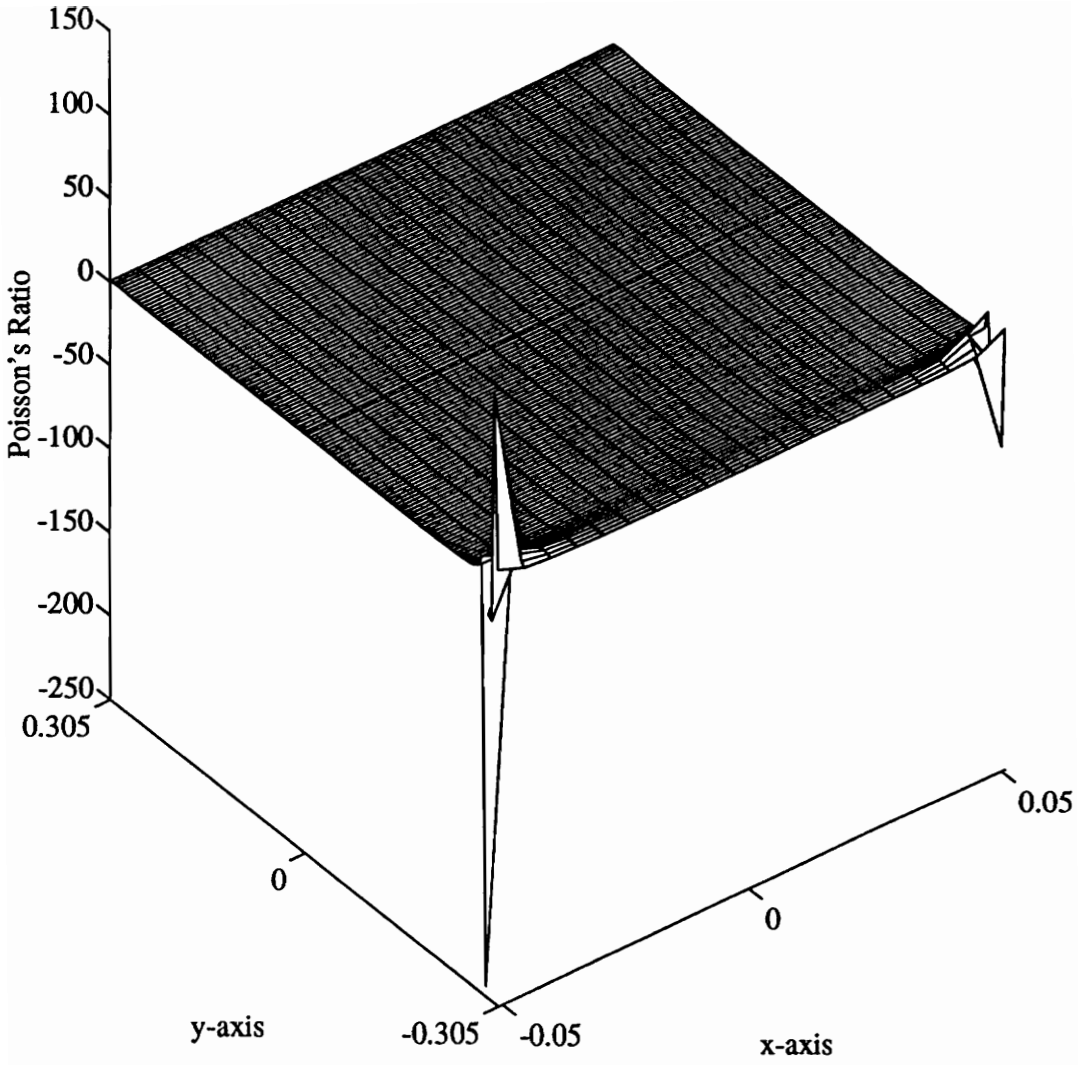

Figure 4.13 Poisson's Ratio 728.3 Hz, 2*Reference Force

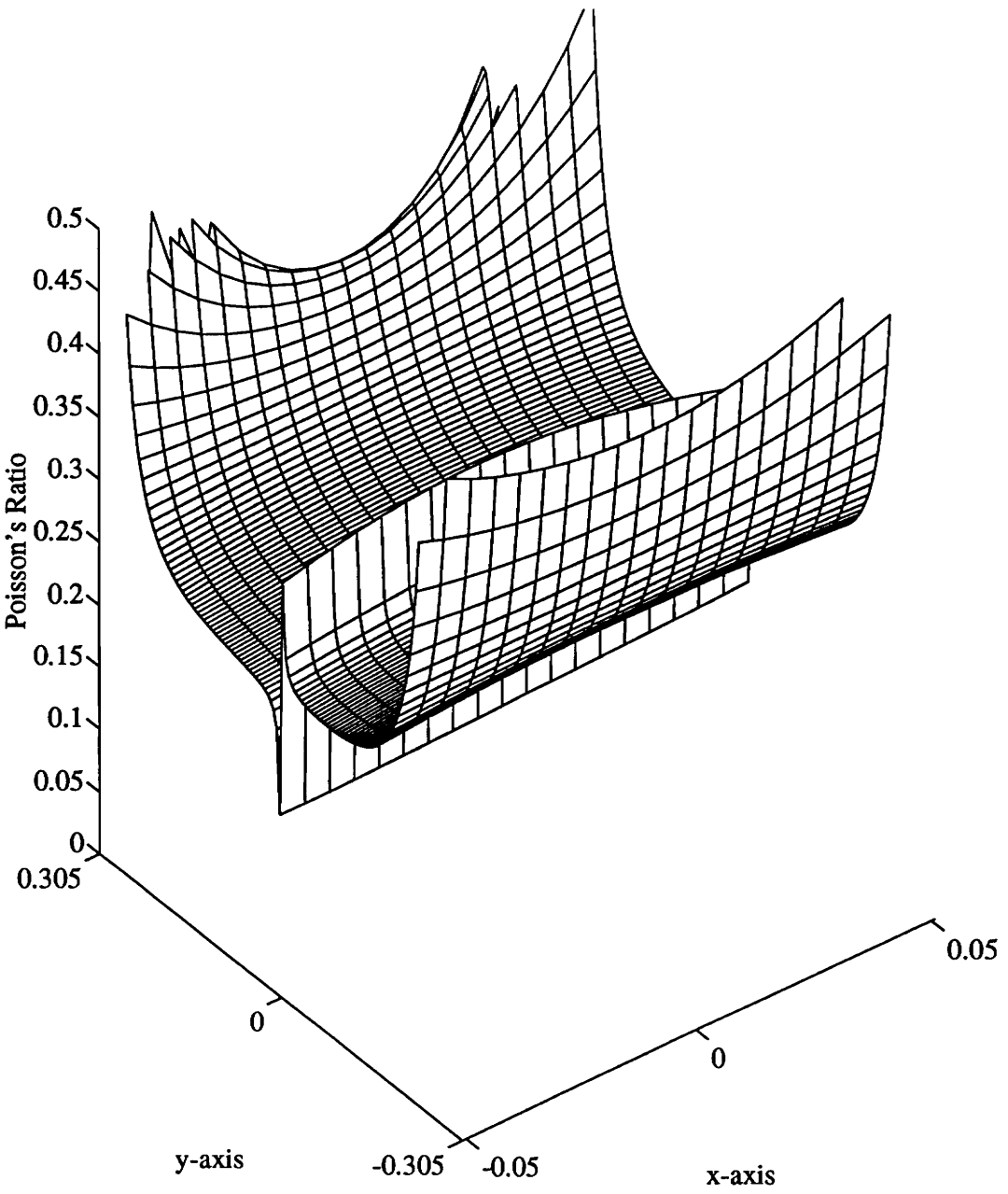

Figure 4.14 Poisson's Ratio 728.3 Hz, 2*Reference Force, Peaks Removed

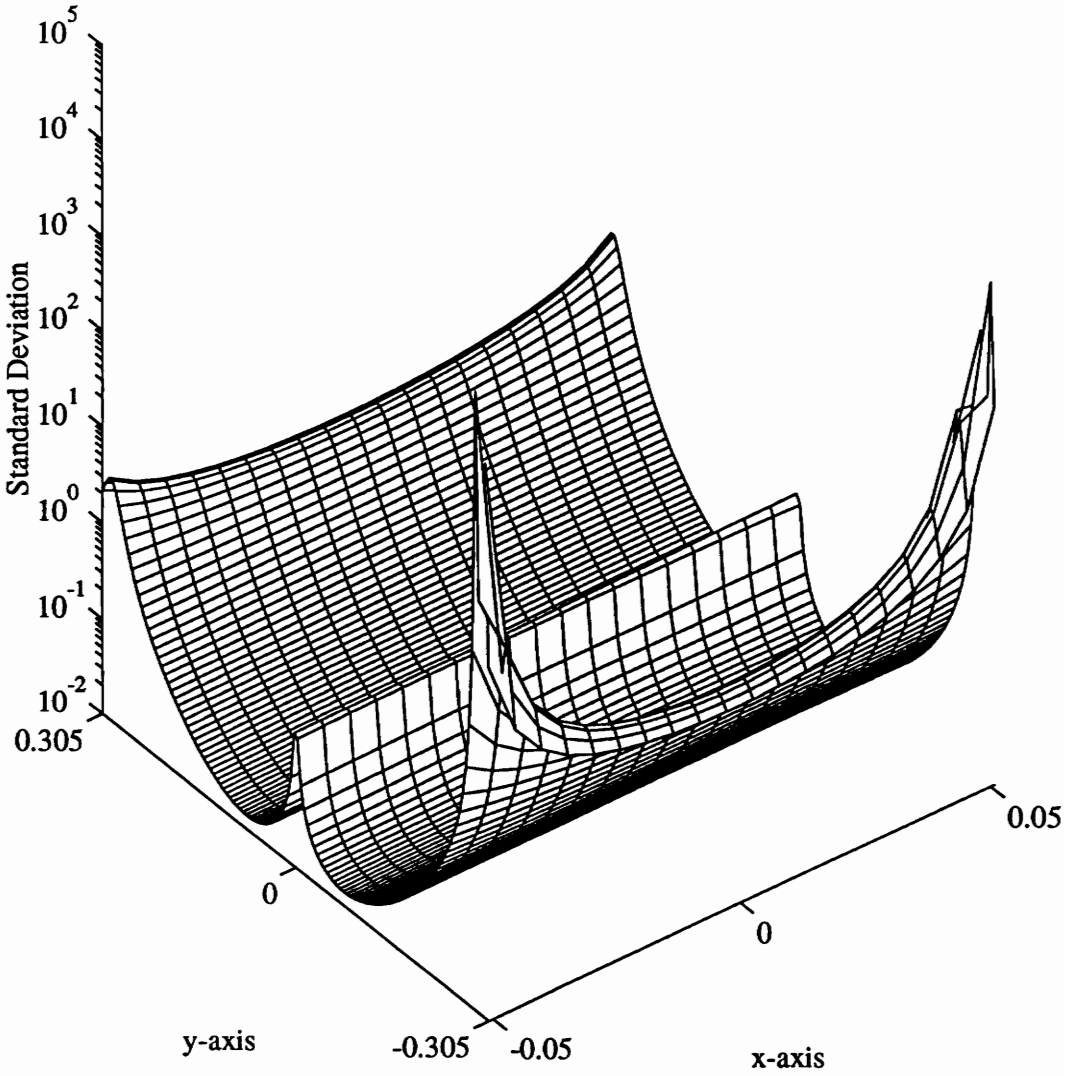

Figure 4.15 Standard Deviation of Poisson's Ratio 728.3 Hz, 2*Reference Force

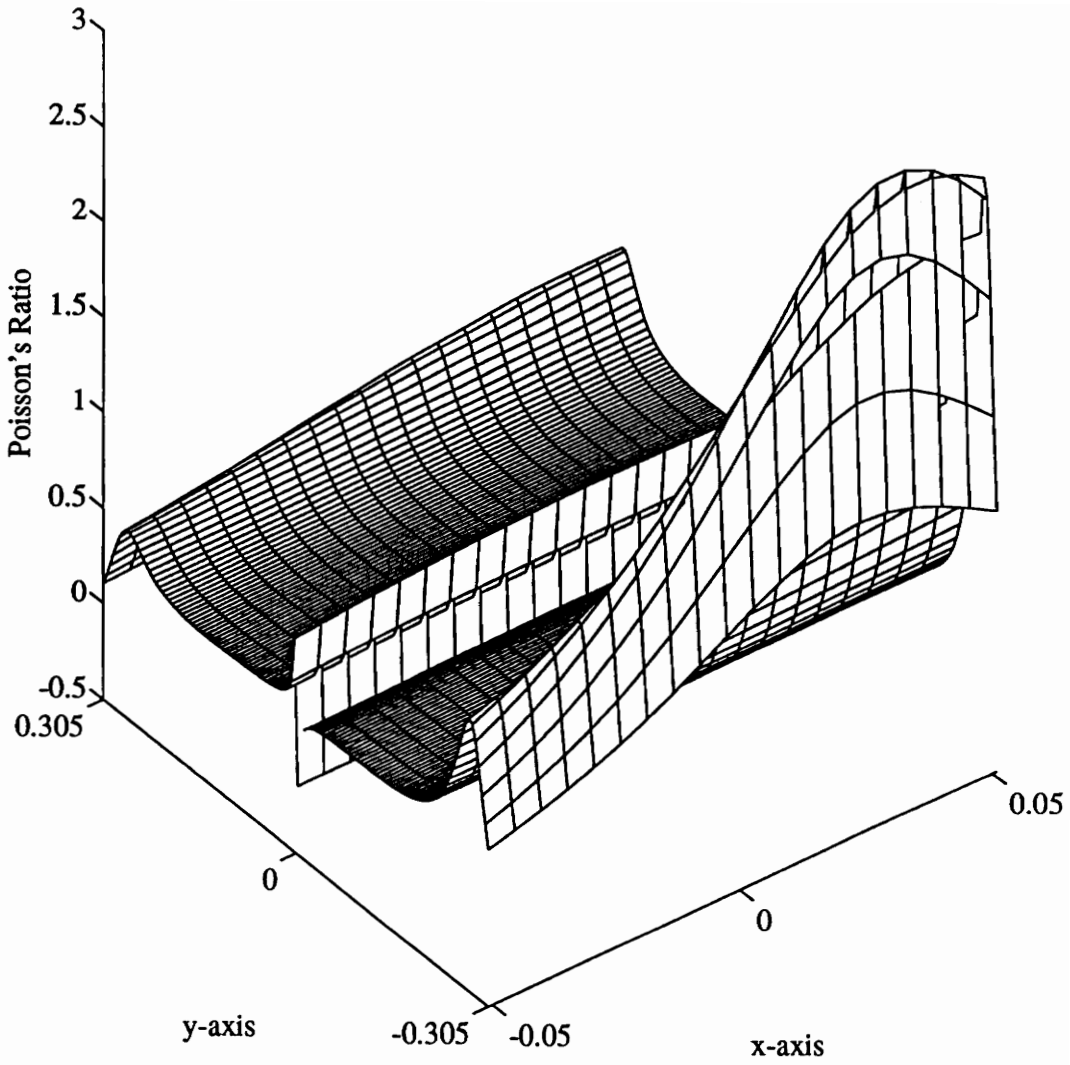

Figure 4.16 Poisson's Ratio 728.3 Hz, 3*Reference Force

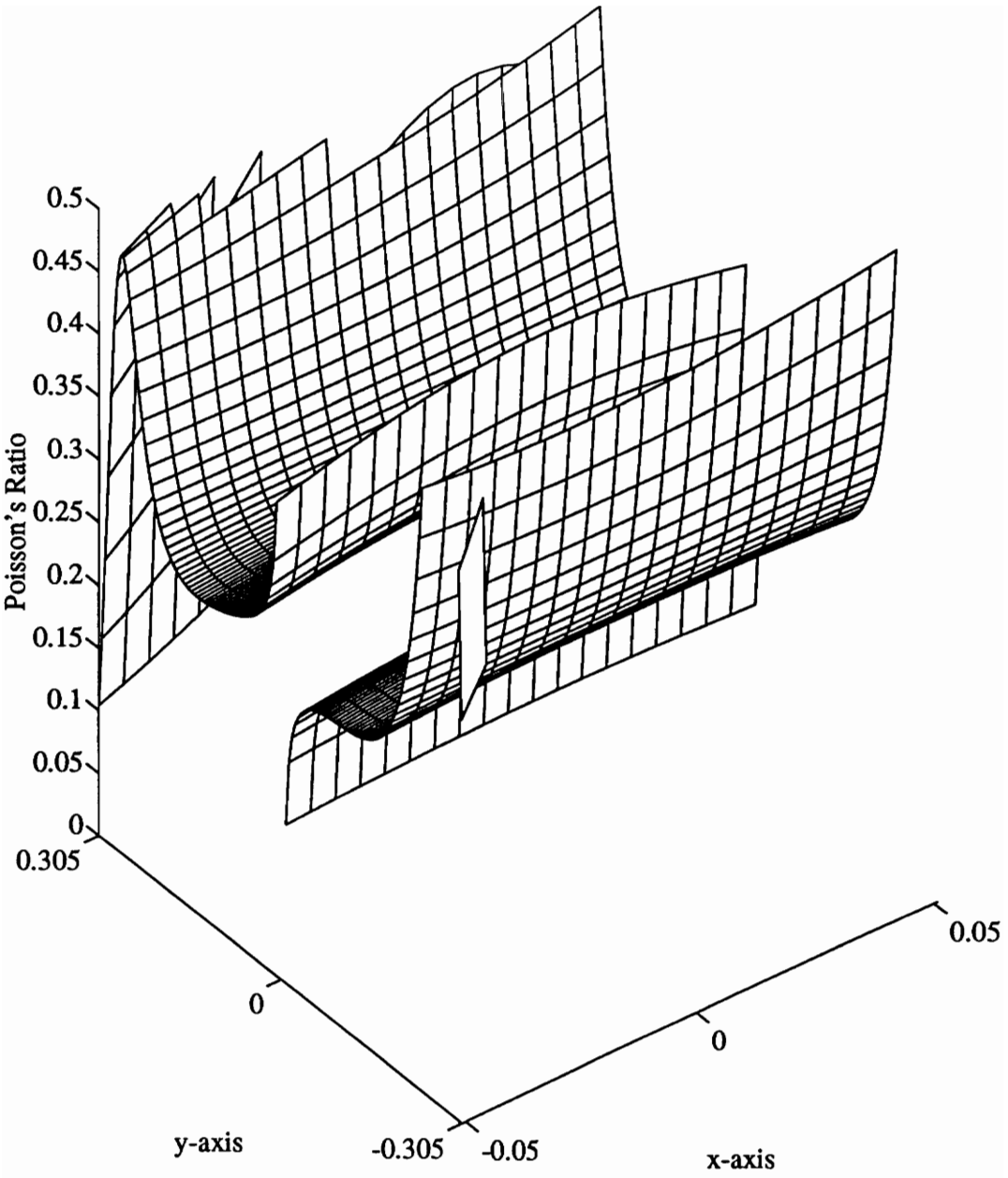

Figure 4.17 Poisson's Ratio 728.3 Hz, 3*Reference Force

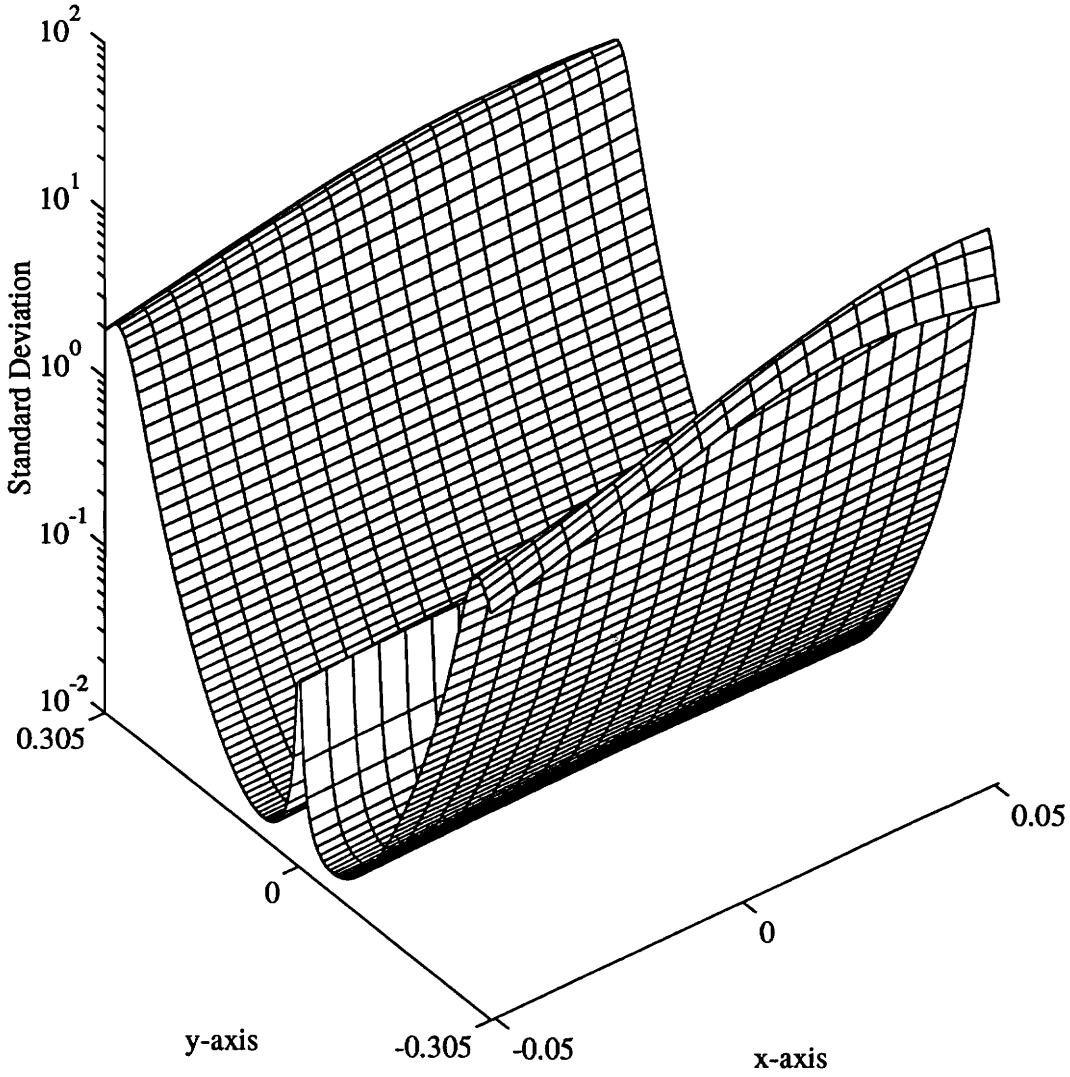

Figure 4.18 Standard Deviation of Poisson's Ratio 728.3 Hz, 3*Reference Force

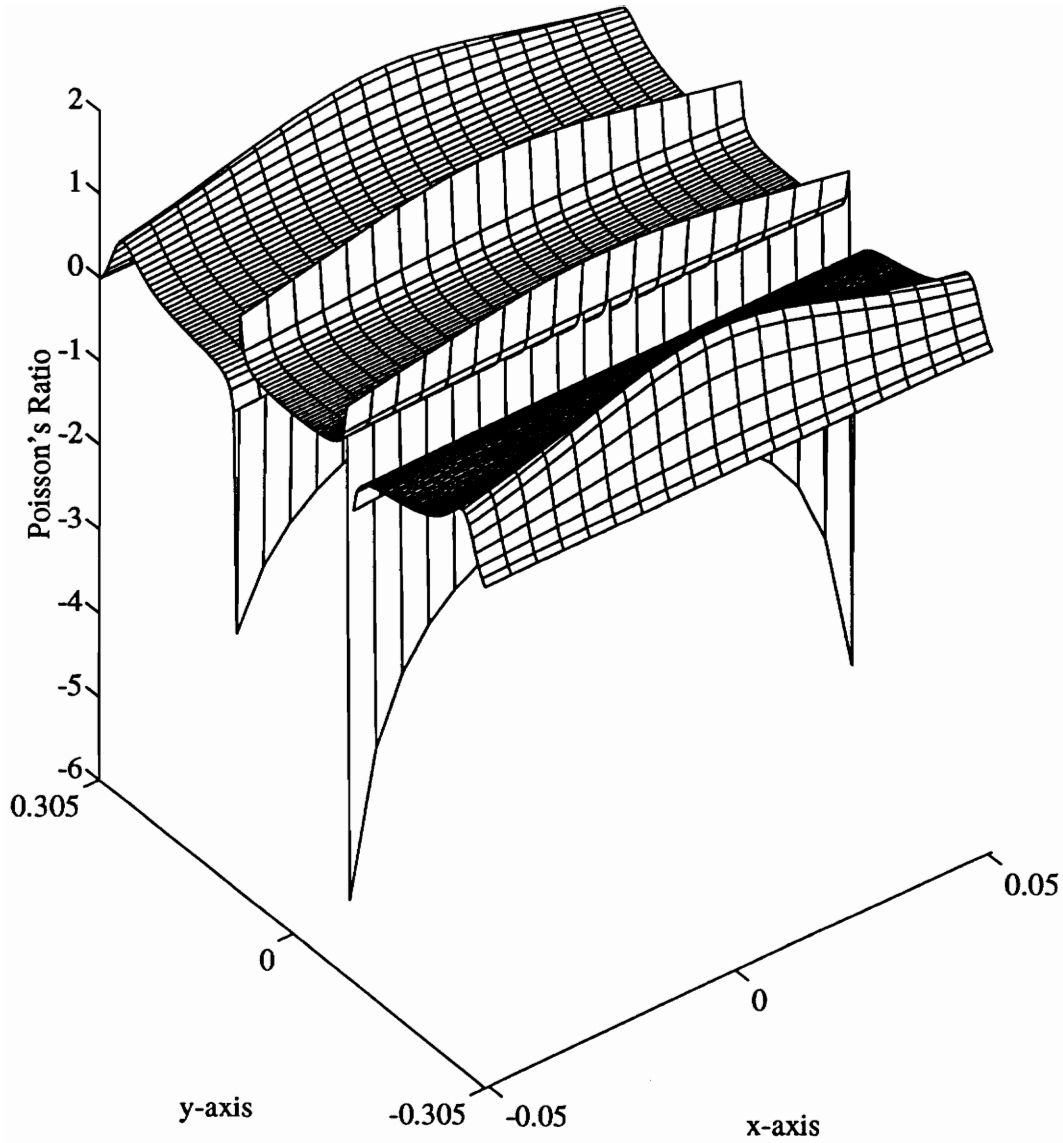

Figure 4.19 Poisson's Ratio 1418 Hz, Reference Force

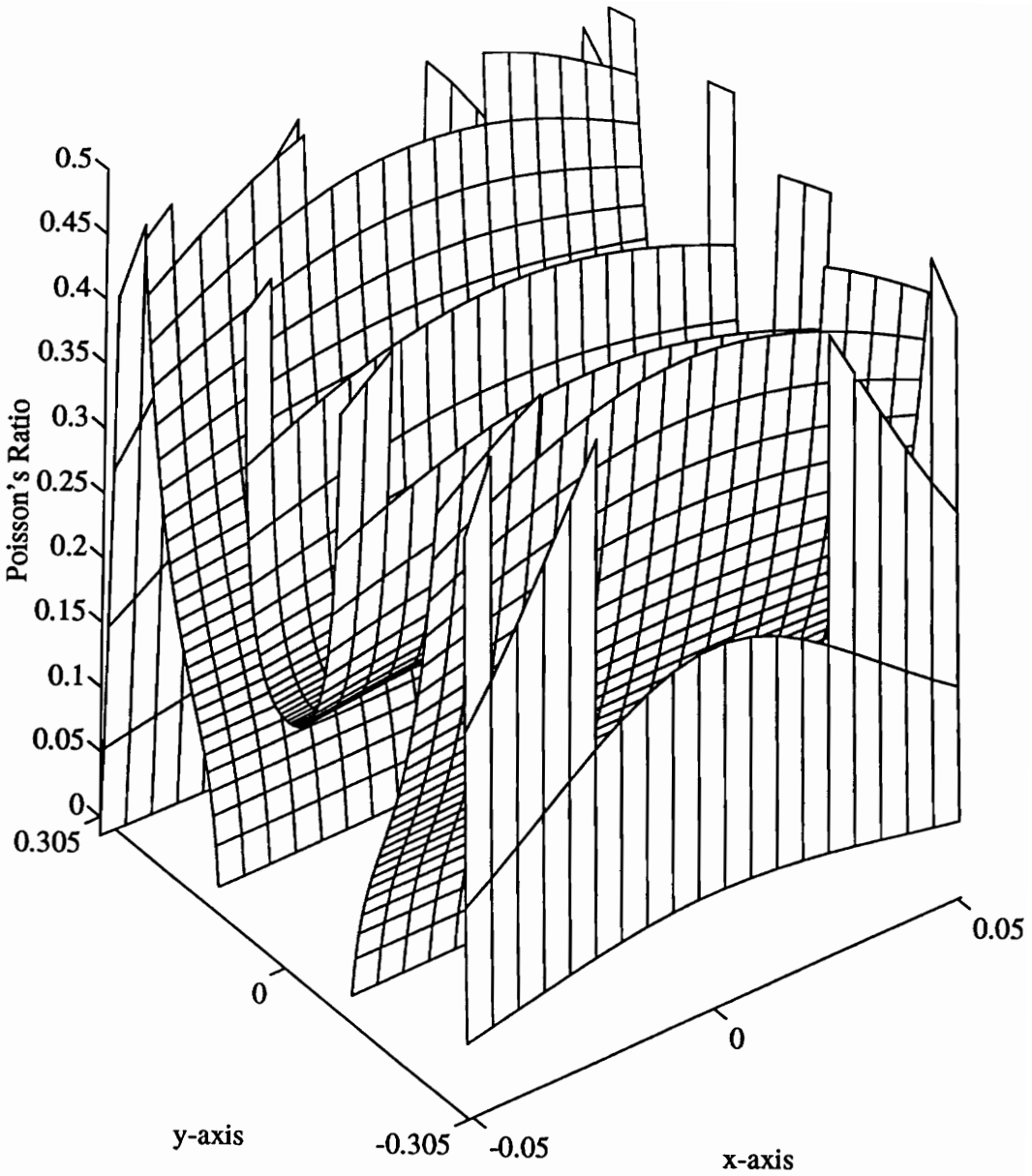

Figure 4.20 Poisson's Ratio 1418 Hz, Reference Force, Peaks Removed

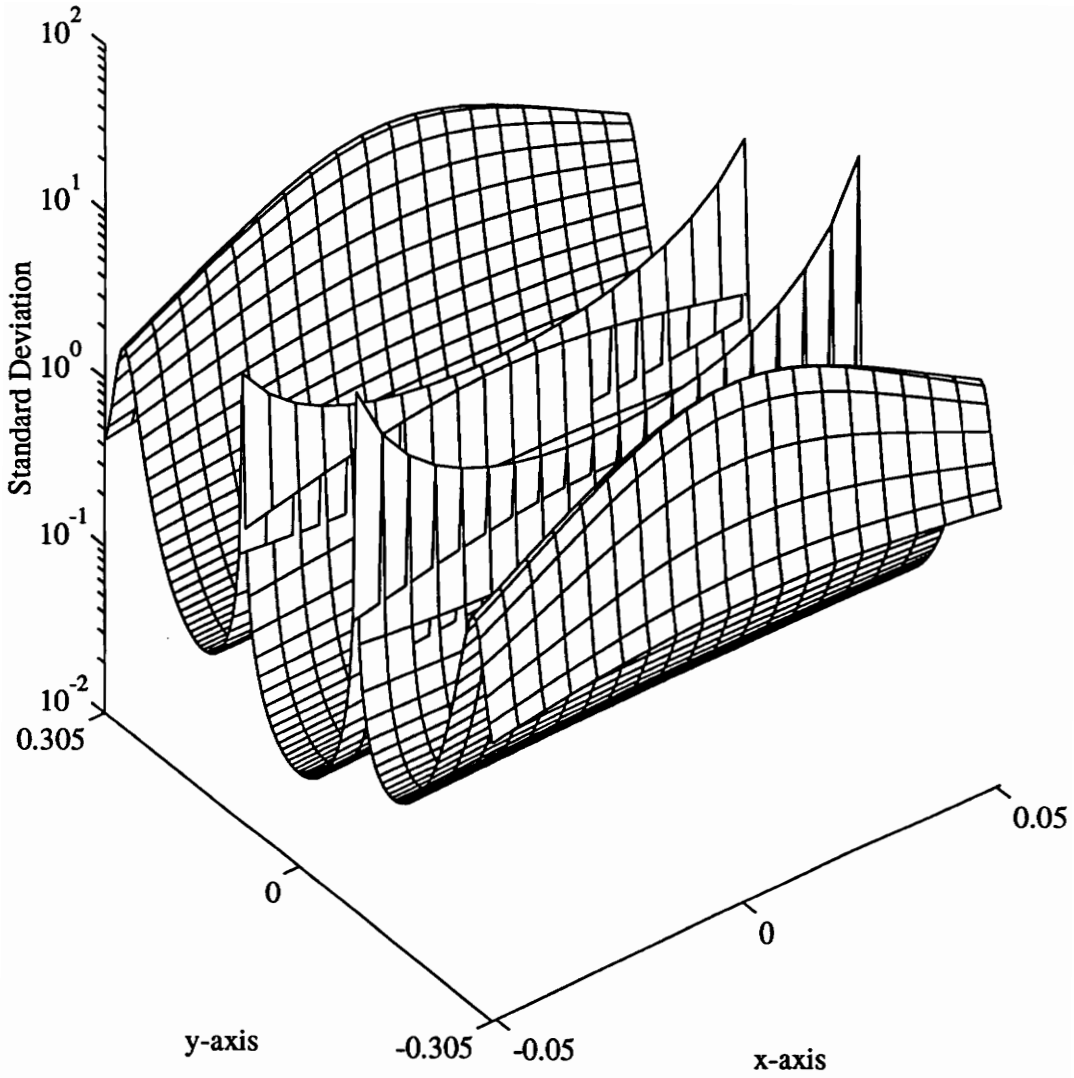

Figure 4.21 Standard Deviation of Poisson's Ratio 1418 Hz, Reference Force

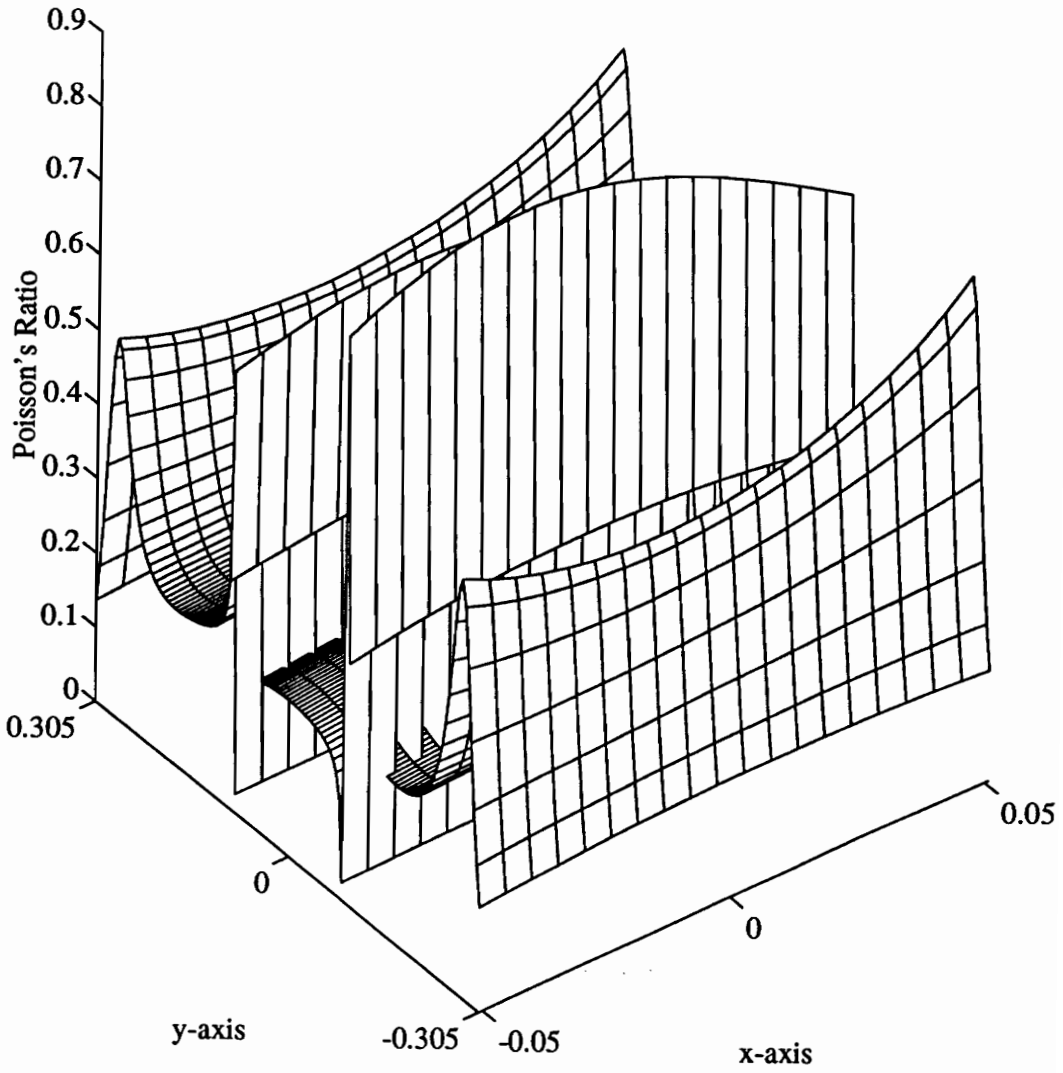

Figure 4.22 Poisson's Ratio 1418 Hz, 2*Reference Force

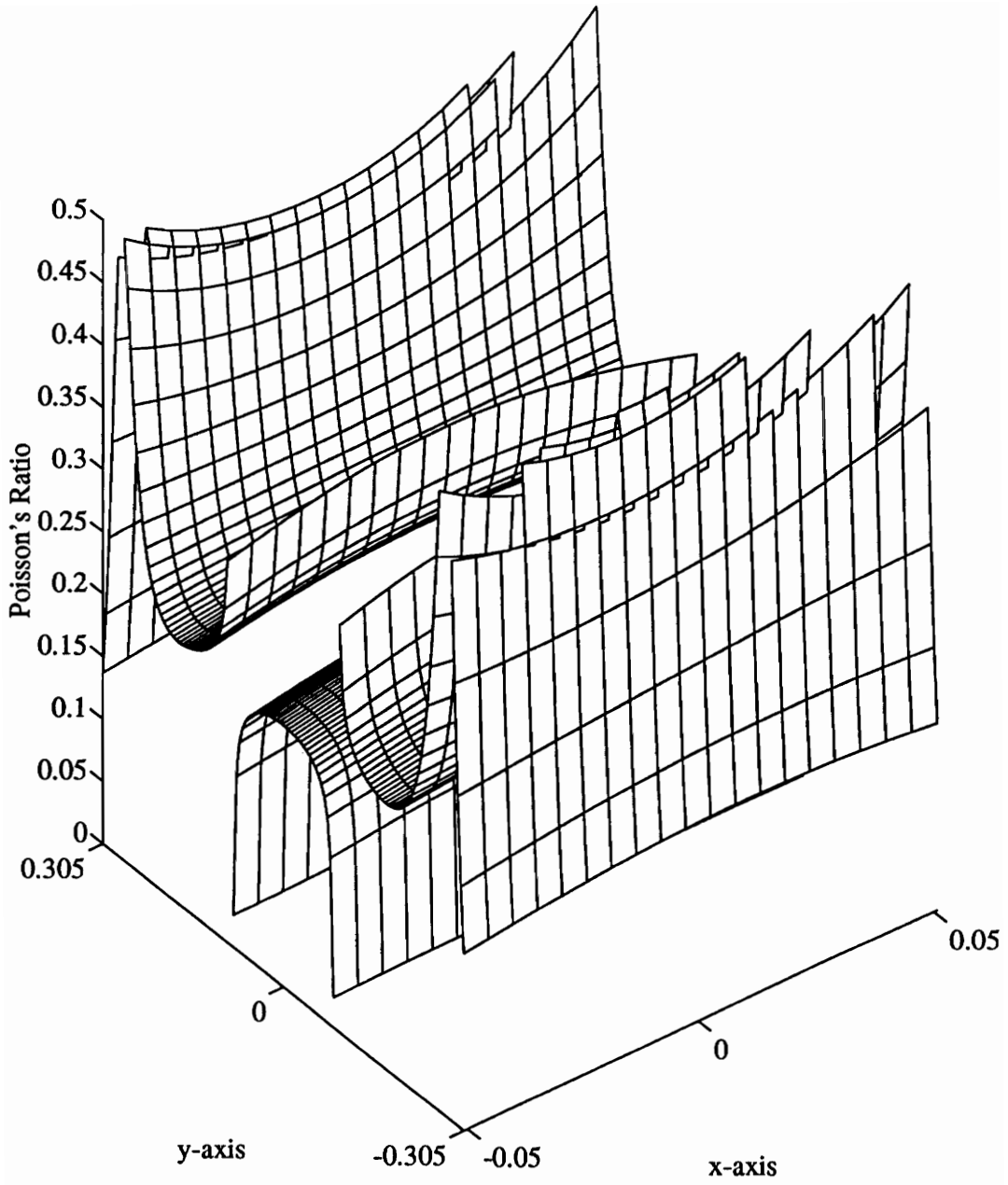

Figure 4.23 Poisson's Ratio 1418 Hz, 2*Reference Force, Peaks Removed

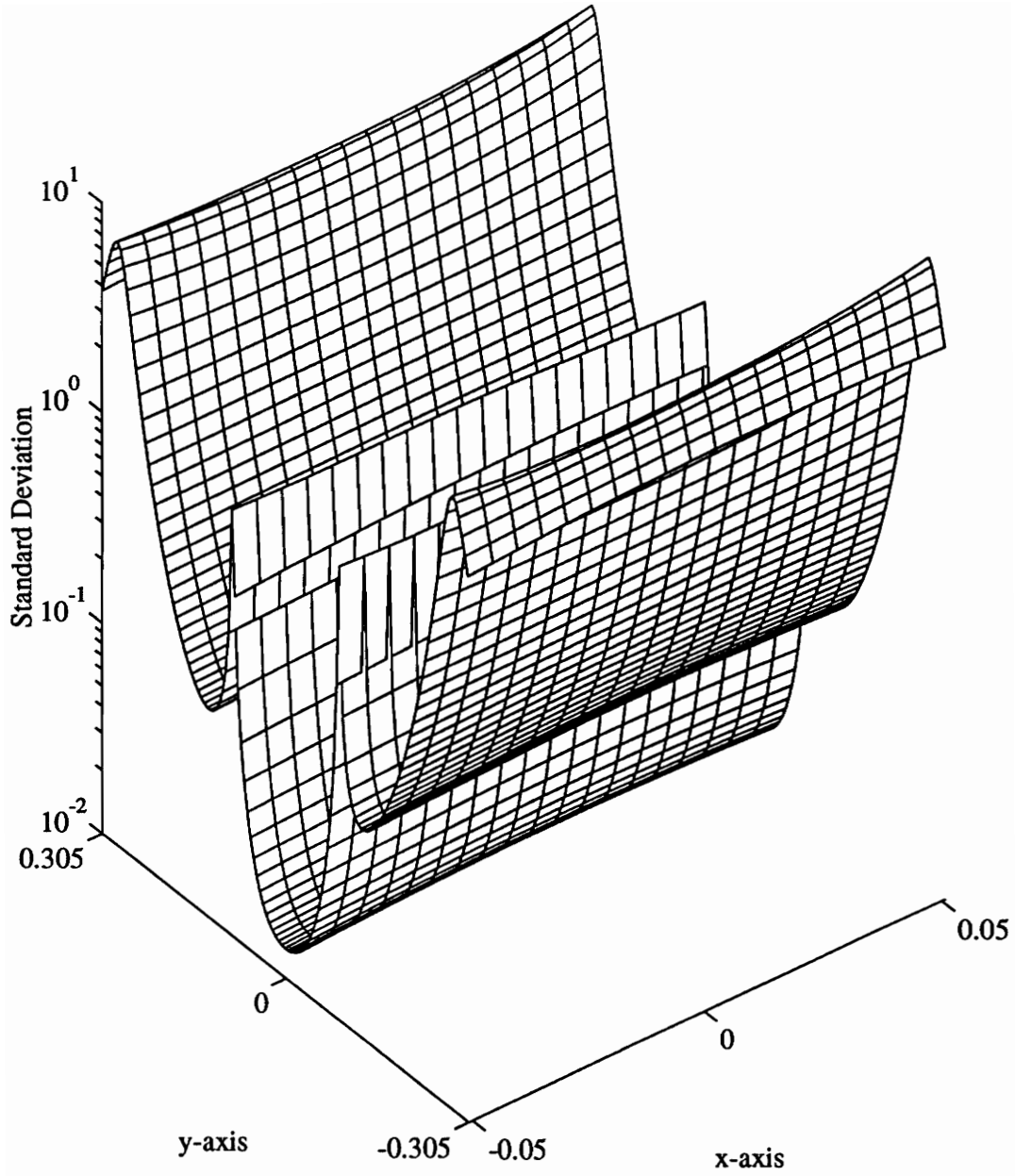

Figure 4.24 Standard Deviation of Poisson's Ratio 1418 Hz, 2*Reference Force

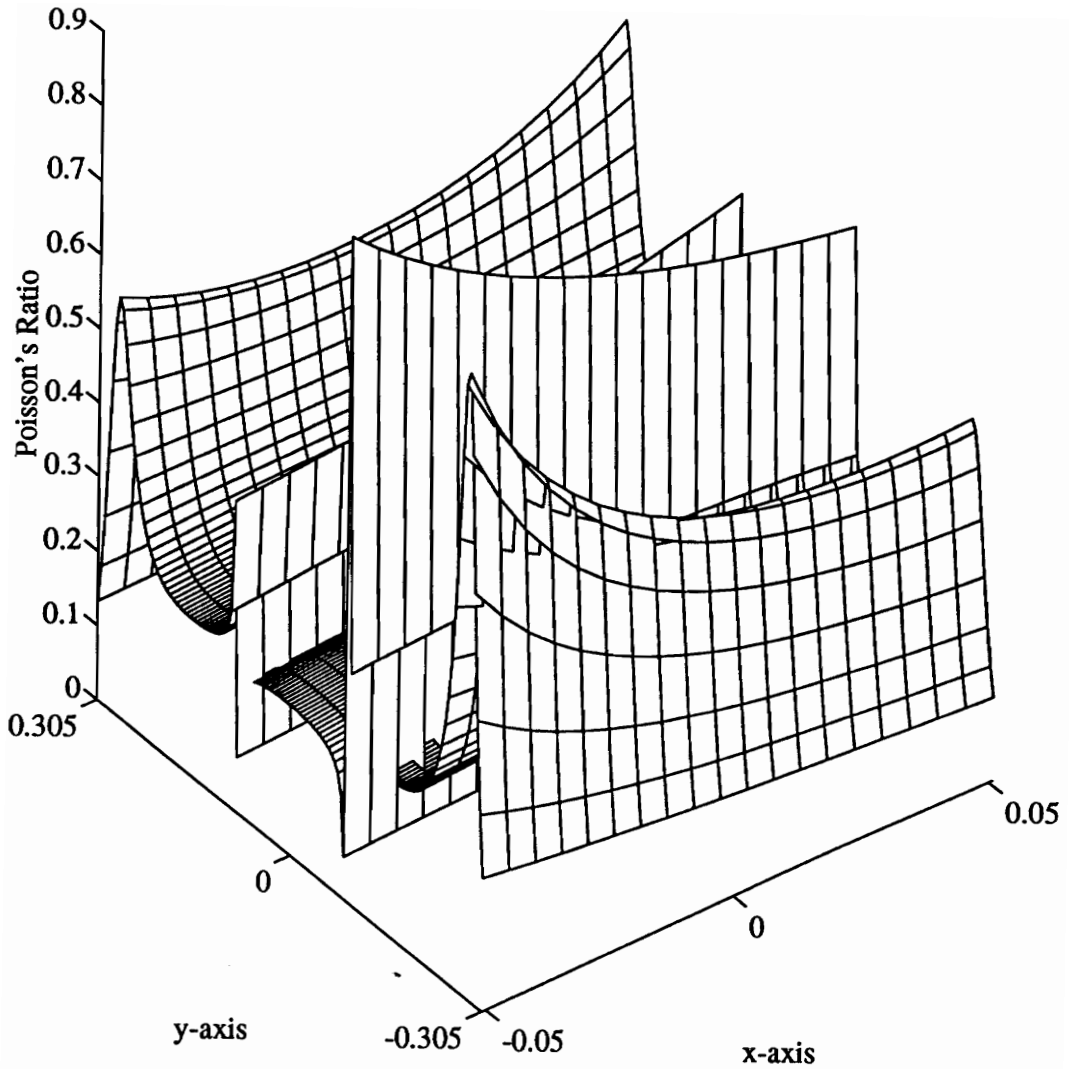

Figure 4.25 Poisson's Ratio 1418 Hz, 3* Reference Force

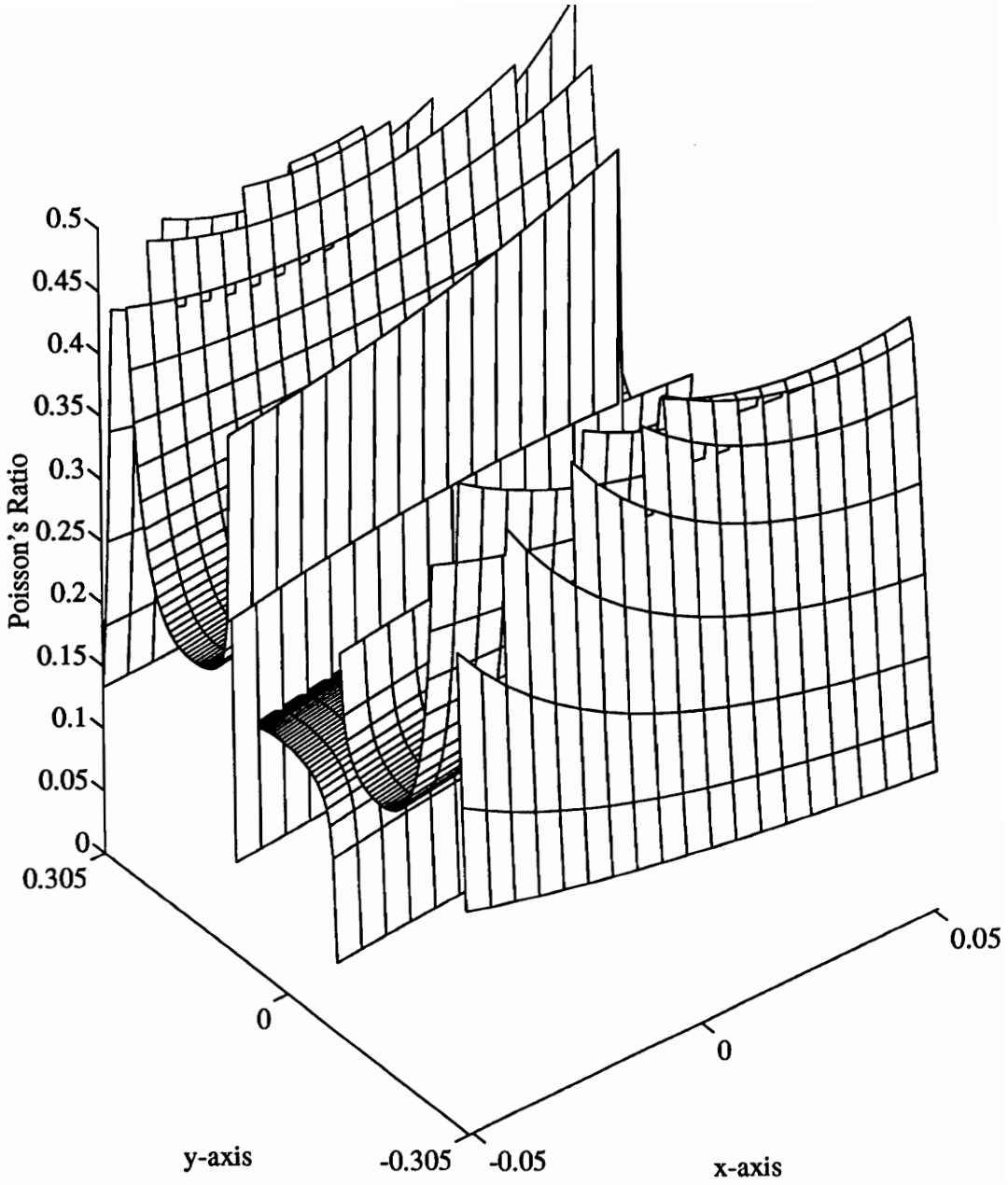

Figure 4.26 Poisson's Ratio 1418 Hz, 3* Reference Force, Peaks Removed

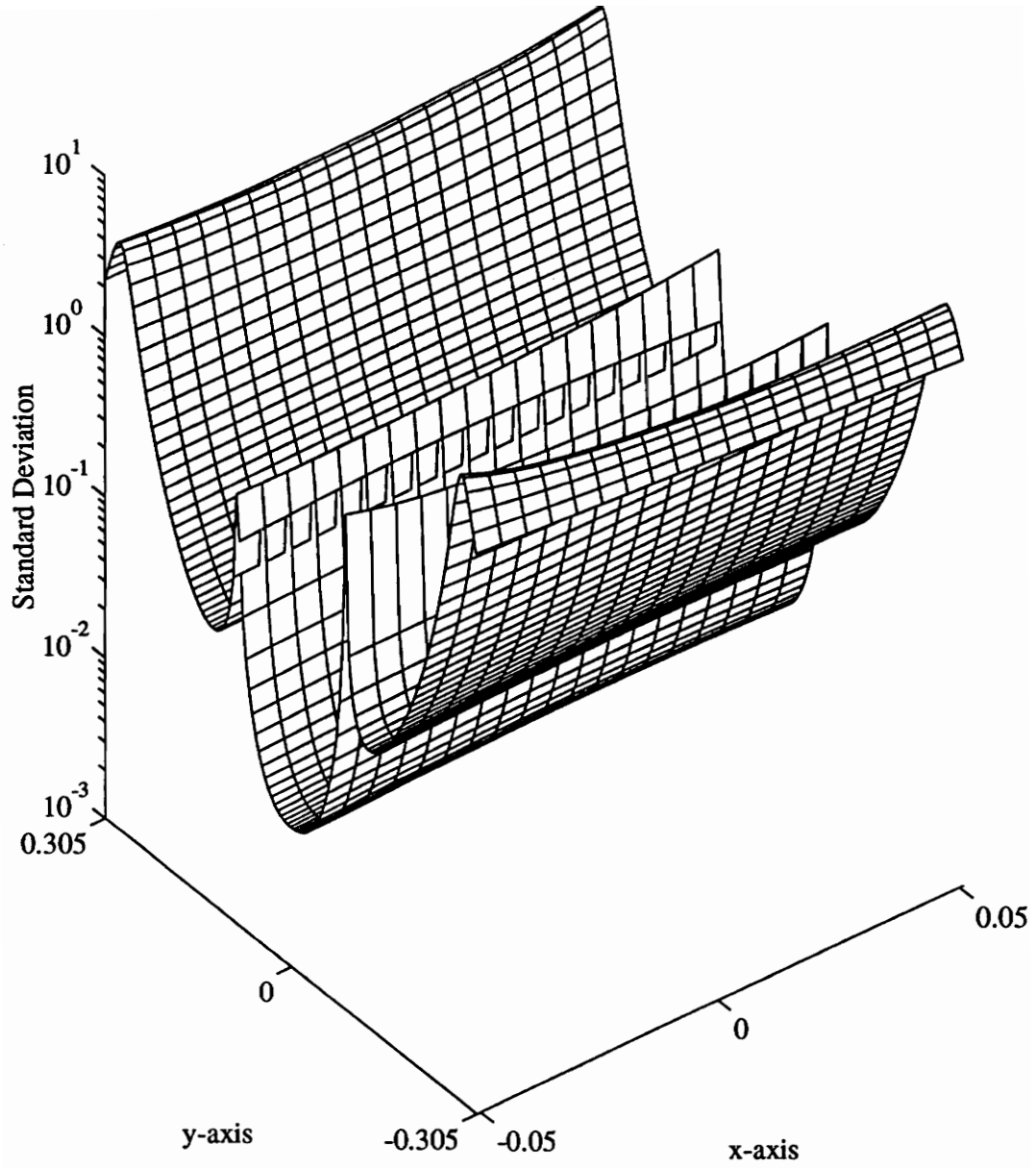

Figure 4.27 Standard Deviation of Poisson's Ratio 1418 Hz, 3*Reference Force

4.3 Discussion

Several observations can be made about the local estimates of Poisson's ratio. The estimates of Poisson's ratio vary with spatial location on the structure. In several cases the values become exceedingly large in magnitude. In general, these points correspond to the nodes or areas near the nodes of the operating shapes. Since the node is most likely a deflection point, it is expected that the second derivative of the deflection in the length-wise direction will be zero. Since this derivative appears in the denominator of the expression for Poisson's ratio, these large values for Poisson's ratio are not unexpected. Once these peaks are removed, slight spatial variations of Poisson's ratio are evident. This, coupled with the fact that the estimates exhibit low variances in regions of large curvature, indicates that the estimates of Poisson's does change with location.

Having discussed the local estimates of Poisson's ratio, we can now consider the global estimates. Figures 4.28 through 4.29 show the global estimates for the mean value and standard deviation for Poisson's ratio for the different loading cases.

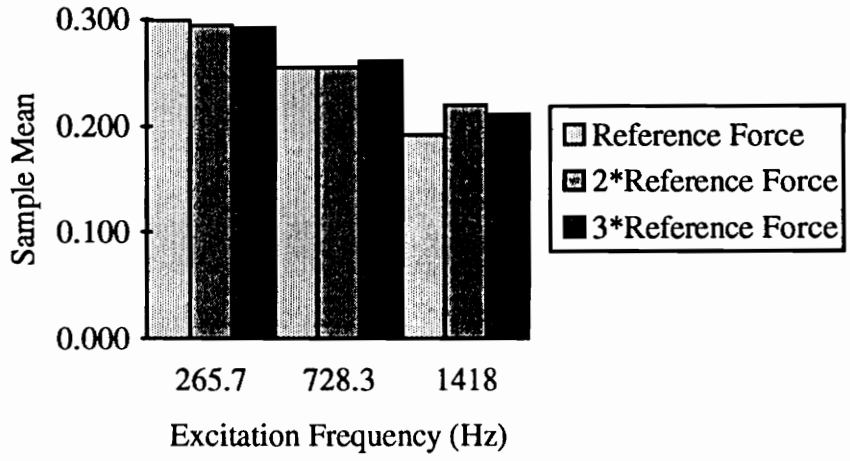

Figure 4.28 Sample Mean of Poisson's Ratio

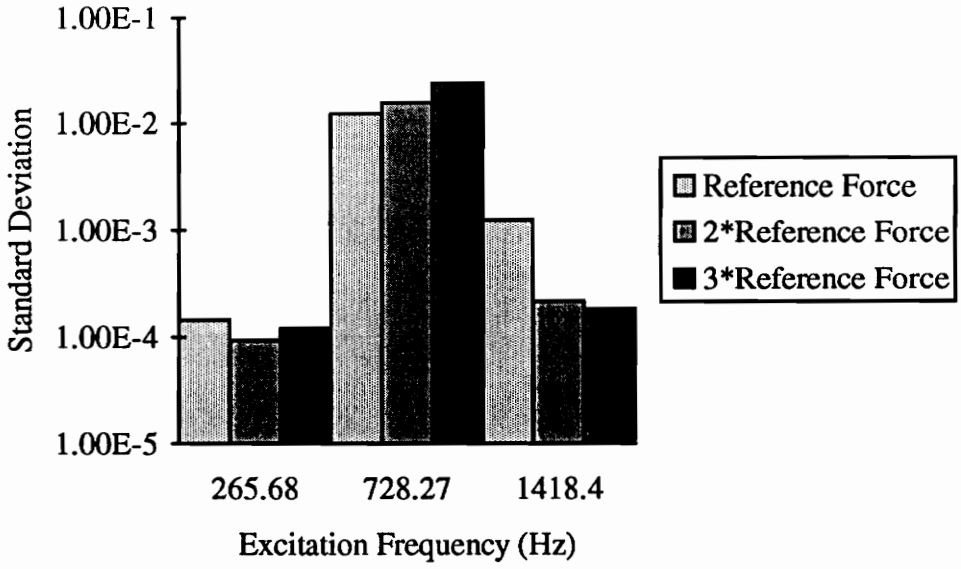

Figure 4.29 Sample Standard Deviation of Poisson's Ratio

The sample mean and sample standard deviation can be used to form the confidence bounds for the true value of Poisson's ratio. Once the confidence bounds have been formed, conclusions can be made as to whether or not the estimates of the true value and variance of Poisson's ratio arrived at for the different cases are indeed different. These conclusions are arrived at as follows.

The confidence bounds define the region over which the true value of a parameter is expected to lie, based on the sample data. There is equal probability that the true value of the parameter lies at any point in the confidence bound at the designated level of confidence. Therefore, if the confidence bounds for different cases overlap, it can be said that we cannot dismiss the hypothesis that the estimates are different. However, if the confidence bounds do not overlap, it can be said that the estimates are indeed different.

These assertions are made at a level of confidence equal to the confidence level of the confidence bounds which in this case is 95%. Graphs of the 95% confidence bounds for the true value of Poisson's ratio is shown in Figures 4.12, 4.13, 4.14, and 4.15 and the values are tabulated in Table 4.1

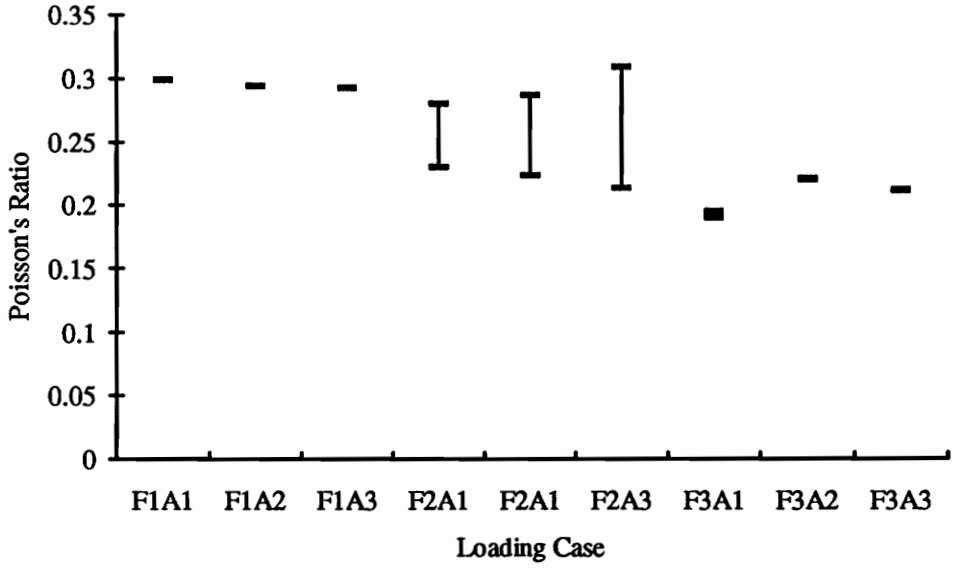

Figure 4.30 95 % Confidence Bounds for Poisson's Ratio

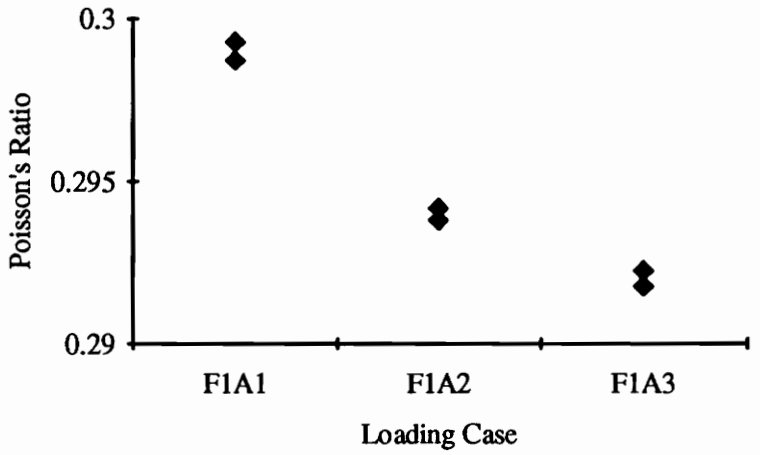

Figure 4.31 95% Confidence Bounds for Poisson's Ratio for 265.68 Hz Excitation

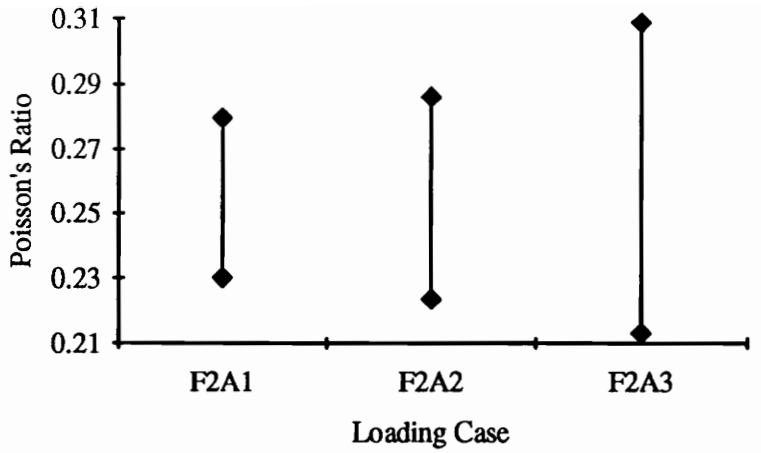

Figure 4.32 95% Confidence Bounds for Poisson's Ratio for 728.27 Hz Excitation

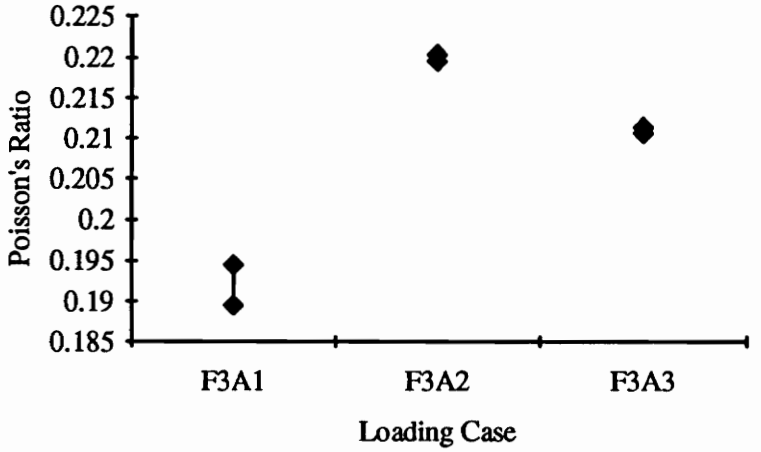

Figure 4.33 95% Confidence Bounds for Poisson's Ratio for 1418.4 Hz Excitation

Table 4.1 95% Confidence Bounds for Poisson's Ratio

	265.68 Hz	728.27 Hz	1418.4 Hz
Ref.	$0.2987<\mu_V<0.2993$	$0.2301<\mu_V<0.2799$	$0.1895<\mu_V<0.1945$
2*Ref.	$0.2938<\mu_V<0.2942$	$0.2237<\mu_V<0.2863$	$0.2196<\mu_V<0.2204$
3*Ref.	$0.2918<\mu_V<0.2922$	$0.2132<\mu_V<0.3088$	$0.2106<\mu_V<0.2114$

Confidence bounds can also be placed on the true value of the variance of Poisson's ratio. These are shown in Figs. 4.34 through 4.37.

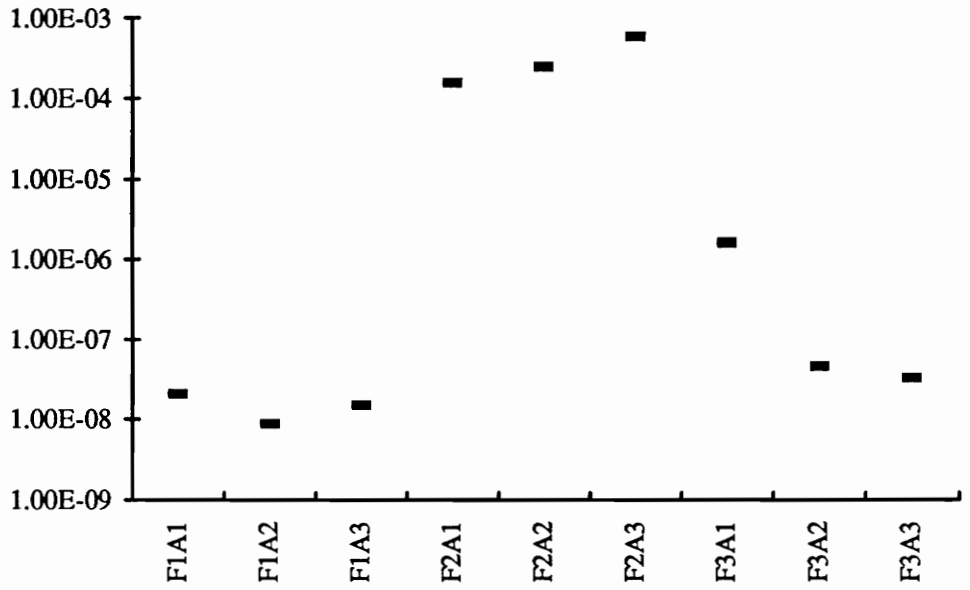

4.34 95% Confidence Bounds for Variance

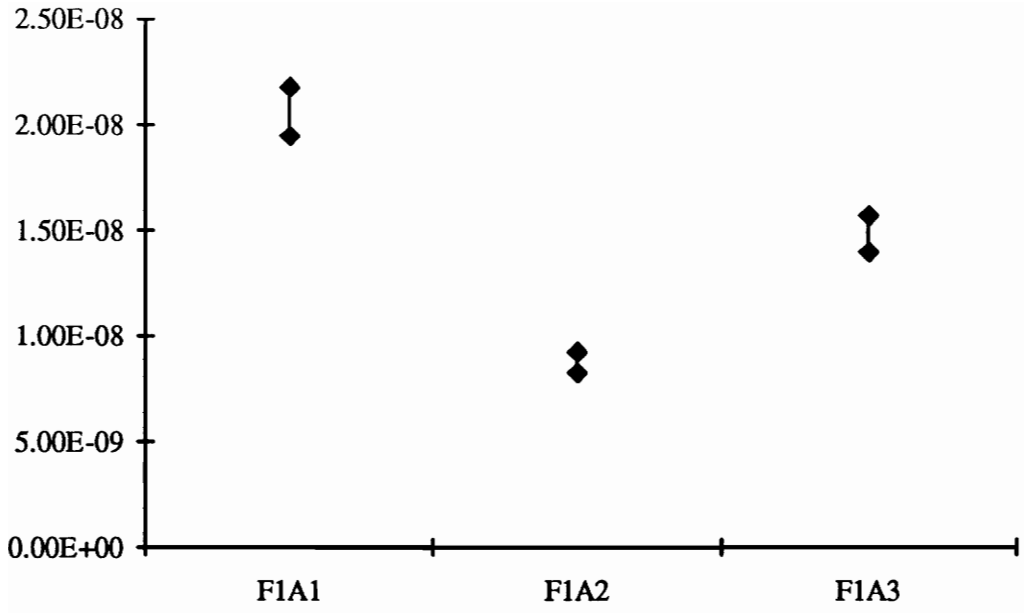

Figure 4.35 95% Confidence Bounds for Variance, 265.68 Hz Excitation

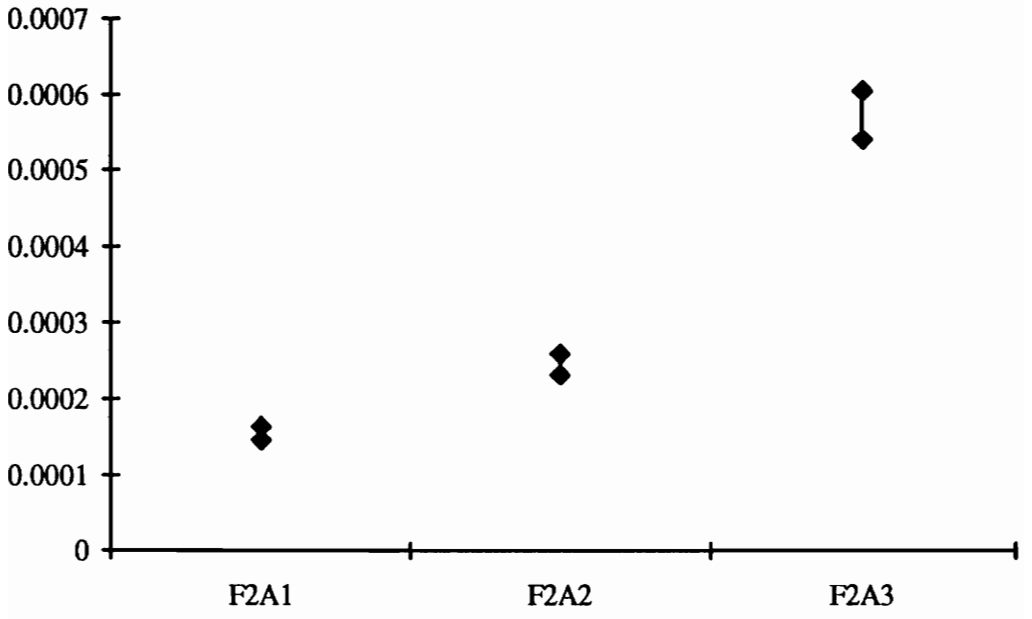

Figure 4.36 95% Confidence Bounds for Variance, 728.27 Hz Excitation

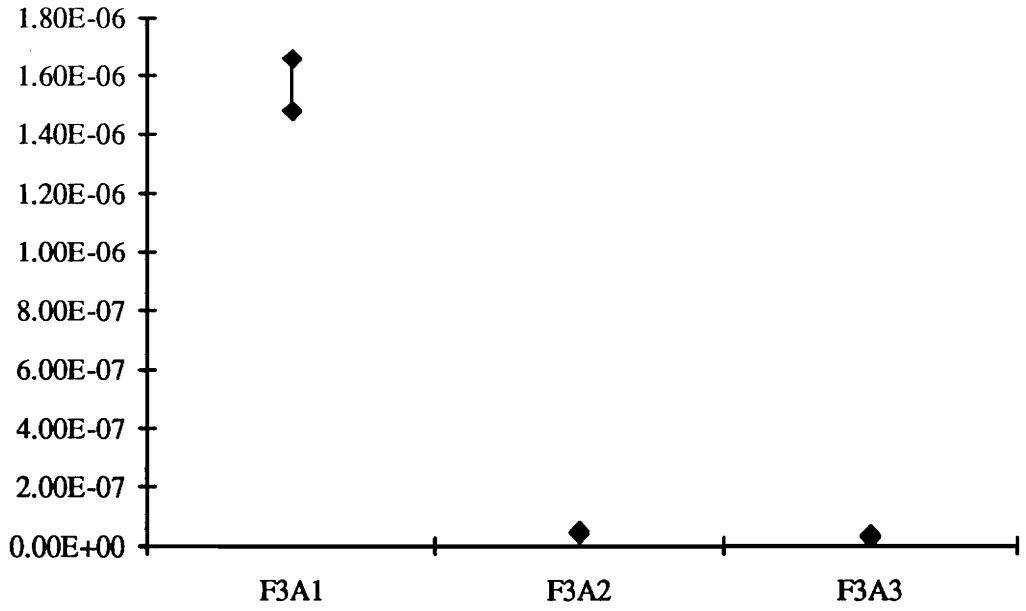

Figure 4.37 95% Confidence Bounds for Variance, 1418.4 Hz Excitation

Table 4.2 95% Confidence Bounds for Variance of Poisson's Ratio

	265.68 Hz	728.27 Hz	1418.4 Hz
A 1	1.95E-08<σ_ν^2<2.18E-08	1.46E-04<σ_ν^2<1.64E-04	1.48E-06<σ_ν^2<1.66E-06
A 2	8.24E-09<σ_ν^2<9.23E-09	2.31E-04<σ_ν^2<2.59E-04	4.32E-08<σ_ν^2<4.84E-08
A 3	1.39E-08<σ_ν^2<1.56E-08	5.40E-04<σ_ν^2<6.05E-04	3.09E-08<σ_ν^2<3.46E-08

Interpretation of theses results are centered on two questions. Are the estimates of Poisson's ratio different for different excitation frequencies and for a given excitation frequency, are the estimates of Poisson's ratio different for different excitation amplitudes?

Based on the confidence bounds of Figure 4.30, it can be said that frequency does affect the estimates of Poisson's ratio and all of the estimates lie below the excepted value of

Poisson's ratio for aluminum of .33. In general the estimates from the first operating shape are larger than results from the third operating shape. However, no conclusions can be made concerning the differences between the first and third operating shapes and the second and third operating shapes. Turning to the estimates of the variance, the variances for the first and third operating shapes are both several orders of magnitude lower than the variances for the second operating shape. This shows that the estimates based on the first and third operating shapes have less scatter that the estimates based on the third operating shape. It can be concluded that the value of Poisson's ratio is affected by the excitation frequency.

Next, the effects of excitation amplitude are considered. For the excitation frequency of 265.68 Hz, the true values of Poisson's ratio are different for different excitation amplitudes. Furthermore, the estimates tend to decrease as the amplitude increases. For the excitation frequency of 728.27 Hz, the estimates of Poisson's are independent of forcing amplitude since the confidence bounds overlap. For the excitation frequency of 1218.4 Hz, the third excitation frequency, the estimates are different for the three amplitudes, with the estimates of the first and third amplitudes being lower than the estimates for the second amplitude.

The dependence of variance on frequency and amplitude are considered nest. Figure 4.34 shows that the variances of the estimates are affected by the excitation amplitude. For the excitation frequency of 265.68 Hz the variance increases and then decreases with amplitude. For the excitation frequency of 728.27 Hz the variance increases with amplitude. For the excitation frequency of 1418.4 Hz the variance decreases with

amplitude. From these results it appears that the amplitude does affect the variance, however there is no clear trend.

4.3 Discussion

Having determined that the estimates of Poisson's ratio are different for different excitation conditions, it is now necessary to explain causes for this behavior. To aid in this, a table of the coefficients of the Legendré' surfaces selected by the forward regression are shown in Tables 4.3, 4.4 and 4.5 on the following pages.

Table 4.3 Coefficients of Legendré Surfaces for 265.68 Hz Excitation

Legendré Surface	F1A1no6	F1A2no6	F1A3no6
$P_{00}(\tilde{x},\tilde{y})$	4.96E-08	8.40E-08	1.47E-07
$P_{01}(\tilde{x},\tilde{y})$	-3.33E-08	9.52E-09	3.30E-08
$P_{02}(\tilde{x},\tilde{y})$	-1.18E-05	-2.26E-05	-3.25E-05
$P_{03}(\tilde{x},\tilde{y})$	-2.37E-08	-7.36E-08	-1.32E-07
$P_{04}(\tilde{x},\tilde{y})$	1.30E-06	2.49E-06	3.60E-06
$P_{05}(\tilde{x},\tilde{y})$	-1.75E-08	-7.67E-08	-1.72E-07
$P_{06}(\tilde{x},\tilde{y})$	-9.28E-08	-2.02E-07	-3.12E-07
$P_{10}(\tilde{x},\tilde{y})$	0.00E+00	5.05E-08	8.64E-08
$P_{11}(\tilde{x},\tilde{y})$	0.00E+00	3.87E-08	7.38E-08
$P_{12}(\tilde{x},\tilde{y})$	0.00E+00	1.12E-08	0.00E+00
$P_{13}(\tilde{x},\tilde{y})$	0.00E+00	0.00E+00	0.00E+00
$P_{14}(\tilde{x},\tilde{y})$	-2.95E-08	-1.39E-08	-3.39E-08
$P_{15}(\tilde{x},\tilde{y})$	0.00E+00	1.32E-08	2.04E-08
$P_{16}(\tilde{x},\tilde{y})$	3.12E-08	0.00E+00	0.00E+00
$P_{20}(\tilde{x},\tilde{y})$	7.08E-08	1.34E-07	1.94E-07
$P_{21}(\tilde{x},\tilde{y})$	0.00E+00	0.00E+00	0.00E+00
$P_{22}(\tilde{x},\tilde{y})$	-9.78E-08	-1.72E-07	-2.38E-07
$P_{23}(\tilde{x},\tilde{y})$	0.00E+00	0.00E+00	0.00E+00
$P_{24}(\tilde{x},\tilde{y})$	1.86E-08	5.90E-08	9.26E-08
$P_{25}(\tilde{x},\tilde{y})$	0.00E+00	0.00E+00	0.00E+00
$P_{26}(\tilde{x},\tilde{y})$	0.00E+00	0.00E+00	0.00E+00

Table 4.4 Coefficients of Legendré Surfaces for 728.27 Hz Excitation

Legendré Surface	F2A1no7	F2A2no7	F2A3no7
$P_{00}(\tilde{x},\tilde{y})$	1.71E-09	3.52E-09	3.77E-09
$P_{01}(\tilde{x},\tilde{y})$	-8.56E-09	-1.99E-08	-3.03E-08
$P_{02}(\tilde{x},\tilde{y})$	7.14E-09	1.29E-08	1.65E-08
$P_{03}(\tilde{x},\tilde{y})$	1.33E-06	2.63E-06	3.87E-06
$P_{04}(\tilde{x},\tilde{y})$	3.86E-09	9.08E-09	1.51E-08
$P_{05}(\tilde{x},\tilde{y})$	-3.45E-07	-6.80E-07	-9.98E-07
$P_{06}(\tilde{x},\tilde{y})$	1.69E-09	0.00E+00	5.05E-09
$P_{07}(\tilde{x},\tilde{y})$	4.78E-08	9.40E-08	1.41E-07
$P_{10}(\tilde{x},\tilde{y})$	-1.99E-09	-4.80E-09	-6.06E-09
$P_{11}(\tilde{x},\tilde{y})$	4.26E-09	1.12E-08	1.38E-08
$P_{12}(\tilde{x},\tilde{y})$	-3.01E-09	-8.09E-09	-9.73E-09
$P_{13}(\tilde{x},\tilde{y})$	-4.10E-09	-5.94E-09	-1.12E-08
$P_{14}(\tilde{x},\tilde{y})$	0.00E+00	0.00E+00	0.00E+00
$P_{15}(\tilde{x},\tilde{y})$	4.64E-09	0.00E+00	0.00E+00
$P_{16}(\tilde{x},\tilde{y})$	0.00E+00	0.00E+00	0.00E+00
$P_{17}(\tilde{x},\tilde{y})$	0.00E+00	0.00E+00	-7.70E-09
$P_{20}(\tilde{x},\tilde{y})$	0.00E+00	2.52E-09	0.00E+00
$P_{21}(\tilde{x},\tilde{y})$	-2.80E-08	-5.74E-08	-8.21E-08
$P_{22}(\tilde{x},\tilde{y})$	0.00E+00	8.77E-09	8.06E-09
$P_{23}(\tilde{x},\tilde{y})$	2.98E-08	5.66E-08	8.68E-08
$P_{24}(\tilde{x},\tilde{y})$	0.00E+00	6.89E-09	0.00E+00
$P_{25}(\tilde{x},\tilde{y})$	-1.58E-08	-3.06E-08	-3.86E-08
$P_{26}(\tilde{x},\tilde{y})$	0.00E+00	0.00E+00	0.00E+00
$P_{27}(\tilde{x},\tilde{y})$	0.00E+00	0.00E+00	1.29E-08

Table 4.5 Coefficients of Legendré Surfaces for 1418.4 Hz Excitation

Legendré Surface	F3A1no8	F3A2no8	F3A3no8
$P_{00}(\tilde{x},\tilde{y})$	0.00E+00	-3.43E-10	-7.47E-10
$P_{01}(\tilde{x},\tilde{y})$	6.35E-10	1.09E-09	1.76E-09
$P_{02}(\tilde{x},\tilde{y})$	7.49E-09	1.36E-08	1.99E-08
$P_{03}(\tilde{x},\tilde{y})$	1.76E-09	3.34E-09	5.08E-09
$P_{04}(\tilde{x},\tilde{y})$	1.38E-07	2.70E-07	4.03E-07
$P_{05}(\tilde{x},\tilde{y})$	0.00E+00	0.00E+00	-1.25E-09
$P_{06}(\tilde{x},\tilde{y})$	-5.95E-08	-1.15E-07	-1.72E-07
$P_{07}(\tilde{x},\tilde{y})$	0.00E+00	0.00E+00	0.00E+00
$P_{08}(\tilde{x},\tilde{y})$	1.20E-08	2.36E-08	3.51E-08
$P_{10}(\tilde{x},\tilde{y})$	0.00E+00	5.89E-10	6.37E-10
$P_{11}(\tilde{x},\tilde{y})$	0.00E+00	-1.27E-09	-1.28E-09
$P_{12}(\tilde{x},\tilde{y})$	0.00E+00	1.25E-09	8.81E-10
$P_{13}(\tilde{x},\tilde{y})$	0.00E+00	0.00E+00	0.00E+00
$P_{14}(\tilde{x},\tilde{y})$	0.00E+00	-2.01E-09	-3.03E-09
$P_{15}(\tilde{x},\tilde{y})$	0.00E+00	0.00E+00	0.00E+00
$P_{16}(\tilde{x},\tilde{y})$	0.00E+00	0.00E+00	2.48E-09
$P_{17}(\tilde{x},\tilde{y})$	0.00E+00	0.00E+00	-1.64E-09
$P_{18}(\tilde{x},\tilde{y})$	0.00E+00	0.00E+00	0.00E+00
$P_{20}(\tilde{x},\tilde{y})$	-1.44E-09	-3.03E-09	-4.67E-09
$P_{21}(\tilde{x},\tilde{y})$	0.00E+00	0.00E+00	0.00E+00
$P_{22}(\tilde{x},\tilde{y})$	-5.12E-09	-7.29E-09	-1.09E-08
$P_{23}(\tilde{x},\tilde{y})$	0.00E+00	0.00E+00	0.00E+00
$P_{24}(\tilde{x},\tilde{y})$	6.77E-09	1.21E-08	1.85E-08
$P_{25}(\tilde{x},\tilde{y})$	0.00E+00	0.00E+00	0.00E+00
$P_{26}(\tilde{x},\tilde{y})$	0.00E+00	-7.92E-09	-1.07E-08
$P_{27}(\tilde{x},\tilde{y})$	0.00E+00	0.00E+00	0.00E+00
$P_{28}(\tilde{x},\tilde{y})$	0.00E+00	2.08E-09	2.32E-09

The effect of excitation frequency will be discussed first followed by a discussion of the effect of the excitation amplitude.

Recalling that the operating shapes consist of contribution from all the modes of the structure, as the excitation frequency increases, the contribution of the modes below the excitation frequency decreases and the contribution of the modes above the excitation frequency increases as shown in Figure 4.38.

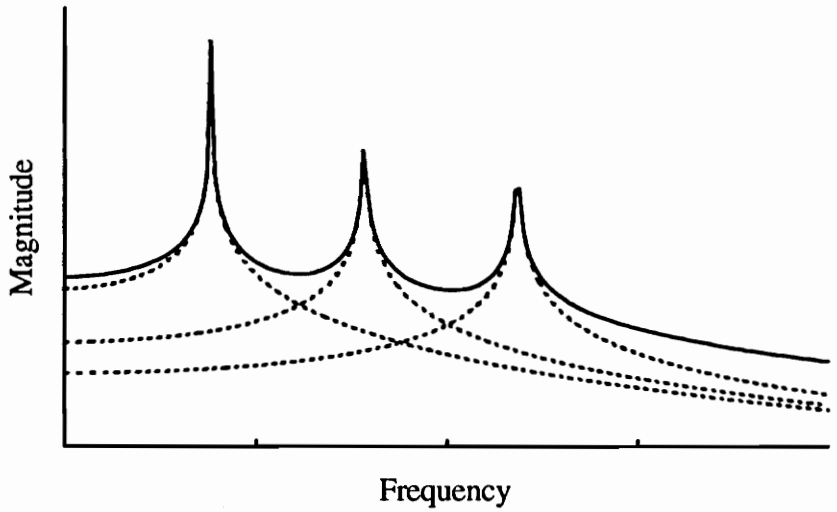

Figure 4.38 Modal Contributions of Multi-Degree of Freedom System

Therefore, the second and third operating shapes have more content contributed by the higher modes, such as the plate modes, than the first operating shape. The response due to plate modes, constructively or destructively interferes with the anticlastic bending. Since it was assumed that all curvature in the *xz* plane was due to Poisson's effect and some of this curvature may be due to the contribution of higher modes, it is reasonable to

expect the contribution of the higher modes to affect the estimates of Poisson's ratio and for this effect to increase as the frequency increases.

Consider the shapes of the first three bending modes and the first plate mode. The first plate mode will contribute curvature in the same direction along the length of the beam as shown in Figure 4.39. The anticlastic curvature of the first bending mode is also in the same direction along the length of the beam, but may not be in phase with the first plate mode. Therefore for the first operating shape, the plate mode will either increase or decrease the curvature along the length of the beam. For the second beam mode, the anticlastic curvature is of one direction over one half the length of the beam, and of the opposite direction along the other half of the beam. Therefore the plate mode will increase the curvature along one half of the beam and decrease the curvature over the other half of the beam, regardless of the phase relationship. This would explain the increased variance for the estimates based on the second operating shapes. A similar effect would occur for the third mode except to a lesser extent since the areas of opposite signed anticlastic curvature are unequal whereas for the second mode the areas of opposite signed anticlastic curvature are equal.

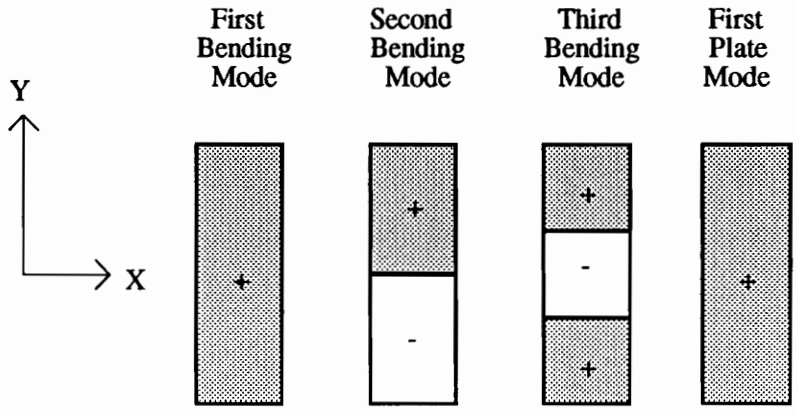

Figure 4.39 Relative Width-Wise Curvature of Modes

This effect can be verified by looking at the deflection at various cross sections of the beam model. If the structure has free-free end conditions and was responding purely in the first bending mode, the anticlastic curvature at the edge would be zero. Any non-zero curvature at the end must be attributed to contribution of plate modes, assuming that the end conditions are free-free.

Figures 4.40, 4.41, and 4.42 show the deflection of uniformly spaced cross sections with the bending mode response removed.

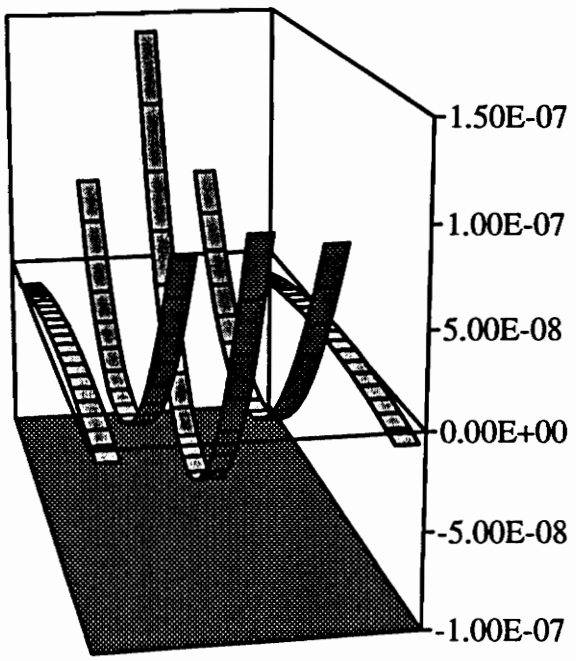

Figure 4.40 Cross Sections of Beam, 265.68 Hz Excitation

It is clear that the first operating shape has considerable contribution from the plate mode. This contribution will bias the estimate of Poisson's ratio since it decreases the curvature

throughout the length of the beam since the curvature at the end is in the opposite direction of the curvature in the center.

Similar results exist for the second operating shape. It is expected that at the middle of the beam, the deflection should be zero since this is a node. However contribution of the first plate mode is perceptible near the node of the second bending mode.

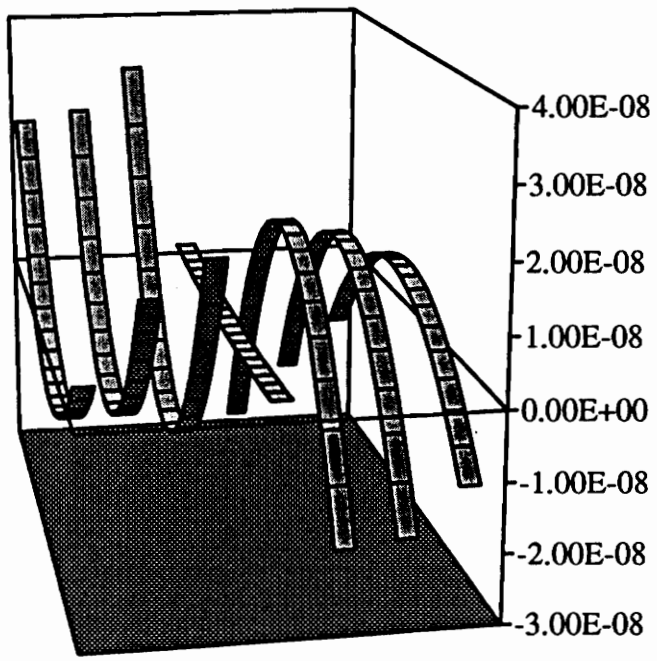

Figure 4.41 Cross Sections of Beam, 728.27 Hz Excitation

Tthe third operating shape also exhibits width-wise curvature at the beam ends.

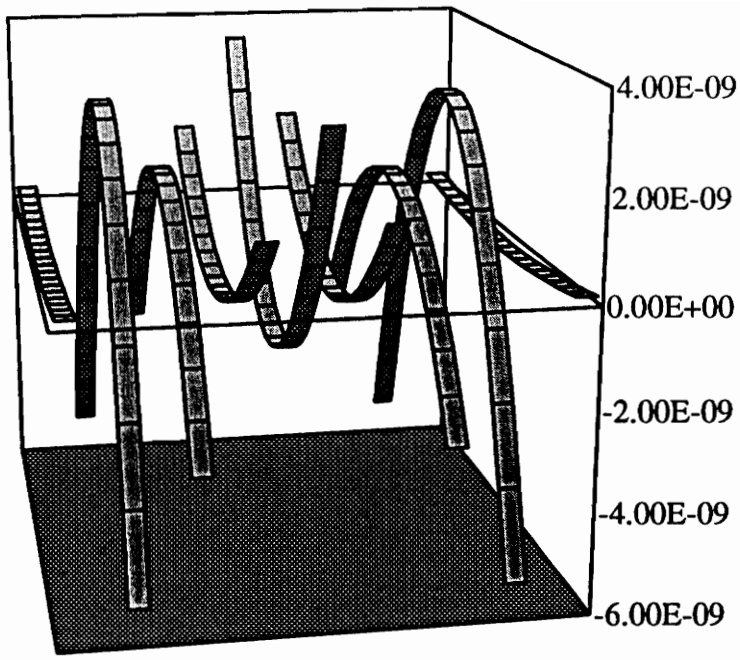

Figure 4.42 Cross Sections of Beam, 1418.4 Hz Excitation

It is readily evident from these plots that there is significant widthwise curvature due to the first plate mode.

Although it appears that there is no way to discern the contribution of the higher frequency modes and the dominant mode from the operating shape, a mechanism does exist, provided that care is taken during the data collection.

Consider the phase response of velocity referenced to force for a multi-degree of freedom system.. If the system is excited at a frequency below the first resonant frequency, the modal contributions will all be in phase. However, if the system is excited at the first mode resonance, all of the higher modes will be either +90° or -90° out of phase with the first mode. Therefore, by measuring the velocity using the laser velocimeter, the real

component of the velocity corresponds to the velocity of the first mode and the imaginary component corresponds to the total contribution of the remaining modes. The fact that the data was processed based on the magnitude precludes the use of this analysis. However, examination of the raw data does not exhibit the behavior of the real part consisting only of the first bending mode and the imaginary part consist of all the content except the bending mode. This could be due to the fact that the frequency of excitation was close to resonance, but the high sensitivity of the modal phase relationships at resonance, amplifies the effects slight shifts from the resonant frequency.

The effect of amplitude can also be described in terms of the contribution of higher modes and by inspection of the coefficients of the Legendré surfaces listed in Tables 4.3, 4.4 and 4.5. At low levels of excitation, the contribution of the higher modes may be buried in the noise floor or are below the resolution of the velocimeter. As the amplitude increases, the contribution of the higher modes emerges from the noise floor. This is supported by the addition of surfaces in the model at higher amplitudes that were not present at lower. Counteracting this effect is the contribution of the random content which was assumed to be additive. Since a gain was applied to the velocity signal in order to utilize the full dynamic range of the A/D converter, the additive error increased as the gain increased. Since the gain would be highest for the lower amplitudes it is expected that the variance would be highest for the lower amplitudes, and if the error is indeed additive, the variance would decrease with increasing excitation amplitude. This trend only held for the third operating shape.

4.4 Summary

The results show that the local and global estimates of Poisson's ratio are affected by the forcing conditions. The local estimates vary with spatial location and exhibit the lowest variance at areas of high curvature. The global estimates are all lower than the accepted value of .33 for Poisson's ratio for aluminum and appear to decrease with increasing frequency. The estimates based on the first and third operating shape exhibit lower variance than the estimates based on the second operating shape. It is shown that the contribution of the plate mode effects the estimate of Poisson's ratio.

Chapter 5

Conclusions and Recommendations

5.1 Introduction

It has been shown that estimates of Poisson's ratio can be found from measured velocity profiles of a free-free aluminum beam under dynamic loading conditions based on measurement of the anticlastic curvature. The proposed procedure was successful in arriving at both local and global estimates.

5.2 Conclusions

Estimates of Poisson's ratio for the free-free aluminum beam considered in this study were found to be dependent on the spatial location. The estimates and variances are also dependent upon the frequency and amplitude of excitation. The global estimates are below the accepted value of .33 for aluminum and are statistically significant. It is not conclusive as to whether the differences are caused by actual changes in Poisson's ratio or sensitivity of the estimation procedure to the operating conditions.

5.3 Recommendations

Following careful analysis of the results, several areas, both in the experiment and the processing, warrant investigation in order to determine if the procedure for estimating Poisson's ratio from velocity profiles can be improved. Exciting the structure at resonance and processing both the imaginary and real components of velocity instead of converting

the real and imaginary components into a magnitude may help in identifying the non-bending mode content. Selecting possible regressors more compatible with the physical system, for instance, using polynomial surfaces with zero second derivatives in the lengthwise direction along the top and bottom edges to account for the boundary conditions of a free-free beam should also be considered. An alternative to this is to apply a constrained weighted least squares process in order to force the model to fit the end conditions of the structure. In order to obtain a more descriptive relationship between Poisson's ratio and the amplitude and frequency of excitation, we recommend that the experiment be conducted at more frequencies. A more complete study would develop a three-dimensional analytical model of the dynamic deflection of the beam, accounting for Poisson's effect, for predicting the behavior of Poisson's ratio for different amplitudes and frequencies of excitation. A more rigorous model of Poisson's effect, accounting for the three-dimensional crystalline structure may also prove beneficial.

References

Beckwith, Thomas G., Marangoni, Roy D., and Lienhard, John H., V, 1993. Mechanical Measurements, Addison-Wesley Publishing Company, New York, New York.

Beer, Ferdinand P., and Johnston, E. Russel, Jr., 1981. Mechanics of Materials, McGraw-Hill Book Company, New York, New York.

Carvill, James, 1981. Famous Names in Engineering, Butterworth and Company, Boston, Massachusetts.

Dally, James W. and Riley, William F., 1978. Experimental Stress Analysis, Second Ed., McGraw-Hill Book Company, New York, New York.

Drain, L. E., 1980. The Laser Doppler Technique, John Wiley & Sons, New York, New York.

Jarosz, B. J. "Ultrasonic Surface Modes Generated by Laser Pulses on Duraluminum" Ultrasonics v. 29, no. 1, Jan 1991, p. 53-57.

Mihara, T., and Obata, M. "Elastic Constant Measurement by Using Line-focus-beam Acoustic Microscope" Experimental Mechanics, v. 32, no. 1, March 1992, pp. 30-33.

Montgomery, Douglas C., and Peck, Elizabeth A., 1992. Introduction to Linear Regression Analysis, Second Ed., John Wiley & Sons, Inc., New York, New York.

Neter, John, Wasserman, William, and Kutner, Michael H., 1990. Applied Linear Statistical Models, Third Ed., Irwin, Homewood, Illinois.

Ometron Limited, 1987. VPI Sensor Operator's Manual, London, England.

Richard, John, and Lomenzo, Richard. "Obtaining Poisson's Ratio From the Dynamic Measurement of Anticlastic Bending in a Beam", pp. 286-292.

Shames, H. Irving, 1975. Introduction to Solid Mechanics, Prentice Hall, Inc., Englewood Cliffs, New Jersey.

Swokowski, Earl W., 1988. Calculus with Analytical Geometry, Fifth Alternate Ed., PWS Kent Publishing Company, New York, New York.

Timoshenko, S., and Goddier, J. N., 1951. Theory of Elasticity, McGraw-Hill Book Company, New York, NewYork.

Ugural, A. C., 1991. Mechanics of Materials, McGraw-Hill, Inc., New York, New York.

Walpole, Ronald E., and Myers, Raymond H., 1993. Probability and Statistics for Engineers and Scientists, Fifth Ed., MacMillan Publishing Company, New York, New York.

Vita

Richard Lomenzo was born on May 10, 1969 in New Orleans, Louisiana. After graduating from Clover Hill High School in Midlothian, Virginia, he studied aerospace engineering at Virginia Tech in Blacksburg, Virginia, and graduated with a Bachelor of Science Degree in 1991. He continued his education in 1991 in the Mechanical Engineering Department at Virginia Tech and received his Master of Science degree in May, 1994. Following graduation, he will begin work on his Doctor of Philosophy degree and hopes to teach at the college level.